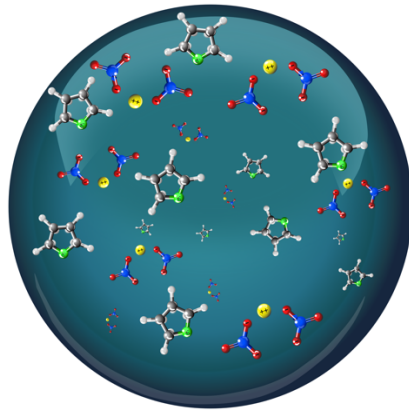# Deciphering gas phase synthesis of sulfide nanoparticles

Dem Fachbereich Produktionstechnik der
UNIVERSITÄT BREMEN

zur Erlangung des Grades
Doktor der Ingenieurwissenschaften (Dr.-Ing.)
genehmigte

Dissertation

von
Adithya Kaese, M.Sc.

Gutachter: Prof. Dr.-Ing. habil. Lutz Mädler
Prof. Dr. rer. nat. habil. Andreas Lüttge

Tag der mündlichen Prüfung: 29.04.2024

Abstract

With the ever-increasing need of impressively engineered materials, research has taken a shine to nanosized materials. This has been predominantly because matter on a nanoscale exhibit behaviours unusual to their bulk counterparts. Taking advantage of these properties on the nanoscale has been applied in many areas of research.

This thesis is focused on a particular group of nanomaterials – metal sulfides and their production through combustion synthesis. Metal sulfide nanoparticles are attractive materials for a wide range of application. The synthesis of metal sulfide nanoparticle has predominantly been through liquid phase synthesis. Although it can be highly versatile, challenges of scaling up production and the requirement for post processing exist. Combustion of liquid precursors using a flame set-up is an established and highly scalable route of synthesis for metal oxide nanoparticles. As combustion requires oxygen, synthesis of metal sulfides through this route is a challenge. This thesis delves into sources of metal and sulfur sources that are ideal to produce metal sulfide nanoparticles through combustion, tailored precursor-solvent solutions and mechanisms of breakdown and formation. Here, tetrahydrothiophene (THT) is used as an effective source of sulfur to produce metal sulfide nanoparticles such as those of copper and iron.

In addition, specific components formed on high temperature breakdown of sulfur source are investigated. Precursor-solvent solutions are poked and prodded using evaporation and distillation, the results of which were unexpected nor have been reported in prior studies.

Zusammenfassung

Angesichts des wachsenden Bedarfs an zunehmend wirkungsvollen technischen Werkstoffen, rückt die Forschung an Nanomaterialien stärker in den Vordergrund. Dies ist vor allem darauf zurückzuführen, dass Materie im Nanomaßstab ein Verhalten zeigt, welches sich von dem ihrer massigen Gegenstücke unterscheidet. Diese positiven Eigenschaften auf der Nanoskala finden heute bereits in einer Vielzahl von Forschungsbereichen ihre Anwendung.

Diese Thesis konzentriert sich auf eine bestimmte Gruppe von Nanomaterialien –Metallsulfide und ihre Herstellung durch Verbrennungssynthese. Metallsulfid-Nanopartikel sind für ein breites Spektrum von praktischen Anwendungen bevorzugte Materialien. Die Synthese von Metallsulfid-Nanopartikeln erfolgte überwiegend durch Flüssigphasensynthese. Obwohl diese Methode sehr vielseitig ist, gibt es Herausforderungen bei der Skalierung der Produktion sowie bei der erforderlichen Nachbearbeitung. Die Verbrennung von flüssigen Vorläufern durch die Nutzung eines Flammen-Systems ist ein etablierter und hochgradig skalierbarer Syntheseweg für Metalloxid-Nanopartikel. Allerdings erschwert der Bedarf von Sauerstoff diese Art der Verbrennung als Methode. Diese Thesis befasst sich mit Metall- und Schwefelquellen, die sich ideal für die Herstellung von Metallsulfid-Nanopartikeln durch Verbrennung, maßgeschneiderte Vorläufer-Lösungsmittel und Mechanismen des Abbaus und der Bildung eignen. Hier wird Tetrahydrothiophen (THT) als effektive Schwefelquelle zur Herstellung von Metallsulfid-Nanopartikeln wie Kupfer und Eisen verwendet.

Darüber hinaus werden spezifische Komponenten für den Hochtemperaturabbau von Schwefelquellen untersucht. Vorläufer-Lösungsmittel werden durch Verdampfung sowie Destillation angeregt und ergaben unerwartete Resultate, über welche in früheren Forschungsstudien nicht berichtet wurde.

Acknowledgement

grew close to and that have been there for me one way or the other – Sangita, Haipeng, Apo, Nithin and Dina, I would like to thank too.

Most importantly, I owe many thanks to my amazing family. Jörn, who lifted me up on every one of my dullest days and had me effortlessly lol. My parents and sister, who believed in me and supported me in every which way since day one. Getting here would have been impossible without them.

Table of Contents

Chapter 1. Introduction

1.1 Metal sulfide nanoparticles

Nanoparticles have historically been defined as particles of any shape with an equivalent diameter between 1 – 100 nm. They are found in nature and have also been used, although unintentionally, as far back as the 4th century in the Lycurgus cup where gold and silver nanoparticles were used to achieve colour variations. In the present decade, the applications and uses of nanoparticles are enormous. Here, in particular interest is one class of nanomaterials- metal sulfide nanoparticles. In the search for materials to improve areas such as battery technology, catalysis and anticorrosion there is extensive research building up around metal sulfide nanoparticles. The simple combination of metal ion and sulfur ion derives its uniqueness from smaller band gaps compared to oxide analogues and certain properties of sulfur.[1] Sulfur exists in oxidation states from -2 through +6 enabling more combination possibilities with metals than oxygen.[2] In theory, sulfur also has an ultra-high capacity and

energy density translating into an exciting cathode material, for example in lithium-sulfur batteries.

1.1.1 Applications and uses of metal sulfide nanoparticles

Metal sulfide nanoparticles find applications in a wide number of areas. Here we look at a few in-depth that have wide ranging implications on future technologies. One of the areas it is being investigated for is in lithium-ion batteries. Currently, graphite is the main anode material for lithium-ion batteries. Although it is used for its high coulombic efficiency and respectable cycling performance its notable drawback is its low theoretical capacity (372 mAh g^{-1}) which is a limiting factor to the energy density of the batteries. The comparatively high theoretical capacities coupled with low volumetric expansion on lithiation of metal sulfides have made it a strong candidate for potential anode material in lithium-ion batteries. Some of the widely studied are sulfides of transition metals such as molybdenum, zirconium, vanadium, tin and tungsten. These have a layered structure comparable to that of graphite which can accommodate lithium ions into their structure exhibiting theoretical capacities in the range of 432-1196 mAh g^{-1}.[3] The structures of some transition metal sulfides are displayed in Figure 1.

a. MoS_2 or WS_2 b. ZrS_2 or VS_2

c. VS_4 d. SnS_2
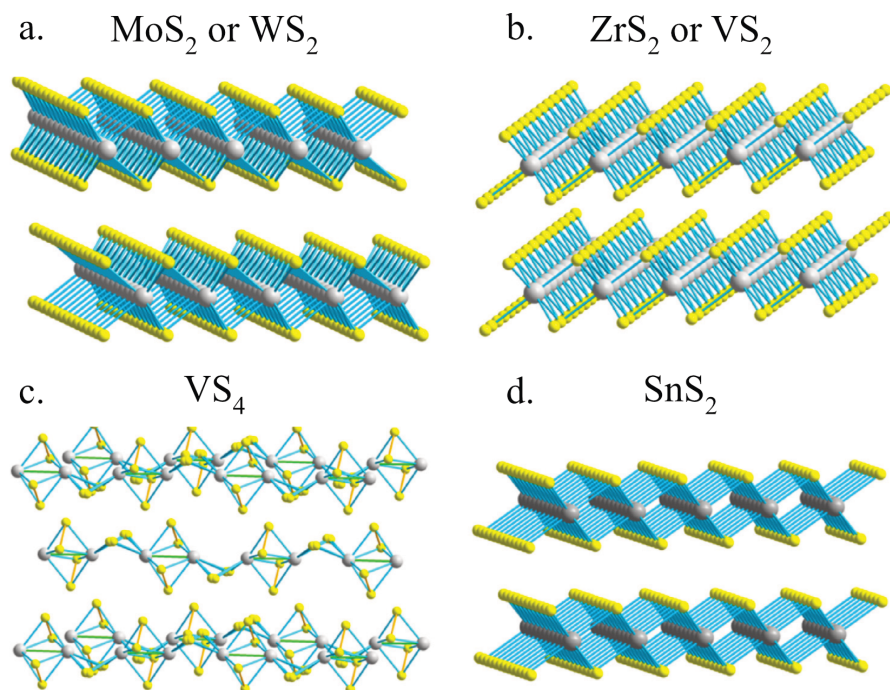
Figure 1. Transition metal sulfides show a layered structure of S-M-S comparable to that of graphite. Here, the yellow balls represent metal atoms and the grey balls represent sulfur atoms. Reproduced with permission.[3]

Studies on electrode material composed of composites of metal sulfide with metal oxide have also been done. Shi and Lu synthesized $SnO_2@SnS_2$ nanospheres and tested it as a high-performance anode material for Li ion batteries. The hierarchical hollow nanostructures exhibited an initial capacity of 1558 mA h g^{-1} and a reversible capacity of 548 mA h g^{-1} after 100 cycles.[4] Similarly, Wu et al have exhibited a layered SnS_2-SiO_2 nanorod structure with a capacity retention of 99.2% after 25 cycles.[5] SnS_2 as a material for electrode material is being investigated as it possesses higher reversible capacities than graphite. However, nanostructures and/or composites/heterostructures of SnS_2 are used to circumvent the issues of large volumetric expansions occurring on lithiation. Wang et al utilize the doping with large ions such as cerium to enlarge the crystal lattice. This provides more lattice space for the intercalation and de-intercalation of the lithium ions.[6]

With massive interest in recent years for hydrogen as an energy source, catalysts for water splitting to produce hydrogen are extensively being investigated. The standard catalysts that have been used for this are precious metal catalysts such as platinum. To be able to essentially split water into hydrogen, both hydrogen evolution reaction and oxygen evolution reaction have to be catalyzed. Platinum has historically been known to be the top performing catalyst for hydrogen evolution reactions. However, platinum is incredibly expensive and is in short supply. Studies to use metal sulfide MoS_2 as a catalyst for water splitting was initially determined to be unfeasible as early as the 1970s. This was due to the observation of MoS_2 electrode undergoing degradation to sulfates using the oxygen that was being generated.[7] However, it was later recognized that nanosized MoS_2, unlike bulk MoS_2, can satisfactorily catalyze the hydrogen evolution reaction. This was proven both theoretically and experimentally.[8, 9] Figure 2 depicts the catalysis of hydrogen evolution reaction on a layer of MoS_2.
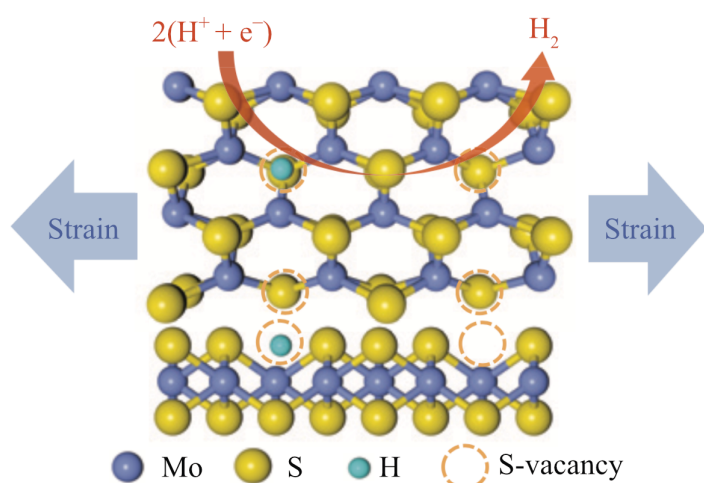

Figure 2. Li et al. demonstrated the activation and optimization of a layer of MoS_2 to be able to catalyze hydrogen evolution reaction through introduction of sulfur vacancies and strain. On the basal plane, S-vacancies function as the active sites and the application of strain further enhances it. Reproduced with permission.[9]

Faber et al. synthesized and studied micro and nano structured CoS_2 as a high-performance electrocatalyst for the hydrogen evolution reaction. They demonstrated a morphology dependent enhancement in activity and stability, with nanostructured CoS_2 exhibiting the highest catalytic activity and stability.[10] As most reported transition metal catalysts have been shown to catalyze one-half of the water-splitting reaction, either the hydrogen evolution reaction or the oxygen evolution reaction. A recent work by Lee et al., has shown bifunctional hollow CoS_x nanoarrays and Ni-Fe based layered double hydroxide nanosheets (NiFe LDH) as an efficient catalyst for both reactions. The metal-organic framework (H-CoS_x@NiFe LDH/NF) provides a strong coupling interaction between hydrogen evolution reaction CoS_x and oxygen evolution reaction active NiFe LDH ensuring catalysis of both halves of the process.[11] Wang et al. use a CoS_2-MoS_2 heterostructure to catalyze both the hydrogen evolution reaction as well as the oxygen evolution reaction, which when assembled as a two electrode cell delivers a cell voltage of 1.52V at 10 mA cm^{-2}.[12] Huang et al. similarly demonstrate a hetero catalyst composed of mesoporous CoS-MoS_2 active in catalyzing both the hydrogen evolution reaction and the oxygen evolution reaction with a cell voltage of 1.61 V at 10 mA cm^{-2}.[13]

1.1.2 Synthesis techniques of metal sulfide nanoparticles

Metal sulfide nanoparticles can be synthesized in several ways. The processes and methods described here are by no means exhaustive but cover the more prominent ones used. There are numerous reported methods to produce different types of metals sulfide nanoparticles – mono-metal sulfides, bi-metal sulfides, multi-metal sulfides, composites, doped sulfides and heterostructures.

Synthesis of metal sulfide nanoparticles through chemical precipitation is a commonly used technique. It involves transforming a supersaturated solution of dissolved components into insoluble solids. This can be a very simple synthesis as seen in the work by Khan et al. where CdS nanoparticles were synthesized by vigorous stirring of cadmium nitrate and sodium sulfide. The precipitate is collected and washed after which powder form of CdS is obtained.[14] It can also be used to synthesize binary metal sulfide nanoparticles. Kaur et al. synthesized ZnS nanoparticles incorporated with copper in this manner. Zinc acetate and copper acetate salts were made into separate solutions using ultra-pure water. They were then combined with sodium sulfide and a capping agent and left to react for 3 hours at 80°C. Here too the precipitate is washed, dried, and crushed to obtain fine powder.[15] To obtain nanoparticles, hot injection precipitation is a preferred form of the synthesis method. The high reaction temperatures assist in rapid sulfur release and nucleation of nanoparticles resulting in uniform crystal nucleation and growth.[16] Joo et al. demonstrates this with the synthesis of PbS, ZnS, CdS and MnS nanocrystals. They were able to produce monodisperse nanocrystals in varying sizes which are depicted in Figure 3.[17] Lee et al varied the growth temperature to show shape evolution of PbS nanostructures including monopods, I-shaped bipod, L-shaped bipod, T-shaped tripod, cross-shaped tetrapod, star-shaped nanocrystal and truncated octahedrons.[18]
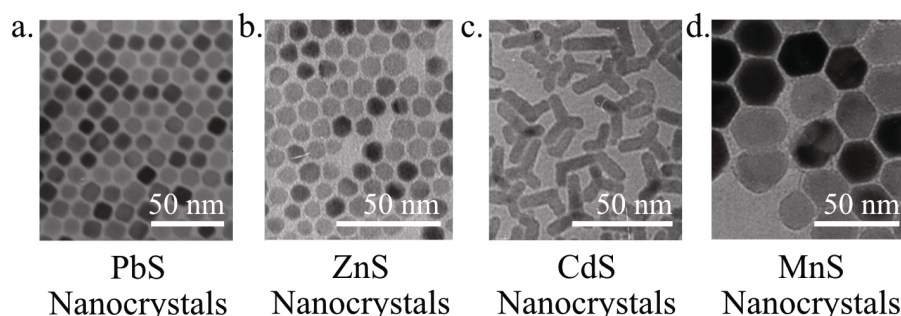

Figure 3. Monodisperse nanocrystals of PbS, ZnS, CdS and MnS synthesized through precipitation. Reproduced with permission.[17]

Ball milling is a relatively easy mechano-chemical synthesis process. IUPAC defines a mechano-chemical synthesis as a chemical reaction induced by direct absorption of mechanical energy and mentions shearing stretching and grinding as typical methods to do so.[19] The set-up is made usually of stainless steel balls in combination with a milling chamber is used to produce nanoparticles of size 4-24 nm. High energy collisions from the balls in the milling facilitate this. Ball milling has been used to create both mono sulfides and binary sulfides. Chin et al. produced FeS_2 and FeS nanoparticles. They experimented with the starting material, using bulk FeS_2 as well as elemental Fe and S to create the metal sulfide nanoparticles.[20] Dutková et al. have demonstrated the production of bi-metal sulfide through ball milling creating Cu_2SbS_4 with crystallites of size 14nm and 10 nm.[21]

A versatile and frequently used technique to produce many kinds of nanoparticles is hydro/solvo-thermal synthesis. In hydrothermal synthesis, water is used as the precursor medium to metal salt and sulfur source before being heated in medium to high temperatures in a steel autoclave. In solvothermal synthesis, organic solvents are used instead of water. Nanostructured metal sulfides of varying geometries can be prepared but most require post treatment for purification and increase in crystalline quality. Dong et al. demonstrate the variation in geometry of synthesized CoS by variation in ratios of reactants and solvents. They used a solvent mixture of water and ethanol in varying ratios. The resulting nanostructures are shown in Figure 4. Reduction in the water to ethanol ratio used in the process creates well defined individual morphologies, indicating a high degree of control of morphology through the varying of select parameters.[22] In a similar manner Kundu et al. also show the variation in structure on varying the water to ethanol concentration of the solvent. With pure water as solvent, CdS spheres composed of 2D nanoplates form. When small amounts of ethanol are

added along with water as the solvent, CdS spheres appear to be built from 1D nanorods. Interestingly, when the concentration of water to ethanol is 1:1 the CdS spheres composed of 0D nanoparticles are observed.[23] As hydrothermal synthesis is a versatile technique, sulfide nanoparticles of many metals have been synthesized using this method. Ikkurthi et al. synthesized nanostructured CoS, CuS, FeS and NiS supported on nickel foam. More complex metal sulfide nanoparticles have also been synthesized through hydrothermal synthesis such as cobalt ruthenium sulfide (Co_2RuS_6) by Bolagam et al.[24]
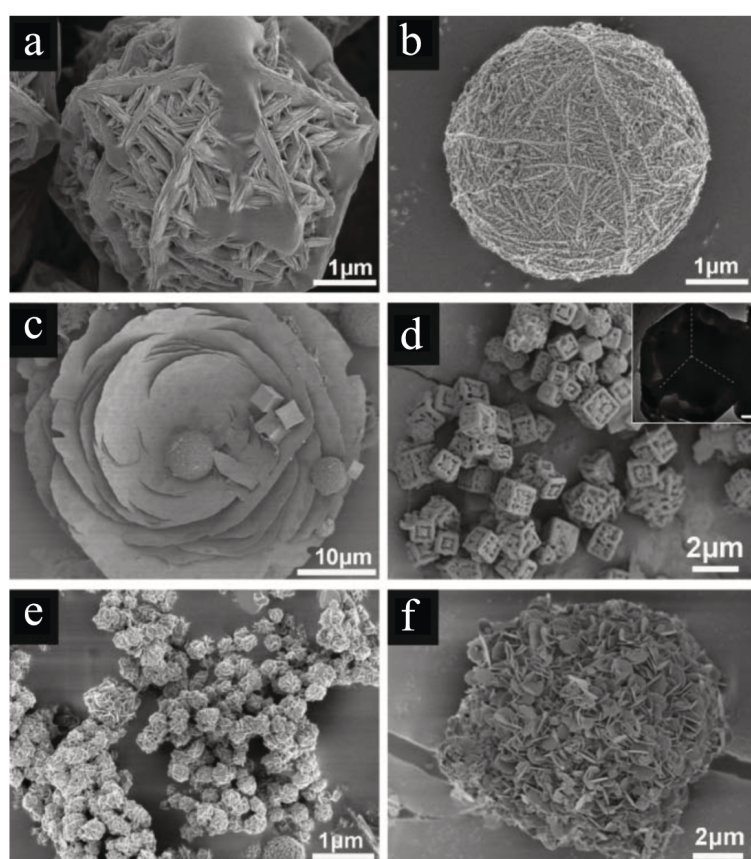

Figure 4. Effect of varying of water to ethanol ratio in creating CoS particles with differing morphologies through solvothermal synthesis. Water to ethanol ratios of (a) 9:1 (b) 7:3 (c) 5:5 (d) 3:7 (e) 1:9 and (f) pure ethanol. Reproduced with permission.[22]

Microwave and ultrasound assisted synthesis introduce high amounts of energy in a short time duration to and can be used to produce metal sulfide nanoparticles. Similar to precipitation synthesis, homogeneous reaction conditions result in uniformity of the products formed. Microwave assisted liquid-phase synthesis is known to suppress side reactions hence having a positive effect on yield. The short penetration depth of microwave irradiation is however limiting in enlarging the size of microwave reactors and hence an issue for large scale synthesis.[25]

1.2 Combustion synthesis

Combustion synthesis through a flame spray set-up is an established route to produce metal oxide nanoparticles on a large scale. This method of synthesis of nanoparticles has several advantages as compared to wet chemical synthesis techniques. It is very common to require a post processing in wet chemical techniques to remove any impurities left over after synthesis. In the flame spray set-up post processing can be avoided as excess solvent or reagent is burned away and particles can be collected as such making it a single step production process. It is also a faster route of synthesis with larger yields in comparison to liquid phase synthesis. The production of metastable phases is made possible by rapid thermal quenching happening during the production process with high temperature gradients and low residence time are.[26]

The process of using combustion to create particles is in general known as aerosol flame synthesis. Depending on the physical state of the starting material that is pushed into the set-up this can be divided into two – liquid-fed and vapour-fed. In the vapour fed process, volatile precursors are evaporated and fed into the flame set-up. This is a limiting process as highly

volatile precursors for many metals are hard to come across. In the liquid-fed process, depending on if the starting precursor solution is combustible or non-combustible, it is known as flame spray pyrolysis or flame-assisted spray pyrolysis. The advantage of using combustible precursor solutions is that is proven to be highly repeatable for the formation of homogenous nanoparticles.[27]

The flame spray pyrolysis set-up using combustible liquid precursor solution mix is shown in Figure 5. The precursor solution is fed into the nozzle of the set up and atomized into small droplets by the dispersion gas. This formation mechanism of particles through this process can be through two different routes. One of the paths is gas-to-particle formation and the other is droplet to particle formation. It is assumed that one of the two routes dominates the entire process and it usually depends on precursor-solvent properties combustion set-up parameters.[28] In gas-to-particle mechanism, nanoparticles are formed and are primarily perceived to occur when using highly combustible precursor-solutions. On ignition of the droplets in the flame, precursor vapour is formed, which then reacts to form product vapour. From here nucleation and/or coagulation leads to the formation of nanoparticles. Gas-to-particle formation can also proceed with an ignited droplet undergoing superheating and exhibiting micro explosions. This is assumed to happen due to the preferential evaporation of the more volatile component from the droplet surface, and some of it becomes trapped in the inner core of the droplet. The trapped component becomes superheated causing a rapid internal build-up of pressure causing the micro explosion. Droplet-to-particle mechanism is predominantly observed in flame-assisted spray pyrolysis where non-combustible precursor-solutions are used which can led to the formation of hollow shell-like particles or micrometer sized particles.[28]
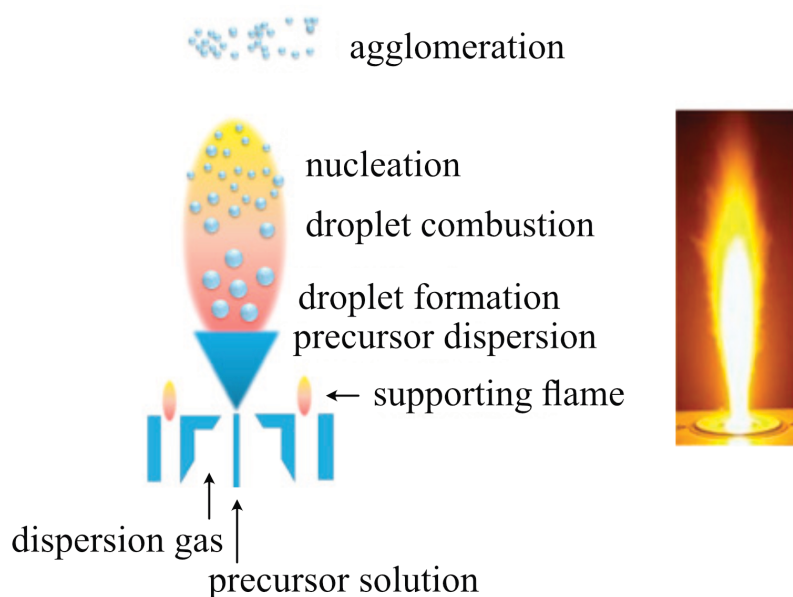
Figure 5. Flame spray set-up schematic with an insert showing a real flame spray set-up. Reproduced with permission.[29]

1.2.1 Flame combustion synthesis of metal sulfide nanoparticles

In literature there are 3 publications to be found that until 2022 that specifically use flame spray combustion to produce metal sulfides. In the first publication seen from 2010, Athanassiou et al. synthesize Mn^{2+} doped ZnS using flame spray combustion. The starting precursors used were zinc 2-ethylhexanoate, manganese naphthenate, tetrahydrothiophene and tetrahydrofuran as solvent. The ratio of sulfur to zinc used is 5:1 and the ratio of manganese to zinc is 1/100 at. % with a total metal concentration of 0.25 mol/L. This solution is atomized and pushed into a premixed flame of methane and oxygen. Here, the flame is enclosed in a porous metal tube to allow stable combustion. It is stated here that the temperature gradient and chemical composition of gaseous species is crucial in determining the chemical composition of the nanoparticles created. The assumption is also made that H_2S is the major contributor of sulfur in the gas phase. A mass spectrometer is used to monitor the concentration of combustion gases H_2, CO_2, H_2O, NO_x, CH_4 and O_2.[30]

PbS-TiO$_2$ heterojunction nanoparticles were synthesized by Bubehofer et al. using flame spray combustion. Here, the structure formed is very interesting. TiO$_2$ nanoparticles function as a support on which even smaller particles of PbS form. Confirmation of composition of the produced powders is done through X-ray diffraction. This unique structure is however well established with noble metals such as platinum and gold as small particles on metal oxides when manufactured through flame spray combustion synthesis. Mädler et al. synthesized Au particles supported on TiO$_2$ and SiO$_2$ nanoparticles. The reasoning behind this structuring is that the concentrations of titania and silica are much higher than that of gold and late nucleation along with little coagulation renders the Au particles a narrower size distribution. Also, metal oxides that are functioning as support to the Au particles nucleate faster. Johannessen and Koutsopoulos, in a similar manner, synthesized platinum supported on TiO$_2$ nanoparticles. Here too the process is described happening with the more stable TiO$_2$ nucleation and at lower temperatures away from the flame nucleation of Pt particles takes place.[31] Strobel et al. in an equivalent approach synthesized similarly structured Pd nanoparticles supported on Al$_2$O$_3$ nanoparticles.[32] Strobel et al. synthesized Pt supported on Al$_2$O$_3$ and its catalytic properties for hydrogenation reactions were studied. [33] Bubenhofer et al. would hence be the first and only till date to show this structuring is possible with non-noble metals (Pb) in addition to being the first to show this structuring with PbS and through flame spray combustion synthesis. The precursors used titanium isopropoxide, lead-2-ethylhexanoate and thiophene as the sulfur source. A mixture of these precursors with a Pb to S ratio of 2.5 and varying ratios of Pb to Ti with keeping the total metal concentration in the solution at 4 wt.% was made and fed into the flame spray set-up. A mixed oxygen/nitrogen (4 L/min/ 1 L/min) dispersion gas was used. Similar to Athanassiou et al., it is assumed that H$_2$S is the main contributor of sulfur in the gaseous phase.

Wang et al. produces mesoporous mono and binary metal sulfides using the flame combustion process. In this study, they intended on creating a template free method and scalable method to produce mesoporous metal sulfide nanoparticles. Herein they have shown to produce Co_9S_8, Ni_3S_4, and $NiCo_2S_4$, nanoparticles. Although the abstract mentions that FeS nanoparticles are also synthesized, it is unreported in the paper. As precursor, metal acetylacetonates combined with thiourea is used although amounts are difficult to ascertain. Precursors are mixed into methane and xylene, the ratio of which is also unclear. In the final step 18 wt.% of liquified propane is added and the solution heated to 50-60 C before pushing the precursor solution combination into atomization nozzle. A diffusion flame was supported with 3 L/min high purity oxygen and surrounded by 20 L/min inert gas, presumably argon. The flame was isolated from ambient environment using a quartz shroud. The composition of produced particles is characterized using X-ray diffraction and TEM diffraction. The electrochemical performance of the synthesized materials were also studied.[34]

1.3 Single droplet combustion studies

Single droplet combustion studies for the creation of metal oxides were done to analyze and understand the processes happening on the micro scale that was leading to the formation of metal oxide nanoparticles. This is because, in the large-scale process of flame spray combustion the precursor solvent solution is atomized into micro droplets and hence in a simplified manner can be observed as a collective of individual burning droplets. As burning behaviour of precursor solvent solutions was unknown in comparison to multi component fuel droplets, Rosebrock et al. initially conducted experiments on pure xylene, ethanol, heptane and dodecane.[35] Combustion of droplets has been used for a longtime to study liquid fuels especially in spray injection systems. One of the first works looking specifically at combustion

of individual droplet which was intended to study fuel sprays was done by Godsave in 1949 and is portrayed in Figure 6.[36]
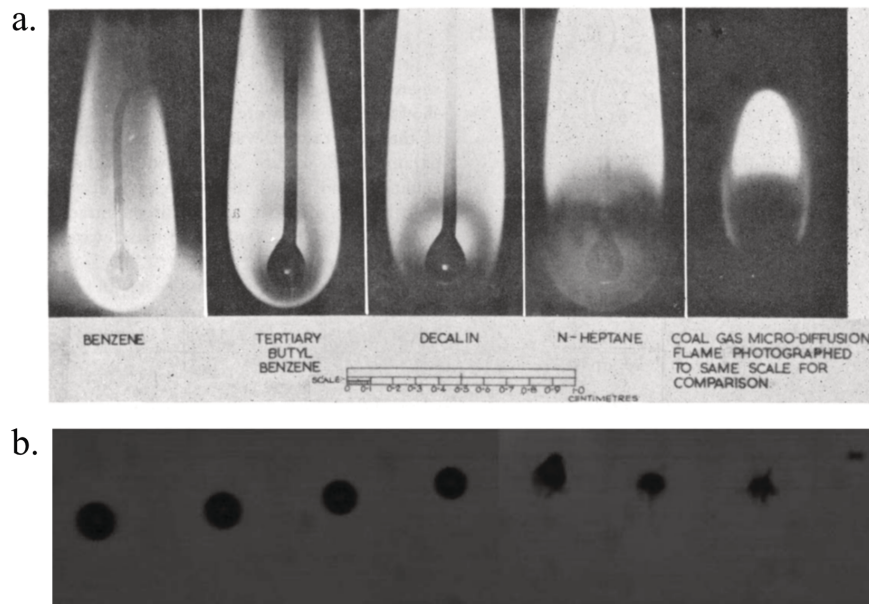

Figure 6. Godsave's work on droplet combustion observing burning of suspended droplets using direct photographs. b.) From the work of Rosebrock et al., an image sequence of the burning of a 100 μm droplet of tin 2-ethylhexanoate in xylene used to study formation of metal oxide nanoparticles. The time interval between consecutive droplets is 621 μs. Both are reproduced with permission. [35, 36]

Rosebrock et al. used a piezoelectric droplet generator to produce micrometer sized monodisperse droplets. These monodisperse droplets are supported with a co-flow of oxygen to prevent fluctuations in droplet trajectory. The end of the droplet generator is connected to a solution reservoir that contains the precursor solvent solution. The droplets generated by the piezoelectric generator are ejected into a cuvette where they are then ignited by tungsten electrodes using a synchronized spark. In the work, they compare combustion of droplets of pure solvents with those containing metal precursors. A major difference seen is the formation of vapour bubbles that in turn expand and burst the droplets.

One of the metal sources Rosebrock et al. work with is zinc nitrate hexahydrate which is combined with ethanol as solvent. In the single droplet experiment, it shows a dried-up impact of where the single droplet hit the TEM grid before complete combustion. Whereas, when the same solution of zinc nitrate hexahydrate and ethanol were combusted on a pilot spray flame set-up, a mixture of spherical and rod like nanoparticles are likely obtained due to the higher temperatures in a spray flame set-up. They note that it is unreported in literature for precursor solutions containing zinc nitrate to produce hollow particles in combustion. For another metal source, zinc naphthenate which was used in combination with xylene as a solvent, showed particle formation through single droplet combustion. Interestingly, the morphology of zinc naphthenate in xylene on combustion through the spray flame set-up was similar to that of zinc nitrate hexahydrate and ethanol in the spray flame set-up as well. This shows that there could very well be a small difference seen when comparing single droplet combustion to spray flame combustion. Conversely, the similarities between nanoparticles produced through single droplet combustion and spray flame combustion are well documented. The authors observed that neither zinc nitrate hexahydrate nor zinc naphthenate vapourize directly but rather form a shell. The high decomposition temperatures such as that of zinc naphthenate allow for the solvent to superheat and hence leading to the micro explosions that were observed.[37]

Li and colleagues studied the comparison of production of tin oxide nanoparticles through flame spray pyrolysis and single droplet combustion. As direct flame investigations are challenging due to a number of factors such as short time scales, turbulence caused by dispersion, interaction of droplets, high flame temperatures and steep temperature gradients, they use single droplet combustion to understand the droplet-to-particle formation. The authors use the same precursor-solvent combination of Tin (II) ethylhexanoate and xylene in flame spray pyrolysis set-up and single droplet combustion set-up. The particles produced through

combustion on the flame spray set-up were seen to be highly agglomerated and contain particles with a wide size distribution. The single droplet combustion produced particles that were either large rectangular or small and almost spherical nanoparticles. It is considered that the particles form via gas-to-particle conversion which is attributed to the observation of homogenous nanoscale particles. Morphology of particles produced were analyzed using TEM and are depicted in Figure 7. The variation of metal concentration in the precursor solutions caused changes in the average size of particles produced. With particles produced using flame spray, an increase in size was observed on increasing concentration. Size distribution of particles was also noted to widen with increasing concentration. While the larger particles produced using single droplet combustion displayed similar behaviour, size of small particles produced using single droplet were less impacted with varying concentration and only showed small fluctuations. Li et al. were unable to verify the droplet explosions observed in single droplet combustion on the flame spray set-up. These observations, although difficult to spot directly in a spray set-up, have been experimentally shown to occur to droplets in the combustion of liquids. Explosions in fuel emulsions on spray combustion is documented in multiple works.[38-41]. Micro-explosions have been recently visualized in flame spray of metal precursor solutions confirming their existence in droplets of both flame spray set-up and single droplet set-up.[42] Li et al. hypothesize that the large size differences in observed particles are caused by the disintegration of large precursor droplets.
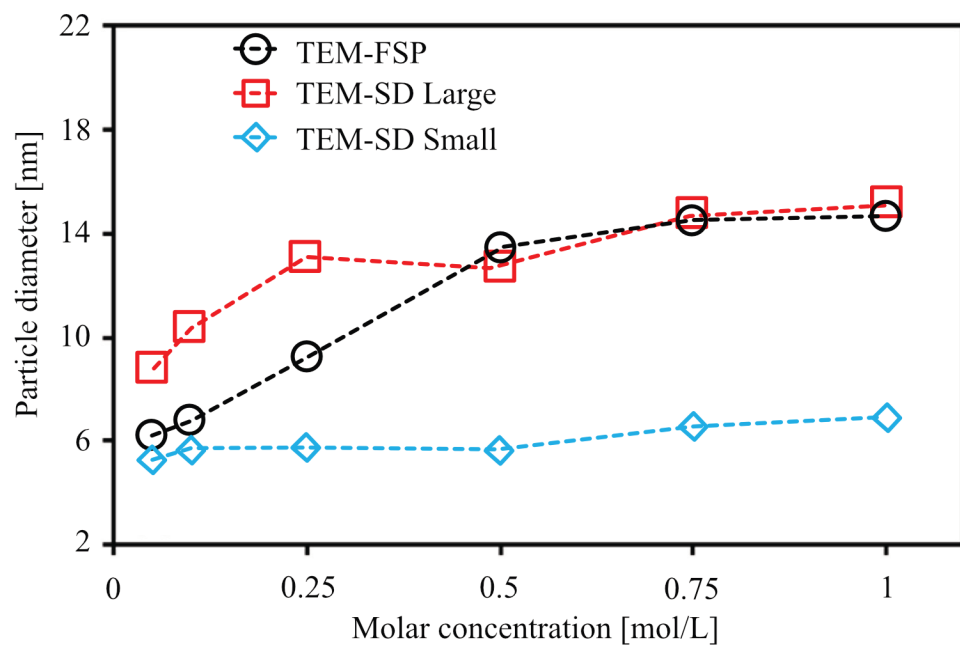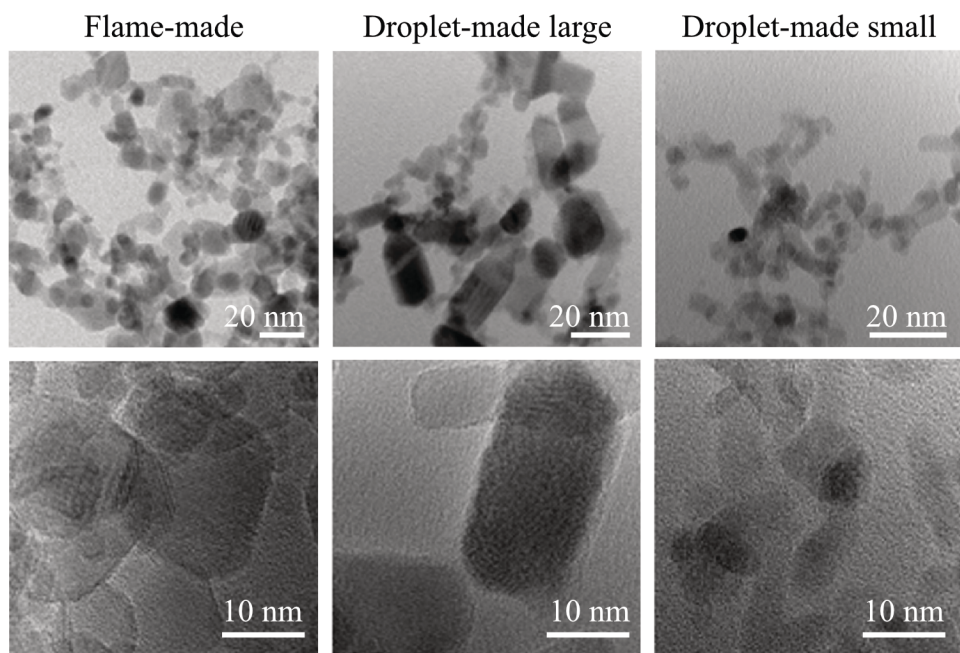
Figure 7. TEM characterization of nanoparticles obtained from the combustion of Tin (II) ethylhexanoate and xylene through flame spray pyrolysis and single droplet combustion. The graph represents variation in particle diameter with changing concentration produced by both flame spray pyrolysis (FSP) and single droplet (SD) combustion. Reproduced with permission.[43]

1.4 Challenges to producing sulfides through combustion

The biggest challenge in producing metal sulfides through the combustion process is to avoid the formation of metal oxides. For spray flame combustion synthesis, it is known that sufficient oxygen is required to produce the metal oxide nanoparticles while avoiding soot formation from incomplete combustion. It is also known that when trying to produce metal sulfide nanoparticles through combustion, sulfur atoms have to compete with oxygen for the metal ions and hence it would be necessary to supply an excess amount of sulfur.[30] The sulfur source ideal for combustion synthesis, whether in gaseous, liquid or solid form is unknown. The sulfur source used needs to be able to provide sulfur atoms in excess of the amount of oxygen that is theoretically present during the process to avoid oxidation of metal ions to metal oxides. It is currently unclear how the sulfur atoms interact and successfully bind with metal ions to produce metal sulfide nanoparticles through combustion.

1.5 Thesis structure

This thesis starts with the lookout for ideal sources of sulfur that can be used within precursor solution mixtures that are created to undergo combustion. As small-scale high-throughput studies are used as a groundwork to large-scale combustion synthesis, materials used are chosen to be economically viable. As the focus is to start with highly combustible precursor solutions, choosing a sulfur source that is combustible, avoids incorporation of undesired species into the final product and dissolves in a wide number of solvents is desired.
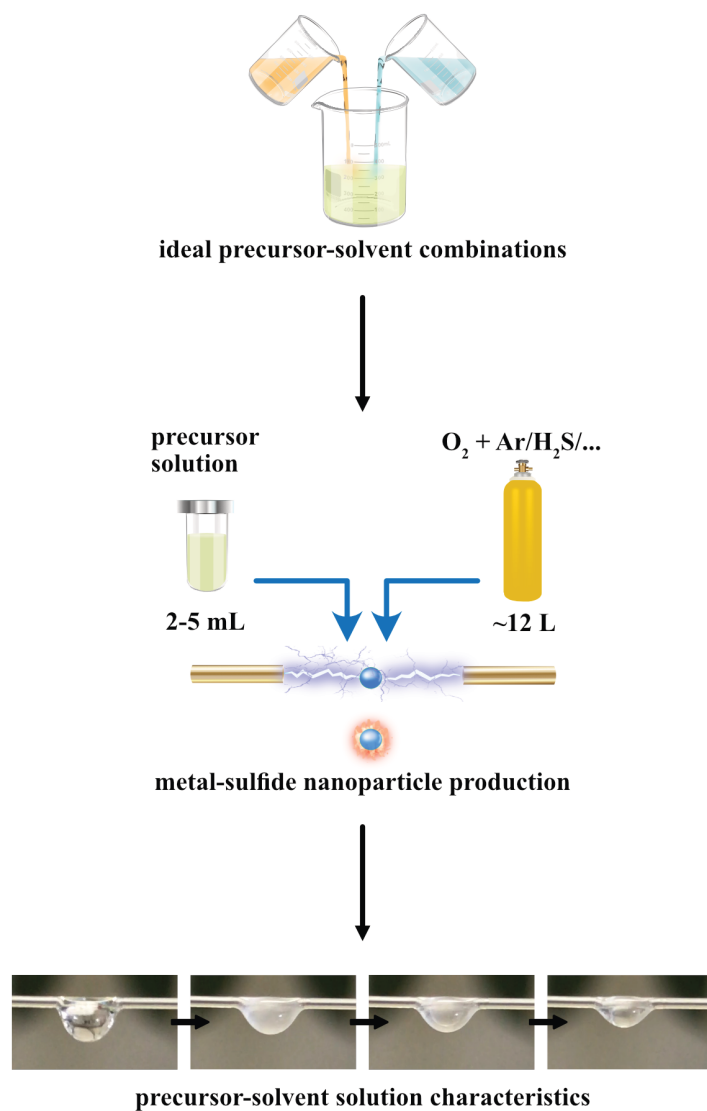
Figure 8. Schematic representation of precursor-solvent solutions being tailored for the production of metal sulfide nanoparticles through combustion and insights into their characteristics and behaviours leading to formation of the nanoparticles can be obtained through creative use of established characterization techniques.

The formulation of different metal-sulfur precursors brings about the need to identify fitting metal sources or classes that can reliably perform, as in producing metal sulfide nanoparticles. Here, an understanding of processes that are prone to take place during the formation of nanoparticles are also explored from a precursor-solution perspective. The understanding of how-to tailor nanoparticles comes from the understanding of mechanisms behind the formation

and hence, the interactions that take place are to be determined. The products and the processes are used together to hypothesize molecular scale mechanisms and reaction pathways that take place in the creation of metal sulfide nanoparticles through combustion of metal-sulfur precursor solutions. The process of creation of metal sulfide nanoparticles through combustion is a new area where literature is also limited as seen in section 1.2.1. The contributions this thesis intends on making is to provide insight into the process of creation of metal sulfide nanoparticles through utilizing a number of processes to study precursor solution combinations.
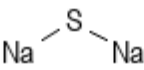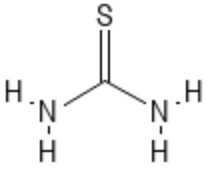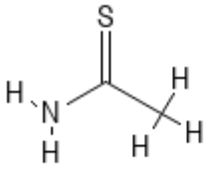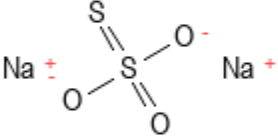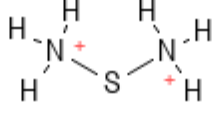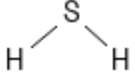
Chapter 2.
Materials & Methods

2.1 Determination of sources of sulfur

There is a plethora of compounds available that can act as a potential source of sulfur. These can range from sulfur itself to organic and inorganic compounds that contain sulfur. They can also range in forms from being solid at ambient temperature to liquid as well as differ in the number of sulfur atoms per molecule of compound. Sulfur itself can also function as a source. Although it is an abundant element, as a mineral it is usually found in sulfides and sulfates. In nature, sulfur is also abundant and plays an important role. This is seen in proteins such as keratin, which derives its strength from the disulfide bonds which are formed between the thiol groups of the peptide cysteine and plays a prominent role in hair, nails, and epidermal layer of the skin. As the focus here is to create liquid metal-sulfur precursor combinations, an analysis of sulfur sources used to produce metal sulfide nanoparticles through liquid phase synthesis was done. Here, 100 randomly picked peer-publications on the same were used and the resulting analysis is seen in Table 1.

Table 1. The following table gives an insight into sulfur sources commonly used in liquid-phase synthesis of 0D metal sulfide nanoparticles that use a single source of sulfur.

No.	Name	Structure
1	Sodium sulfide	
2	Thiourea	
3	Thioacetamide	
4	Sulfur powder	
5	Sodium thiosulfate	
6	Dodecanethiol	
7	Ammonium sulfide	
8	Hydrogen sulfide	
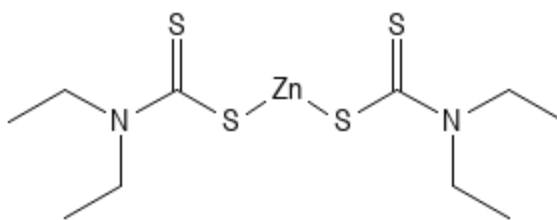
9	Zinc diethyldithiocarbamate	
10	Thioacetic acid	
11	Tetrahydrothiophene	
12	Thiosemicarbazide	
13	Sodium diethyldithiocarbamate	
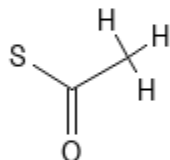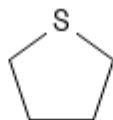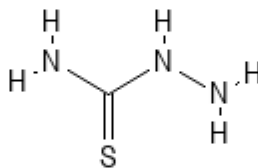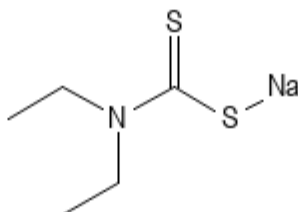
From the analyzed publications, sodium sulfide is by far the most used source of sulfur in liquid-phase synthesis. Na$_2$S is used in multiple other applications ranging from flotation of oxide minerals to processing of leather.[44, 45] It is synthesized by reducing sodium sulfate as seen in the following reaction[46] -

$$Na_2SO_4 + C \rightarrow Na_2S + CO_2$$
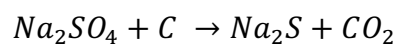
Sodium sulfide can also be made in the laboratory in a redox process that involves the reaction of sodium with sulfur –

$$Na + S \rightarrow Na_2S$$
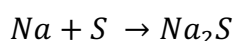
However, it is a compound that can be purchased directly from established chemical suppliers which eliminates the need to produce it in-house. Na^+ is a highly soluble monovalent cation which can easily undergo an ion exchange reaction. This makes it an attractive source of sulfur in liquid-phase reactions to produce metal sulfide nanoparticles. Similarly, sodium thiosulfate also has two Na^+ ions present. It is used comparatively less than sodium sulfide which is probably due to the fact that the disassociation of the sulfur atom in sodium thiosulfate requires high temperatures or treatment with acids.[47]

Thiourea is a white, odourless solid with a sulfur atom and is highly nucleophilic. Thiourea and its derivatives have applications in a wide variety of areas – pharmaceuticals, insecticides, plastics, textiles, dyes etc.[48] Thiourea is mainly produced by the reaction of calcium cyanide with hydrogen sulfide:[49]

$$CaCN_2 + 2H_2S \rightarrow Ca(SH)_2 + (NH_2)_2CS$$
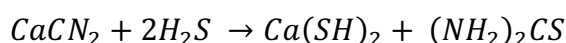
Thiourea and thioacetamide are seen as two most used sulfur sources in wet chemical synthesis after sodium sulfide. Both compounds have the same physical appearance and are soluble in water and ethanol.

Sulfur powder is commercially produced in large quantities. It is mainly through processes that separate sulfur byproducts in the petrochemicals industry. When sulfur-contaminated petrochemicals are burnt, they produce pungent-smelling sulfur dioxide fumes which would eventually fall back onto earth as acid rain. Curtaining this resulted in the extensive filtering out of sulfur containing byproducts before burning. In the production of nanoparticles, it is

most used in combination with oleylamine as a solvent. It is a colourless oil also known for its use as a surfactant which aids in controlling size and shape of produced nanoparticles.

Dodecanethiol, ammonium sulfide and tetrahydrothiophene are sulfur sources in the liquid form. The benefit of using sulfur sources in liquid form is that they can dissolve appropriate metal salts without the need of an additional solvent. This is useful to have higher ratios of metal to sulfur if needed. Hydrogen sulfide is the only one here used in the gaseous form. Storage and handling of hydrogen sulfide requires special attention as it is highly explosive and exposure above a certain threshold can even result in death.

Zinc diethyldithiocarbamate is used as both source of sulfur as well of metal ion. The limiting factor is the set ratio of metal to sulfur. To be able to vary the concentration of sulfur when utilizing a single source precursor, a additional sulfur source will need to be used. Sulfur sources that are enticing are organic compounds that contain only S, C and H which reduce the probability of contamination in final products. Compounds such as hydrogen sulfide, tetrahydrothiophene and dodecanethiol fit this description.

2.2.1 Combination with metal sources

The metal precursors used in combination with the sulfur sources considered above are shown in Table 2. These are specifically to produce 0-D nanoparticles.

Table 2. Metal precursors used in conjunction with sulfur sources shown in Table 1. Indicated here are also the forms in which the sources are present - solid (*), liquid (†) or gaseous (#) form.^

Sulfur Source	Metal source	Preparation technique	NPs	Application	Ref
	cadmium nitrate	stirring for 12 h with glucose as a capping agent	CdS	studies on dielectric properties	[50]
	copper anode	electrochemical synthesis: metal source as anode and sulfur source as part of the electrolyte	Cu_2S	Improving solution synthesis of Cu_2S	[51]
	zinc nitrate + ferrous sulfate	stirring at 293K with methanol as solvent	$Zn_{1-x}Fe_xS$	studies on magnetic and electrical properties	[52]
	nickel anode	electrochemical synthesis using a steel cathode∞	NiS	studies on optimizing synthesis conditions	[53]
	cadmium acetate	solution of metal source with capping agent heated, cooled down and sulfur source stirred in	CdS	photodegradation of dyes	[54]
	cadmium chloride	sulfur source added to the metal source, sodium hydroxide and mercaptoacetic acid solution accompanied by bubbling nitrogen	CdS	oligonucleotide label	[55]
	cadmium chloride	sulfur source added under argon, metal precursor dissolved in degassed and distilled water and stirred	CdS	studies on size dependence of spectroscopic and electrical properties	[56]
Sodium Sulfide*	zinc nitrate	precursor solutions made with distilled water and then stirred for 1h	ZnS	studies on photoluminescence emission	[57]
	cadmium acetate	sulfur source added dropwise to an ethanol solution of the metal source	CdS	studies on photoluminescence and photoconductivity	[58]
	zinc nitrate + manganese acetate	sulfur source added dropwise to a distilled water solution of metal sources	ZnS:Mn	studies on doping effects on photoluminescence	[59]
	lead nitrate	metal precursor dissolved in degassed and distilled water and sulfur source added under argon and stirred	PbS	electrochemical biosensor	[60]
	cadmium nitrate	sulfur source and additional capping agent added to solution of deionized water and metal source	CdS	studies on formation of nanoparticles in aquatic environment	[61]
	silver nitrate	sulfur source added dropwise to a solution of metal source at 80°C and PVP solution added to this when temperature drops to 60°C and stirred for 3h	Ag_2S	studies on properties of doped and undoped Ag_2S	[62]
	copper nitrate	solutions of sulfur source and metal source made with distilled water and added dropwise into PVA-distilled water solution	CuS	studies on nanoparticle in PVA film	[63]

	cadmium perchlorate	sulfur source solution and metal source solution made separately using heptane	CdS	studies on selective photoetching properties with a surrounding silica shell	[64]
	palladium chloride	aqueous solution of metal source, sodium chloride, sodium borohydride and sulfur sources autoclaved along with a carrier	Pd$_4$S	studies on support for nanoparticles	[65]
	silver nitrate	metal source and sulfur source in combination with sodium citrate or sodium salt of ethylenediaminetetraacetic acid was left to react for three days	Ag$_2$S	studies on synthesis conditions and size in colloidal solutions	[66]
	copper chloride	sulfur source stirred into metal source, cetyltrimethylammonium chloride and water for 15 min at 90℃ to obtain coated nanoparticle	CuS	photothermal cancer therapy	[67]
	zinc acetate	reaction in solution with metal and sulfur source with the addition of a stabilizer	ZnS	studies on photocatalytic properties	[68]
	zinc nitrate	metal source and sulfur source added to aqueous buffer solution	ZnS	studies on precipitation in environmental conditions	[69]
	cadmium acetate	solutions of sulfur and metal source made using deionized water, one added to the other and heated	CdS	studies on interaction with ATP	[70]
Sodium Sulfide[*]	copper sulfate	aqueous solution metal source and sulfur source mixed with stabilizing agent	Cu$_x$S	studies on quantum effects of nanoparticles	[71]
	zinc sulfate	metal source solution with N-cetyl-N, N, trimethyl ammonium bromide added dropwise into sulfur source	ZnS	studies on effects of capping agent on surface properties	[72]
	cadmium nitrate	metal source and sulfur source solutions in methanol added into dendrimer solution	CdS	studies on luminescence properties	[73]
	cadmium nitrate	sulfur source dissolved in water and added to metal source and sodium hexametaphosphate solution in deoxygenated water and stirred	CdS	studies on DNA on nanoparticle emission	[74]
	iron chloride/ ammonium iron (II) sulfate	metal source and sulfur source solutions added into dendrimer solution	FeS	studies on nanoparticle deposition on silica gel	[75]
	ferrous sulfate	sulfur source in deionized water added to a solution of metal source in deionized water along with sodium carboxymethyl cellulose	FeS	studies on soil dispersibility and removal of mercury from water	[76]
	sodium gold sulfite	aqueous solutions of metal source and sulfur source were mixed for 24h	Au$_2$S	studies on synthesis and optical properties	[77]
	cadmium chloride	metal solution is mixed with diethylene triamine solution and manganese chloride solution is added. Double distilled water is used as	CdS:Mn	Studies on characteristics of Mn2+ doped cadmium sulfide nanoparticles	[78]

		solvent. Sulfur source is finally added dropwise			
	zinc acetate + manganese chloride	aqueous solutions of metal sources and sulfur source mixed with capping agents	ZnS:Mn	studies on photoluminescence emission	[79]
	cadmium sulfate	sulfur source solution added to metal source solution with acetic acid and capping agent	CdS	studies on using Bovine Serum Albumin as the capping agent	[80]
	cadmium nitrate	aqueous solution of metal source and sulfur source strongly stirred	CdS	studies on optical and dielectric properties	[14]
	zinc acetate	sulfur source solution was added to prepared metal source and copper acetate solution in ultrapure water and heated to 80°C for 3h	ZnS:Cu	photocatalysis	[15]
	zinc acetate + manganese acetate	aqueous solution of sulfur source added to solution of metal sources and stirred vigorously	ZnS:Mn	studies on photoluminescence emission	[81]
	zinc acetate	metal source and sulfur source milled together in a planetary ball mill	ZnS	studies on synthesis and optical properties	[82]
Sodium Sulfide[*]	cadmium chloride	metal source added to sulfur source, sodium hydroxide and methanol	CdS	studies on synthesis and optical properties	[83]
	zinc chloride	sodium sulfide and mercaptoethanol was added to metal source solution	ZnS	studies on synthesis and photoluminescence properties	[84]
	zinc sulfate	aqueous solution of metal source and sulfur source mixed vigorously	ZnS	studies on structural properties	[85]
	lead nitrate	sulfur source added to metal source solution in mercaptoacetic acid and pH adjusted with sodium hydroxide	PbS	studies on nanoparticle label for biological applications	[86]
	calcium chloride	sulfur source was added to metal source solution, where both use absolute ethanol as solvent	CaS:Fe	Ferromagnetic nanoparticle for cancer hyperthermia	[87]
	copper chloride	aqueous sulfur source solution added to a solution of metal source solution and sodium citrate	CuS	therapeutics for atherosclerosis	[88]
	unspecified calcium halide salt	sulfur source and thioglycerol solution made in ethanol, metal source solution and europium nitrate solution also made with ethanol and sintered at high temperature	CaS:Eu	studies on fluorescent properties	[89]
	calcium chloride	sulfur source and triethanolamine solution in 2-propanol added to metal source solution in 2-propanol	CaS	studies on luminescence of capped nanoparticle	[90]
Thiourea[*]	nickel nitrate	metal source and sulfur source solution made by spraying solution into furnace held at 800°C	NiS	studies on comparison of electrochemical properties of pure metal sulfide with metal sulfide-RGO composite	[91]

	cobalt chloride	metal sulfur source and sulfur source solution in methanol autoclaved at 180°C for 24h	CoS	studies on electrochemical properties for potential application as pseudocapacitors	[92]
	zinc nitrate, cadmium nitrate, lead nitrate, copper nitrate, iron sulfate and bismuth nitrate	metal source solution made using deionized water (bismuth dissolved in 5% nitric acid) to which sulfur source is added and passed through a continuous flow reactor at high temperatures	ZnS, CdS, PbS, CuS, $Fe_{(1-x)}S$, Bi_2S_3	studies on rapid synthesis of various metal sulfides	[93]
	copper nitrate + indium nitrate	metal sources and sulfur source solution in ethylene glycol at heated	$CuInS_2$	solar cells	[94]
	cobalt dichloride	metal source, sulfur source, citric acid and sodium chloride are dissolved in deionized water and stirred	CoS	studies on incorporating nanoparticles in a matrix for enhancement of electrochemical properties	[95]
	cadmium sulfate	aqueous solutions of metal and sulfur source stirred for 1h with ammonium hydroxide to adjust pH	CdS	studies on synthesis and dielectric properties	[96]
	cadmium chloride	chemical bath deposition of aqueous solutions of metal source and sulfur source	CdS	studies on self-organization	[97]
	ruthenium chloride	aqueous solution of metal source and sulfur source were mixed and subjected to ultrasound irradiation	RuS_2	electrode material for supercapacitors	[98]
Thiourea[*]	copper acetate + indium acetate	metal sources, sulfur source and octadecylamine were dissolved in absolute ethanol and autoclaved at 200°C for 16h	$CuInS_2$	studies on synthesis and mechanism of formation	[99]
	copper acetate	metal source and sulfur source aqueous solution ultrasonicated and pH adjusted with sodium hydroxide	Cu_xS	solar cells	[100]
	lead acetate	methanol solutions of metal source and sulfur source were treated in variations of chemical bath deposition	PdS	studies on property variation with difference in capping	[101]
	cadmium acetate	aqueous solutions of metal source and sulfur source mixed using diffusion through eggshell membrane	CdS	studies on controlling size of produced nanoparticles	[102]
	lead nitrate	aqueous solution of metal source and sulfur source were strongly stirred for 24h and triethylamine used to prevent agglomeration	PbS	studies on optical properties with capping	[103]
	zinc nitrate	sulfur source and metal source dissolved in deionized water and autoclaved at 170°C for 2h	ZnS	studies on electrochemical capacitor application	[104]
	cadmium acetate	aqueous solutions of metal source and sulfur source mixed using diffusion through eggshell membrane	CdS	studies on optical properties	[105]
	copper nitrate	sulfur source added to metal source solution and treated with ultrasound irradiation	CuS	studies on synthesis and electrochemical properties	[106]

Thiourea[*]	cadmium nitrate, bismuth nitrate, indium nitrate, zinc nitrate	metal source and sulfur source coordinated product pressed into pellets and combusted	$NiS + NiS_2$, $CoS_2 + CoS_{1.097}$, Fe_7S_8, $Cu_{1.8}S$, α-ZnS	studies on synthesis by combustion in an inert environment	107
Thioacetamide[*]	cadmium chloride	aqueous sulfur source added to metal source and poly-vinylpyrrolidone solution and sonicated	CdS	studies on capping using sonochemical synthesis	108
	cuprous chloride	aqueous sulfur source solution added to aqueous metal source solution	CuS	studies on bioactive nanoparticle for cancer cell	109
	cupric nitrate	aqueous solutions of metal source and sulfur source mixed with surfactant and oil	CuS	studies on producing metal sulfide nanoparticle within liquid crystal template	110
	bismuth nitrate	sulfur source solution in ethanol added to metal source solution with diphenylthiocarbazone and tetrachlorocarbon	Bi_2S_3	studies on preparation of ion-selective electrode	111
	zinc acetate	sulfur source and metal source separately milled for 15 min and then milled together and heated	ZnS	studies on low-temperature synthesis	112
	copper acetate	sulfur source added to aqueous source solution with capping agent	CuS	studies on absorption of dye	113
	nickel acetate	products of metal source and 2-hydroxy acetophenone solution in ethanol dissolved in ethylene glycol and sulfur source solution added and treated with microwave irradiation	NiS	studies on variation of synthesis conditions	114
	nickel acetate	aqueous solution of metal source and sulfur source mixed with ammonia solution	NiS	studies on loading nanoparticle on activated carbon for dye removal	115
	zinc acetate	ultrasonication of aqueous solution of metal source, sulfur source and silica microsphere	ZnS	studies on surface synthesis of nanoparticles	116
	zinc acetate + manganese nitrate	aqueous solution of both metal sources, sulfur source solution in ethanol, sodium linoleate and linoleic acid heated to 90°C for 10h	ZnS:Mn	studies on photoluminescence properties	117
	zinc acetate	metal source and sulfur source milled separately and then milled together§	ZnS	studies on synthesis technique and properties	118
	copper acetate, nickel acetate	metal source, sulfur source and a complexing agent were treated with ultrasound irradiation	CuS, NiS	studies on synthesis and possible formation mechanism	119
	copper acetate	aqueous sulfur source solution and aqueous metal source solution kept at 80°C for 24h	CuS	studies on the effect of surfactants	120
	cadmium acetate + zinc acetate	metal sources, sulfur source and ethanol stirred at 50°C for 4h	$Zn_xCd_{1-x}S$	studies on photocatalysis	121
	copper chloride	aqueous solution of sulfur source added to aqueous solution of metal	CuS	studies on photothermal therapy	122

Thioacetamide[*]		source and thioglycolic acid pH adjusted with sodium hydroxide			
	copper chloride	sulfur source and metal source added to ethylene glycol solution and treated with microwave irradiation	CuS	studies on synthesis and properties	123
Sulfur Powder[*]	copper chloride	sulfur source solution in oleylamine added to metal source solution with oleylamine, oleic acid and octadecene mixed at high temperatures	CuS	cathode material for Mg-ion battery	124
	cadmium chloride	sulfur source, metal source and sodium borohydride solution in tetrahydrofuran stirred for 3h	CdS	studies on optical and electrical properties	125
	copper acetylacetonate, selenium powder, tellurium powder	metal source, sulfur source, 1-dodecanethiol and oleic acid heat treated	$Cu_{2-x}S$, $Cu_{2-x}Se_yS_{1-y}$, and $Cu_{2-x}Te_yS_{1-y}$	studies on synthesis methods	126
	zinc stearate	sulfur source added to metal source, tetracosane and octadecene solution at high temperatures	ZnS	studies on effect of dopant on electrical properties	127
	nickel nitrate	heated solution of oleylamine and sulfur source added to metal source and oleylamine solution with variations in ratio of sulfur and metal source	NiS, NiS_2, Ni_3S_4, Ni_7S_6	study on single synthesis techniques for variation in phases obtained	128
	zinc acetate + copper chloride + tin chloride	sulfur source in oleylamine added to heated metal sources solution in oleylamine	Cu_2ZnSnS_4	studies on synthesis and electrical properties	129
	zinc chloride	sulfur source solution in capping agent added to metal source dissolved in capping agent	ZnS	studies on properties of nanoparticles with capping	130
	nickel chloride, copper acetylacetonate	sulfur source in solution added to metal source solution and capping agent and heated	Ni_3S_4, CuS and $Cu_{1.8}S$	studies on synthesis and structural properties	131
	ferrocene	metal source and sulfur source ground with a pestle and mortar and heated in alumina foil	FeS_2	studies on solvent-free synthesis	132
Sodium Thiosulfate[*]	sodium perrhenate	perchloric acid added to the metal source, sulfur source and ethylene glycol solution	ReS_2	studies on synthesis and characteristics	133
	cadmium sulfate	sulfur source, metal source, isopropyl alcohol and sodium dodecyl sulfate aqueous solution irradiated with gamma rays	CdS	studies on synthesis and properties	134
	copper oxide + copper sulfate + copper chloride	sulfur source, metal sources and distilled water autoclaved at high temperature	CuS	studies on synthesis from multiple sources of metal	135
Dodecanethiol[†]	copper chloride, lead nitrate, manganese chloride	metal source treated with oleate source which is added to the sulfur source, dodecanethiol and oleylamine solution and heated	Cu_2S, PbS, MnS	studies on synthesis technique and reproducibility	136

31

Dodecanethiol[†]	gadolinium acetylacetonate + Europium acetylacetonate	metal sources and sulfur source solution sonicated	EuS:Gd	imaging of cells in vitro	[137]
Ammonium sulfide[†]	lead nitrate	sulfur source solution added to metal source solution in tributylphosphate	PbS	studies on toxicity	[138]
	silver nitrate	aqueous solution of metal source, sulfur source treated in a stopped-flow reactor	Ag_2S	studies on real-time optical properties	[139]
Hydrogen sulfide[#]	zinc nitrate	metal source solution with nitric acid held in a rotating packed bed reactor and exposed to sulfur source	ZnS	studies on new synthesis techniques	[140]
	titanium tetra isopropoxide	sulfur solution bubbled through metal source solution in butylamine	TiS_2	studies on new synthesis techniques	[141]
Zinc diethyldi-thiocarbamate[*]	Zinc diethyldithiocarbamate	precursor dissolved in octylamine and toluene and heated	ZnS	studies on synthesis from single precursor and mechanism	[142]
	zinc diethyldithiocarbamate	precursor dissolved in toluene and atomized in a furnace	ZnS	studies on synthesis in vapor phase	[143]
Thioacetic acid[†]	copper carbonate	sulfur source solution in acetic/propionic acid added to metal source solution in acetic/propionic acid	CuS	studies on synthesis, electrical and photoluminescence properties	[144]
Tetrahydrothio-phene[†]	zinc 2-ethylhexanoate + manganese naphthenate	metal sources and sulfur source solution in tetrahydrothiophene and treated in a flame spray pyrolysis set-up	ZnS:Mn	studies on large scale production	[145]
Thiosemicarbazide[*]	zinc acetate	metal source, sulfur source, hexamethyle- netetramine and sodium hydroxide autoclaved	ZnS	studies on synthesis and optical properties	[146]
Sodium diethyldi-thiocarbamate[*]	copper chloride	sulfur source, metal source and oleylamine solution heated	CuS	studies on coated nanoparticles for cancer therapy	[147]

^ Adapted with permission.[148]

As seen in Table 1, many metal sulfides have been created and mostly through liquid phase synthesis techniques. In combination with sodium sulfide the most common class of metal sources used are those of nitrates and chlorides. Zinc and cadmium are by far the most utilized metal ions. The preference for zinc, cadmium and copper as the metal ion is seen in other sulfur sources such as thiourea, thioacetamide and sulfur powder. This is likely due to the corresponding sulfides finding application in areas such as photocatalysts and battery electrodes materials. A preference for nitrate and chloride salts is also seen with thiourea. Other

metal classes used with thiourea are sulfates and acetates. Acetate salts are most commonly used with thioacetamide. A few studies have used single source compounds containing both sulfur and metal ions. Zinc diethyldithiocarbamate has been used as a single source precursor to synthesize zinc sulfide nanoparticles. In both documented studies where it has been employed, it was mixed with a solvent and heat treated.

2.3 Ultraviolet-visible spectrophotometric analysis of solutions

UV-Vis spectrophotometry performs absorbance/transmittance and reflectance spectroscopy on solid or liquid samples. Here, the focus is on only liquid samples. This is done by the irradiation of light in the ultraviolet-visible spectral region through the sample. When certain samples are irradiated with light, the electrons within the sample absorb photons and undergo transitions from a lower to higher energy molecular orbital. This happens when the energy of the photon matches the difference in energy required to make the transition.

The spectrophotometer is set-up to have two light sources, one to cover the ultraviolet spectral region and one for visible light. This is done with deuterium and tungsten lamps respectively. The light is then passed through a monochromator to separate the different wavelengths. This results in the ability to compute intensity at each wavelength. This light is then split and passed through a reference holder and a sample holder simultaneously and proceeds to be collected by a detector. The output is obtained as intensity versus wavelength.

In a UV-Vis spectrophotometer, the intensity of the incident light is compared to the intensity of the light after passing through the sample. This comparison is done as Beer-Lambert law states that in a uniform solution, the absorptivity of the sample is directly correlated to the

optical path length (Equation 1). This allows for determination of concentration of species present in the sample.

$$A = \varepsilon c l \quad ...(1)$$

Where absorbance (A) is dependent on the molar absorption coefficient (ε), molar concentration (c) and optical path length (l). The molar absorption coefficient is a sample dependent property. The optical path length is depicted in Figure 9 along with the set-up of a UV-Vis Spectrophotometer. Absorbance of the sample can be equated to the light transmitted from the reference (I_0) and the sample (I) as follows:

$$A = log_{10}\frac{I_0}{I} ...(2)$$

Absorbance should be considered only in ranges from 0-1. Absorbance value of 0 at any wavelength implies that the intensities of the reference and sample beams are the same, showing that absorption of light has failed to take place. Absorbance of a value 1 has the implication that 90% of the light at a particular wavelength has been absorbed and only 10% of incident light has reached the detector. For absorbance value 1, theoretically no transmitted light has reached the detector. From Equation (1), the reason for a high absorbance value is related to concentration of the sample. Hence, dilution of samples before being studied assists in keeping intensity between 0-1. This can also be caused in coloured samples. The solution to stay within acceptable absorbance values remains the same to dilute the sample.
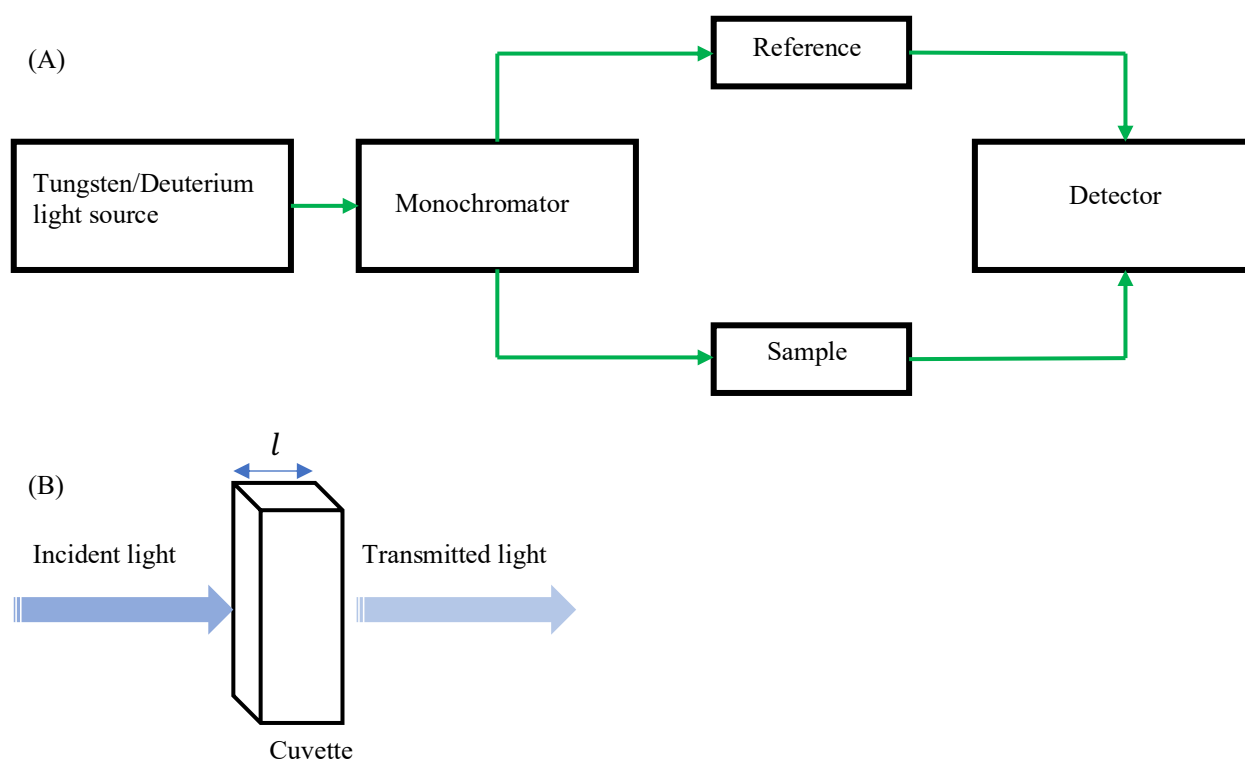
Figure 9. (A) A simplified set-up of a UV-Vis Spectrophotometer. (B) Using Beer-Lambert law, depicted here is the optical path length l, which is taken as the length of the cuvette used to hold liquid samples.

Using UV-Vis spectrophotometry, it is possible to find unknown concentrations of sample solutions. Here, a known and precise concentration solution is run on the instrument and a prominent wavelength is chosen. The absorbance at this wavelength is noted for the particular concentration. Repeating this with multiple known concentrations, absorbance versus concentration profile can be plotted and used as a correlation curve to determine unknown concentrations. As is known from Beer Lambert law that absorbance is proportional to concentration and hence the resulting graph will be linear. If working beyond the scope of Beer Lambert law, the resulting graph is likely to be a curve.

2.3 Production of nanoparticles

To test if precursor-solution combinations created could result in metal sulfide nanoparticles on combustion, a high-throughput single droplet combustion set-up was utilized. This set-up is depicted in Figure 10. To enable combustion of droplets of a defined diameter, a piezoelectric drop-on-demand (DoD) droplet generator is utilized. The benefit of using a piezoelectric DoD droplet generator is that the droplet size and the number droplets generated per minute can be controlled via electrical inputs. It has also shown to be able to produce monodispersed stable droplets for longer time periods.[149] This is important as to be able to collect sufficient nanomaterial after the combustion process. The piezoelectric droplet generator is made using a titanium tube encapsulated by a piezoelectric actuator. One end of the titanium tube is connected to the precursor-solution reservoir. The actuator moves the tube in the radial direction with a displacement of less than 100 nm. The electrodes in contact with the piezoelectric element are controlled via external circuitry.

The piezoelectric droplet generator opens into a quartz cuvette of dimensions 10 x 10 x 45 mm. High voltage electrodes enter on opposite sides of the cuvette, are used to ignite the generated droplets. At the bottom of the combustion zone within the cuvette, a retractable arm that can hold a single TEM grid is used to collect nanoparticles resulting from the combustion of the droplet directly onto the TEM grid. Within the cuvette, gas flow is controlled by means of mass flow controllers.

The TEM grid is a thin foil mesh which can be made from various metals such as copper, titanium, gold, tungsten etc. Here, copper grids are chosen as they are conductive and inexpensive. A copper disc with a mesh and coated with one side flash coated with carbon is

preferred as nanoparticles are to be collected. While the holes on the disc allow for electrons to pass through, the thin carbon coating prevents particles from falling through the grid. Particles are directly collected on TEM grids as TEM allows for scanning imaging, spectroscopy as well as diffraction of specimens. The modes available usually depend on the instrument used.
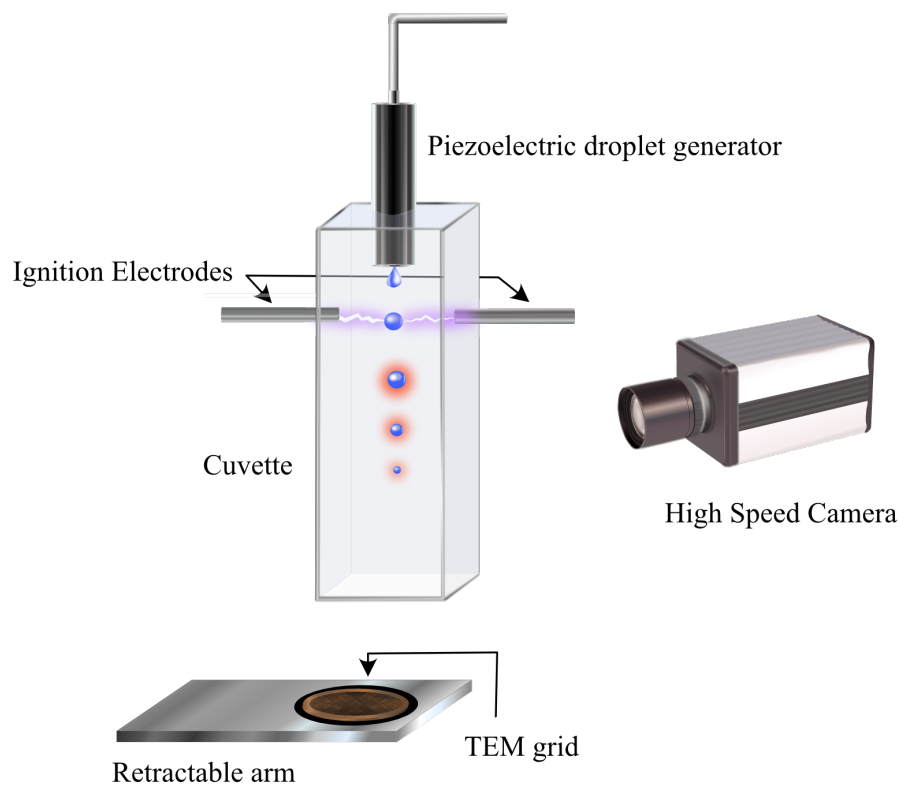

Figure 10. Single droplet high-throughput combustion set-up is shown here. A piezoelectric DoD droplet generator opens into a quartz cuvette. Ignition electrodes are placed inside the cuvette from opposite ends. The ignition electrodes and combined electronics are used to ignite the droplets generated. The product of the combustion is collected on a TEM copper grid placed on a retractable arm on the opposite opening of the cuvette.

2.4 Methodology to analyze produced particles

2.4.1 Transmission Electron Microscopy

Transmission electron microscopy or TEM is a technique to analyze specimens that are <100nm in size. Here, the Titan 80-300 ST microscope (FEI^{TM}) is used. One of the most beneficial features is that both diffraction and image of the same area of interest can be obtained. TEM also pushes to much higher resolution in comparison to light microscopy. Resolving power of a microscope can be defined as the shortest distance between two points that can be clearly distinguished. The need for electron microscopy to looks at nanoparticles can be explained using the Abbe diffraction limit where the minimum resolvable distance between two points (d) is given as:

$$d = \lambda/2n\ sin\theta \quad \dots (3)$$

Where λ is the wavelength of illumination, n is the refractive index of the medium and θ is the aperture angle. As seen, with a direct proportionality the smaller the wavelength of illumination, the smaller the resolvable distance can be. Using an accelerated electron beam with 100 – 400 kV results in wavelengths of 0.0037 – 0.0016 nm compared to visible light where the lowest possible wavelength is 400nm.[150] To understand this, we start with the de Broglie relation of wave-particle duality which is as shows the dependence of the momentum of a particle with its wavelength:

$$\lambda = h/p \quad \dots (4)$$

Where h is the Planck's constant. Electron in a TEM attains a kinetic energy eV by the imparting of momentum to electron through a potential drop V. Hence the potential energy of the electron and momentum can be equated as:

$$\frac{m_\circ v^2}{2} = eV \quad \dots (5)$$

$$p = m_\circ v \quad \dots (6)$$

As electrons within a TEM are accelerated at high voltages such that their speed reaches more than 50% the speed of light, relativistic effects must be taken into consideration and the relation between accelerating voltage and wavelength is given by:

$$\lambda = \frac{hc}{\sqrt{eV(2m_\circ c^2 + eV)}} \quad \dots (7)$$

Where, h is the Planck's constant, c is the speed of light, e is the charge of an electron, V is the acceleration voltage and $m_\circ$ is the electron mass.

As a TEM utilizes an accelerated electron beam to analyze samples, all the components that interact with the electron beam are housed inside a vacuum chamber. This helps to reduce unwanted electron-gas collisions to negligible levels and hence increasing the mean free path. This is achieved using a series of multiple vacuum pumps, each operating at different pressure ranges. The electron beam required in a TEM is generated by an electron gun. The electron gun can be a thermionic or a field emission gun.[151] Thermionic guns are heated to achieve electron beams whereas field emission guns utilize high voltages to achieve electron emission. Materials used for generation of electrons are usually single crystal tungsten or lanthanum hexaboride. Field emission guns are capable of greater current densities which results in a better signal-to-noise ratio as compared to a thermionic gun.

The generated electron beam is manipulated using lenses that are made of electromagnetic coils. The condenser lenses are positioned under the electron gun. Below the condenser lenses are the objective and projection lenses. The condenser lenses focus the electron beams on to the specimen, illuminating the area under observation. The specimen in a TEM is placed in between the objective lenses.[152] Here, initial focus and magnification of the specimen takes place. The image is further magnified by intermediate lenses and followed by further magnification and projection onto the phosphorous screen by the projection lenses.

Electrons interact with the specimen in several ways. Selective detection and analysis of the different interactions enables imaging, quantitative and semi-quantitative information gathering. Elastic scattering, where there is a high angle change of direction with negligible change in energy of the electron contributes to the presence of back scattered electrons (BSE). This is usually caused by interaction with the nucleus. BSE production directly varies with the atomic number of elements causing the backscattering. This gives a topographical image where differences in average atomic number can be observed.

Inelastic scattering produces a few different effects. When the electron beam hits the specimen, an electron from the beam can knock out an electron within the specimen forming what is known as secondary electrons. When an electron from the beam knocks out an inner shell electron, an electron from a higher energy shell can fall into the vacancy and the remaining energy is ejected as photons in the visible or near infrared range or can be transferred to an outer shell electron which is then ejected forming an Auger electron.

The region on the specimen the electron beam interacts with is known as the interaction volume. The depth of penetration of the interaction volume depends on the intensity of the electron beam and well as the atomic mass of the sample. In this volume, at the very top of up to 5nm depth is where Auger electrons are primarily ejected from. Detecting and analyzing Auger electrons enables elemental study of surfaces and thin films as the escape depth is a few monolayers due to their low energies. If x-ray photons are formed instead of Auger photons, they are used to qualitatively detect elemental composition. This is more established as a qualitative elemental analysis rather than quantitative. Secondary electrons, which possess energies typically below 50 eV have an escape depth of around 10 nm. Although it is likely that secondary electrons are generated below this depth, they are unable to escape into the vacuum hence making detection impossible. These are primarily used to characterize surface morphology.[153]

The diffraction imaging in TEM is done by focusing on the back focal plane of the objective lens and acts as the image plane for the intermediate lens. This is depicted in Figure 11. The result of this is a dotted pattern for single crystal specimens or ring pattern for polycrystalline specimens made up of differently oriented crystallites. The diffraction pattern generated by a TEM is known as Selected Area Diffraction (SAED) as the diffraction pattern generated is formed from a specific user chosen area. This is enabled by the use of apertures which block out the beam from other areas. For a single crystal sample, the SAED pattern is the two-dimensional projection of its reciprocal lattice and will depend on its orientation with respect to the electron beam.
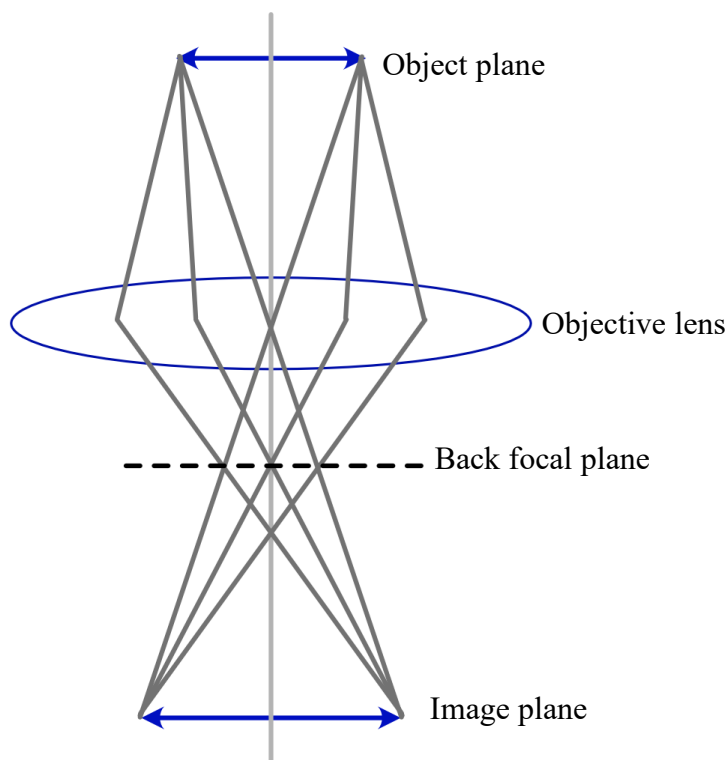
Figure 11. Schematic representation of rays from a finite object. Here, all rays from the object are converged by the lens to the image plane. The back focal plane is where all the parallel rays from the image are focused by the objective lens. Depending on the mode of operation, the intermediate lens uses the back focal plane or the image plane as its object. This is depicted in detail in Figure 13.

The diffraction mode available on the TEM is used to measure the lattice constants. Here, specifically the d-spacing. Diffraction by electron was accidentally discovered by C. Davisson and L. H. Germer in 1927.[154] As accelerated electrons exhibit wave-particle duality and wavelength of electrons is comparable to the interatomic spacing, it is scattered by the atoms within the lattice and an analogy to x-ray diffraction can be made. Consider two lattice planes separated by a distance d as shown in Figure 12. The incident rays are parallel and in-phase and strike the lattice plane at an angle θ. The top beam strikes an atom on the upper layer and scatters whereas the second beam continues to layer below before being scattered by an

atom on the plane below. If the rays are to continue in the same phase, the extra distance covered by the bottom ray must be an integral multiple of the wavelength, resulting in constructive interference at the Bragg angle:

$$AB + BC = n\lambda \quad ...(8)$$

As seen in the figure, the hypotenuse of the right triangle is d and the AB = BC, hence:

$$AB = d\ sin\theta \quad ...(9)$$

$$AB + BC = 2d\ sin\theta \quad ...(10)$$

Combining equation 8 and 10, we arrive at Braggs law of diffraction:

$$n\lambda = 2d\ sin\theta \quad ...(11)$$
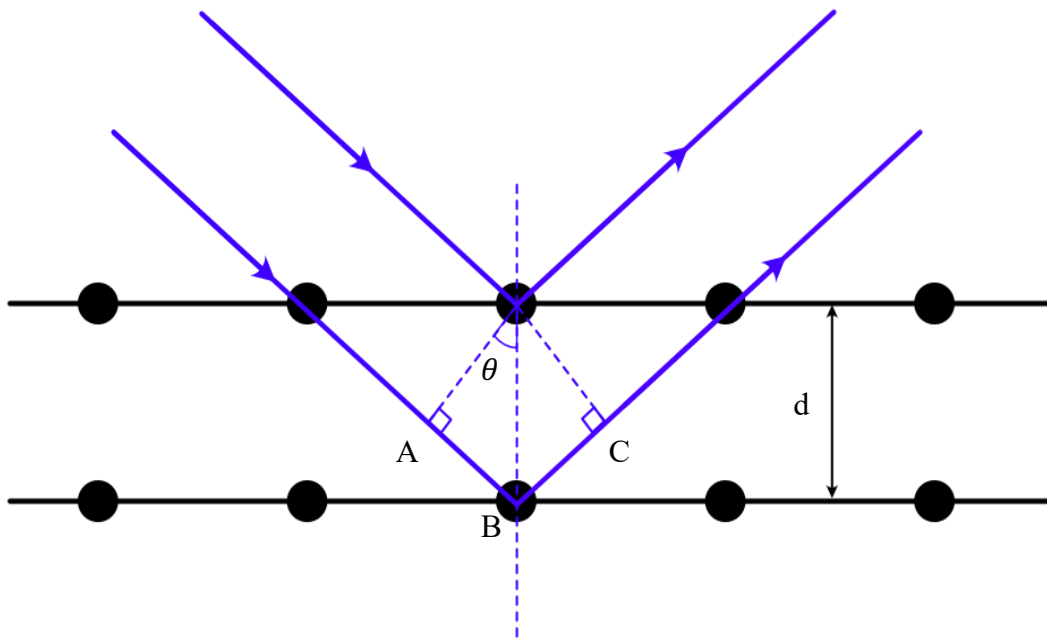
Figure 12. Depicted here are two parallel lattice planes of atoms separated by a distance d. The two incident rays scatter off two different atoms with the lower beam traversing a slightly longer path after undergoing scattering.

The analysis of *d*-spacing is powerful as every mineral compound has its own unique set of *d*-spacing values. Values obtained from electron diffraction can be compared to diffraction patterns obtained from x-ray diffraction which is usually displayed as an x-y graph with x-axis being 2θ and y-axis being intensity. In the x-ray diffraction pattern, the unique *d*-spacing appear as peaks. As peak positions can provide information on cell parameters when crystal structure is known. In certain cases, peaks from certain planes will have an intensity of zero due to symmetry. For different crystal structures the conditions for peaks to occur are also varied.
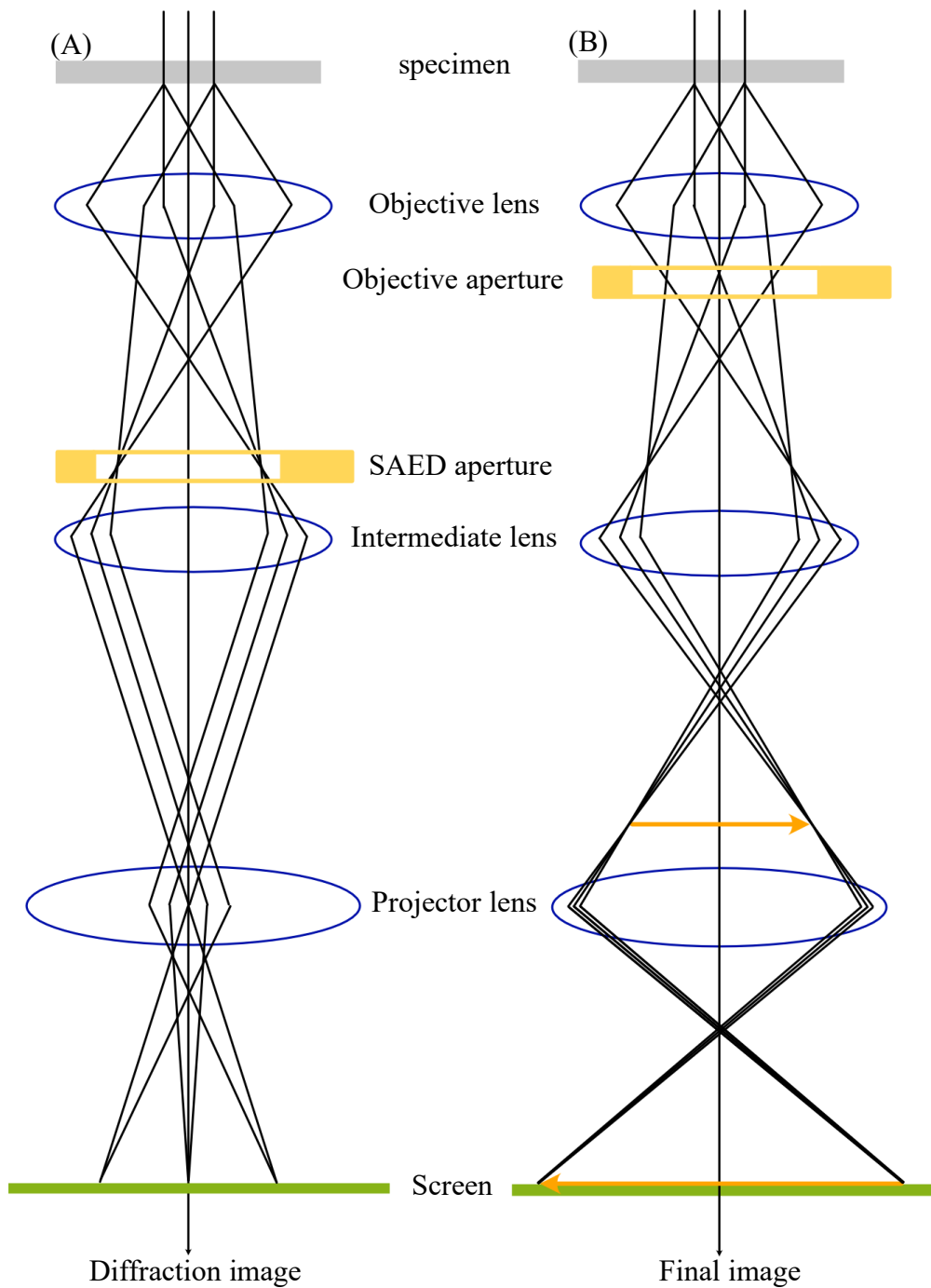
Figure 13. Simplified schematic of the two basic imaging modes in a TEM. (A) Depicts the diffraction imaging mode where the objective aperture is removed and (B) depicts imaging mode where the SAED aperture is removed. The imaging mode can be changed by what the intermediate lens chooses as its object. Redrawn with permission.[155]

2.4.2. Software

As particles are directly collected on a TEM grid below the combustion area, information obtained from TEM is used to characterize the particles. To determine the compound formed, high resolution and SAED images are analyzed for their *d*-spacing. To do this, the processing software Fiji (ImageJ) was used, screenshot of which can be seen in Figure 14. This is an open-source platform (BSD-2 license) and has the capability via open architecture to allow for extension of functionalities to provide custom analysis and processing Java plugins.

Images obtained from TEM for *d*-spacing analysis are .dm3 format which can be opened and processed on Fiji. Once opened, the image is to be checked for correct scaling in comparison to the magnification. As this varies from instrument to instrument, the calibrated values have to be checked individually. This is important as all compositional values of the compound are obtained through the *d*-spacing. Two Java plug-ins - 'Concentric Circles' and 'TEM suite'- that are additionally needed can be downloaded from the ImageJ website. Concentric Circles plugin enables drawing of specified number of concentric circles with individual inner and outer radii. The circles created are a non-destructive overlay and retains the original pixel intensity of the image. TEM suite is a collection of 4 Java plugins for analysis of d-spacing from images taken on a TEM – 'calc dSpace', 'get dSpace', 'pub Montage' and 'get Meta'. A combination of Concentric Circles and TEM Suite are used to obtain d-spacing from concentric rings seen on TEM images.
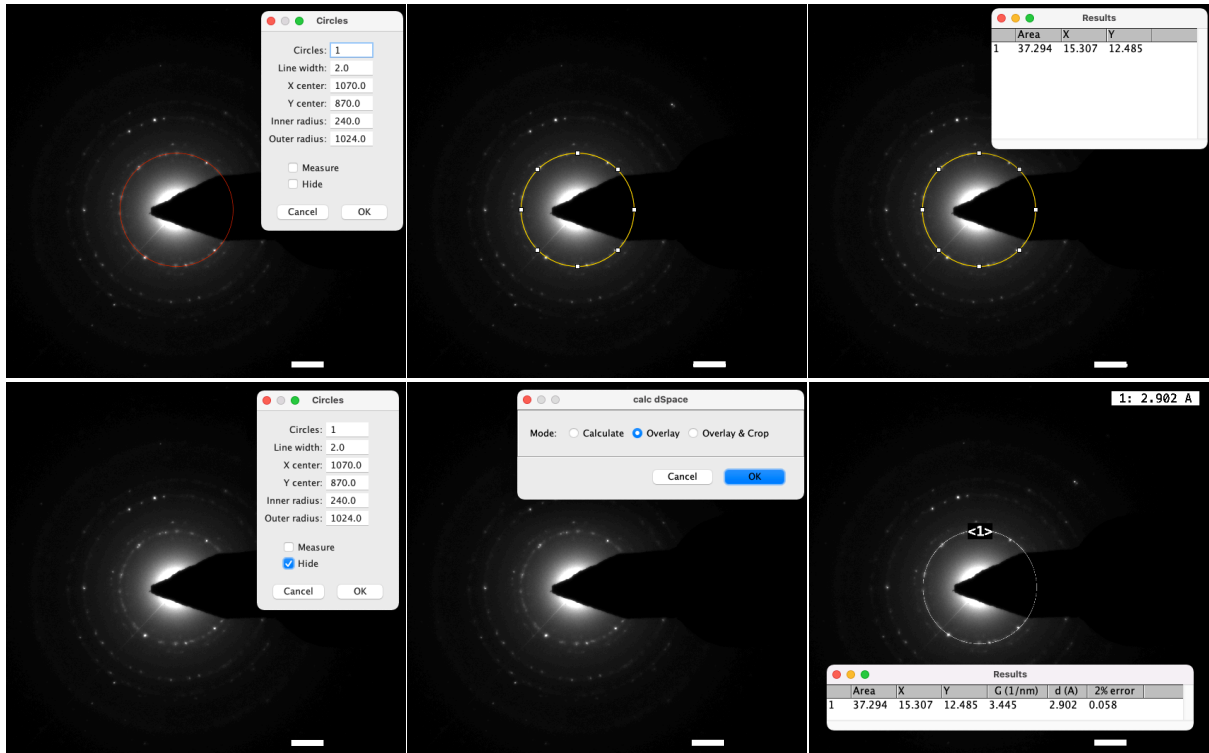
Figure 14. TOP (left to right) 1. Circle created on a *.dm3 SAED image using 'Concentric Circle' plug-in. The x and y centers are specified and inner radius is changed to overlap the ring structure. 2. Oval tool is used to create a circle on top of the red circle 3. After drawing with the oval tool, the circle is measured and the resulting data is shown in a pop-up window as seen in the figure. BOTTOM (left to right) 4. Concentric Circle plug-in is started again and the option 'hide' is selected to remove the red circle from the image. 5. Calc dSpace plug-in from TEM suite is started and 'overlay' is selected from the options. 6. On selecting 'overlay' measurement of the circle from previous steps is used to compute the *d*-spacing which can then be seen in the results window. By repeating the steps, *d*-spacing of all rings present on the image can be obtained. ROI manager can be utilized to save an area selected using the oval tool and used for measurements.

First, to obtain an accurate diameter of the concentric ring diffraction pattern on the SAED image, the Concentric Circles plugin is used. Here, the x-center and y-center are defined based on the bright center spot. Number of concentric circles is set to 1. With this, the innermost ring/spots is overlapped with a circle created by the plugin by adjusting the radius. On this circle, using the oval tool in its circle mode (holding down shift while tracing) another

overlapping circle is created and measured. Once all rings/spots are measured, calc dSpace plugin of the TEM suite is used. This results in an output that shows the scalar component of the G vector in reciprocal space (1/nm), d-spacing and 2% error. For analysis of high-resolution lattice fringes corresponding to the SEAD images, a straight line is drawn through the spots or lines using the straight tool and then analyzed using 'Plot Profile'. Multiple lines are averages to obtain the final d-spacing value. An in-depth look at the analysis along with images is shown in Figure 15.
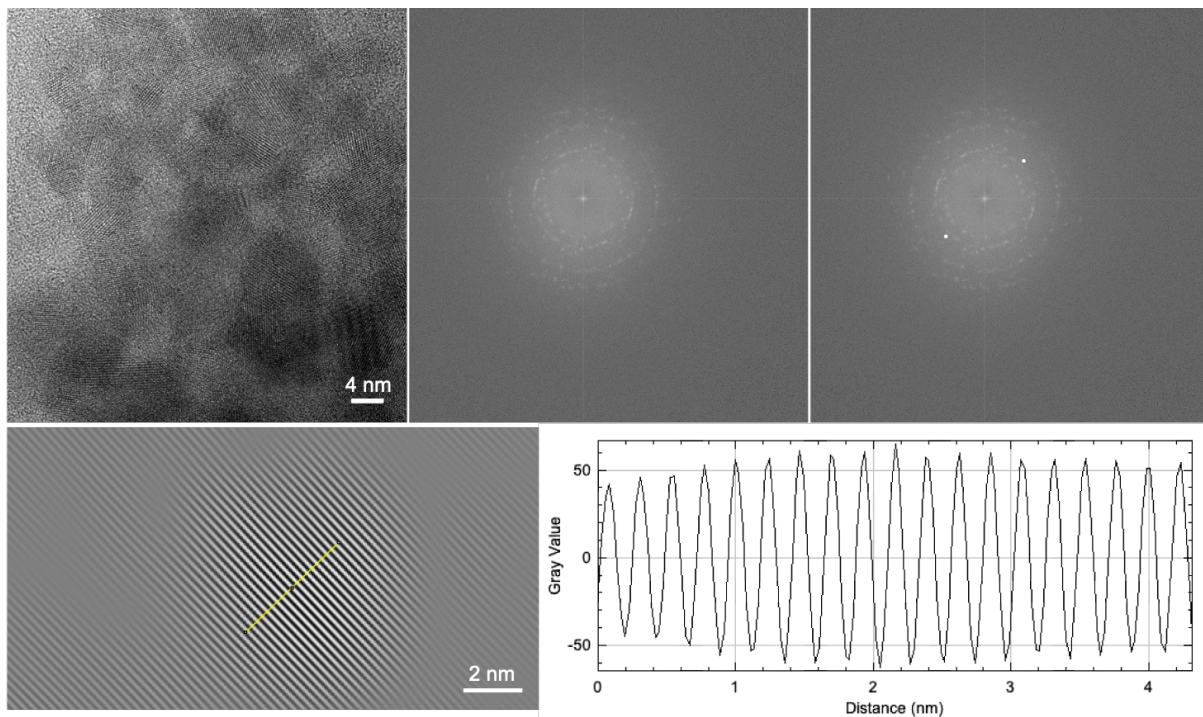
Figure 15. TOP (left to right) 1. A high-resolution *.dm3 image is opened in Fiji 2. Fast Fourier Transform (FFT) of the image is done using the processing option resulting in a diffraction pattern of all particles present in the image. 3. Two opposing diffraction spots are chosen and filled in using the oval tool and the fill option. BOTTOM (left to right) This acts as a mask which on performing inverse FFT results in 4. A clean image of lattice fringes formed by the nanoparticles for the selected diffraction spots. 5. Plot profile is used from the drop-down menu options to obtain the d-spacing value from the maxima.

The analysis of SAED pattern obtained gives values for all d-spacings present in particles in the region under observation. Obtaining these values of d-spacing from samples help identify what was produced by comparing the values to compounds with known *d*-spacing values in the ICSD database. As many compounds can have multiple peak positions that match with the unknown compound, peak intensities are also to be taken into consideration as it is determined by the atomic number and position of atoms within the unit cell.

2.5 Fourier-transform infrared spectrometry (FTIR)

FTIR is used to obtain information on infrared spectrum absorption or emission by the sample under study. When IR radiation interacts with a molecule it can cause vibrations within it. Molecules usually contain different types of bonds with differences in strengths of those bonds and atoms of different masses, each of which possesses its own characteristic energy. If this energy matches that of IR irradiation that is direct onto the sample, it is absorbed. The resulting spectrum acts as a unique molecular fingerprint for that sample. Hence, it finds use in different types of analysis such as identification of unknown samples, number of compounds present in sample. quality of sample etc.

It all starts with an IR light source. The light then passes through an interferometer, where it is split into two beams. To be able to scan through all infrared frequencies simultaneously on a sample, the instrument relies on an interferometer. One of the split beams falls on a stationary mirror while the other onto a motorized moveable mirror. The two beams recombine at the beam splitter and moves to the sample. As the path length of one of the split waves is being changed, the recombined IR light has constantly changing frequencies. A plot of this signal intensity versus time (mirror position) is known as the interferogram. Fourier transformation

is performed on the output signal to convert it from time domain to frequency domain and hence obtaining an intensity versus wavenumber plot which is usually used for analysis. The graphical representation of the set-up is shown in Figure 16.
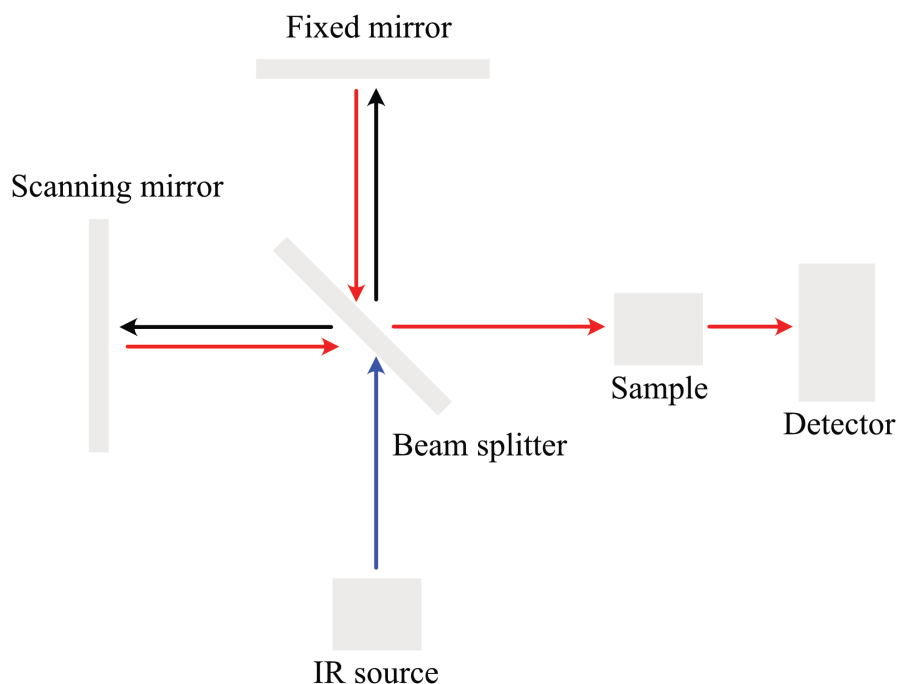
Figure 16. The basic functioning of a Fourier transform infrared (FTIR) spectrometer is shown here. Light from the IR source is split into two at the beam splitter. One of the beams falls on a fixed mirror while the other falls on a motor movable mirror. The two beams then recombine to pass through the sample and onto the detector. The obtained interferogram is converted to a frequency domain using Fourier transformation.

Every molecular functional group and bond show distinctive peaks on absorption of infrared light. These fingerprint peak patterns can be used to identify unknown compounds using database patterns. FTIR analysis can also be used quantitatively. Here for example, it is used to identify concentrations of compounds. For this standard samples with known concentrations are used to create a correlation curve which can then be extrapolated to obtain concentration of unknown compounds.

2.5.1 Determination of components present in solution

In this body of work, FTIR analysis is predominantly used to determine composition of solutions that have been treated either to heat or environmental conditions. The instrument used for this analysis is the 'Agilent Cary 630 FTIR' spectrometer. The possibility to use minute quantity of sample for analysis on this instrument is extremely handy.

As solutions of quantities 10 mL and less are studied, on treatments such as room temperature evaporation much smaller amounts of solution is left behind. This can be collected using syringes which are then used to deposit a few drops of the sample on the spectrometer. For solutions that separate into immiscible layers, a syringe is used to get sufficient amounts of the bottom layer first followed by using another syringe for the top layer. For solutions containing uncommon compounds, analyzing individual peaks in the generated spectrum can prove to be challenging. Comparison can be made to spectra of individual compounds to determine what components could likely be contributing to the peaks.

After determining components contained in the sample, it is possible to extrapolate the concentration of a select component. For this, a spectrum of known and differing concentrations of the component in similar a solution is needed. The information from the spectra of the known concentration of solutions are then used to create a correlation curve which is used to extrapolate for the unknown concentration in the sample. This is a basic plotting technique to produce a standard calibration curve. Using the slope and intercept, a linear function is solved to obtain the unknown concentrations in solution.

2.6 Mass spectrometric analysis

In mass spectrometric studies, samples are ionized to obtain their mass-to-charge (m/z) ratios. This is useful to determine molecular weight of components through which unknown compounds can be identified. The principle behind this is the difference in deflection of molecules of different mass accelerated at the same speed. As the deflection depends only on mass, through detection electronics a precise determination of molecular masses present is possible.

A mass spectrometer, schematic depicted in Figure 17, has three significant phases to it, which starts with ionization. Although there are multiple ways in which samples can be ionized, the instrument used utilizes an electron impact ionization to do so. With electron impact ionization the sample is in the vapour phase and is ionized and sometimes fragmented due to fast moving electrons. The accelerated ions then pass through a mass analyzer. It is here that the charged ions are separated according to their mass-to-charge ratio (m/z). This is done using a magnetic field. The effect of an electromagnetic field on a charged ion is defined as Lorentz force:

$$F = Q(E + v \times B) \ \dots (12)$$

Where, F is the force applied on the charged ion, Q is the ion charge, E is the electric field, v is the ion velocity and B is the magnetic field. Considering Newton's second law of motion, the above equation can be rewritten as:

$$(m/Q)a = (E + v \times B) \ \dots (13)$$

This equation governs the movement of charged ions when subjected to an electromagnetic field. As seen in the equation, this movement is influenced by the term m/Q. This dependency is exploited in mass spectrometers and represented as a dimensionless value m/z where:

$$z = Q/e \quad ... (14)$$

Defining z as the number of elementary charges (e) present on the ion. In the instrumentation used here, a quadrupole mass analyzer is used. As the name suggests, it is made of four metal rods which are placed in a parallel configuration and a voltage is applied between two pairs of the electrodes. This is used so that only ions of a certain m/z value reach the detector. This allows for a rapid sweep of predefined range of m/z values.
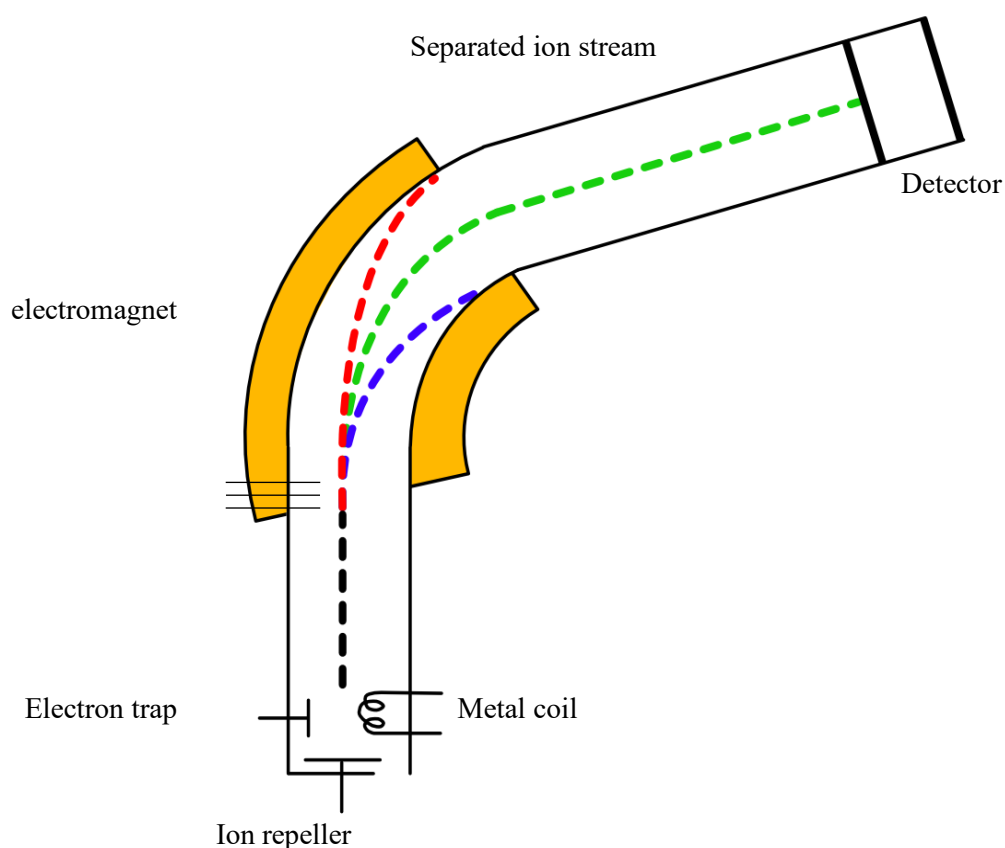
Figure 17. The general working of a mass spectrometer is shown here. The vaporized sample enters the chamber which is constantly being pumped out by a vacuum pump. This is to avoid unwanted electron collision with gas molecules. The sample is ionized and a stream of mixed ions, represented by black dash line, is formed, and accelerated. On reaching the

electromagnetic field, ions of different m/z values get deflected by varying amounts. Ions with lighter mass are more deflected than ions with a higher mass, which is represented here by blue and red dash lines respectively.

The outcome of putting a sample through a mass spectrometer is a stick diagram of relative intensity versus different values of m/z. The relative intensity is obtained by the number of ions being detected for each m/z value, hence providing an insight into relative abundance on the ions. The stick diagram of fragmentation of an element shows the isotopes of that element whereas for a compound it represents fragmented parts of a molecule of that compound. The tallest peak in the stick diagram, also known as the base peak, is usually represented by an intensity of 100 implying that it is the most abundant fragment. The intensities of all other fragments are measured relative to it.

2.6.1 Determination of fragment composition

To study chemical components or precursor-solvent solutions fragmentation on treatment with high temperature, samples are first placed in a suitable crucible. Here, a Netzsch STA 449 F1 Jupiter TGA coupled to QMS 403 Aëolos Quadro mass spectrometer is used. Crucibles that are loaded into the thermogravimetry cavity of the STA 449 Jupiter can be purchased in many different materials and forms. In all TG-MS studies mentioned in this work, aluminium oxide crucibles with punctured lid have been used unless otherwise mentioned.

The STA 449 measurement software provided by Netzsch is used as the acquisition software and used to control all settings including the heating rate, gas flow and temperature cycles. As liquids are studied, only heating cycles are of importance here. Throughout all experiments a

heating rate of 10K/min was employed. From the data generated, which is stored in a '.ngb-ss3' file, the software 'NETZSCH Proteus® Thermal Analysis' is used for further analysis.

In the Proteus® software, under the drop-down menu of 'Mass Spectra' an option to show/hide QMID curves is available. Using this feature, individual atomic mass units (amu) can be selected. However, since we can expect the unexpected due to limited or no prior studies of high temperature fragmentation of compounds and combination of compounds used here, for the initial analysis all amu that correspond to the individual component and lower are selected. For example, is only tetrahydrothiophene (THT) is being studied, all amu values from 88 and below are selected. In areas where peaks are present, values of amu that flat and show no sign of presence in the run can be deselected. With this, values of amu for all fragments formed from the breakdown of components present in the liquid are obtained.

Matching the amu values to most likely contributing chemical species is the more difficult part. Within Proteus®, when double clicking on a peak in the scan bar graph inside the 'Aeolos' window opens the linked 'NIST MS Search 2.4' library with matching chemical structure contributing to peaks. However, the database is limited and care must be taken that species displayed can be formed with elements present in the sample. For a more extensive list NIST Chemistry WebBook, SRD 69 can be used. Here, searching by molecular weight all possible corresponding chemical structures can be obtained. From this, all species that can be formed by elements present in solution of that particular molecular weight can be obtained. This is usually one or two compounds and further insight into which of them is the most stable and more likely to be formed must be deduced. It must also be considered that organic molecules of same elemental composition can have different structures. In this manner, all peaks of differing amu values can be assigned to structures formed on dissociation.

As intensities of generated fragments are relative to each other, the intensities of peaks can reasonably be used to assess as to the abundance of different fragments. This is useful to also understand what gaseous species could be forming under given conditions on heat treatment of the sample. Combined with knowledge of elemental composition of fragments formed and their relative abundance an indication of how the breakdown proceeds can be obtained.

Chapter 3.
Results & Discussion

3.1 Precursor-solvent solutions

As the synthesis process described here aims to enable single-step gas-phase synthesis of metal sulfides with well controlled compositions, commonly used inorganic sulfur salts such as sodium sulfide are excluded as it increases the probability of inclusion of unwanted elements such as Na in the final product. In addition to sodium sulfide, other sodium and metal containing sulfur sources are disregarded as a choice for a sulfur source.

One of the sources of sulfur that provides only sulfur – sulfur powder was tested with various solvents for its solubility. In 5 mL of xylene, sulfur powder was added to make 1M solution. This was sonicated to assist in dissolution. However, the result was a colloidal looking solution where particles of sulfur failed to dissolve. Reducing the concentration of sulfur 10X and with

sonication sulfur powder dissolved in xylene. As metal concentration in solution need be at least 0.25M, sulfur powder in xylene with low dissolution properties is unsuitable.

The next solvent that was tested with sulfur powder was toluene. Here, even at 0.15M dissolution was only partial. Nevertheless, with overnight stirring a clear solution was obtained. Toluene eats away at parafilm and hence and instead of a glass jar, a closed bottle was used. When concentrations were increased by 5X it resulted in the appearance of chalky white precipitate. Ethanol, water, and propanol all resulted in poor dissolution as well. With the inability to provide varying and higher concentrations of sulfur to a metal source, sulfur powder is seen as an unappealing sulfur source.

Another sulfur source that was found is 2,2 thiodiethanethiol (TDT). With 3 sulfur atoms per molecule, it is the sulfur compound with highest S per molecule that was found to be commercially available and containing only S, C and H. It is in liquid form at room temperature, non-toxic and is odor free. It is soluble in most organic solvents including xylene. In dissolution studies it failed to dissolve in ethanol. Although it appears to be an ideal source of sulfur with capabilities to provide up to 1:60 ratio of M:S, the steep price of the compound makes it highly unattractive for future bulk usage.

As the starting metal-precursor combination must be liquid to feed into the drop generator, using a liquid form of sulfur source has multiple benefits. If a solid source of sulfur is used, both sulfur and metal source must be dissolved in a solvent. As there is an extent to solubility in a solvent, this can limit the concentration of sulfur being used. In the gas-phase synthesis it is important to consider this aspect as the sulfur is likely competing with oxygen for the metal ions making it beneficial to be able to provide more sulfur molecules per molecule of metal.

Out of the three sulfur sources that contain only S and potentially C and H from Table 1 are sulfur powder, dodecanethiol and THT. From these, only dodecanethiol and THT are liquid at room temperature. Although both dodecanethiol and THT can be procured in liquid form, THT is the more ideal sulfur source. This is due to dodecanethiol being an oily liquid that has a much higher boiling and flash point as compared to THT. This is likely due to its structure of a 10-carbon chain.

The next benefit of THT is that it is highly volatile and combustible which can assist in promoting disruptive and explosive combustion. As THT is widely used as a natural gas odorant, it is also easily available and considerably cheap, making it an ideal candidate for future large-scale synthesis. THT was dissolved in a range of solvents. Solvents are considered if able to dilute THT to desired concentration. What is interesting to be noted is that it is soluble by itself to a large extent in most organic solvents. Then again, THT is insoluble in water. This is beneficial as it has the potential to be used with a wide range of metal precursors.

To formulate precursor-solvent combinations for testing in the gas phase using single droplet combustion, multiple criteria were needed to be fulfilled. The precursor-solvent combinations needed to be highly soluble without any suspensions. This is done to avoid clogging of pipes and equipment that have small diameters. The chemical components used were selected so that they are economically viable for large scale production in the future. Care was taken to make sure the precursors were also commercially easily available and low in toxicity as solutions are also handled in multiple environments to be studied. Use of highly toxic compounds such as those that need to be handled under inert atmosphere to prevent exposure or uncontrolled reaction are avoided for personal safety reasons. Concentrations of 0.25M with a M:S ratio of

1:20 are used throughout. In this manner, highly combustible and stable precursor-solvent combinations were created.

One of the first metal sources picked was ferrocene. The sandwich structure combined with the presence of only carbon, hydrogen and iron made it an excellent option to avoid contaminating end products with other elements. Hence, it acts as a clean source of iron. The downside of testing with iron is that the x-ray powder diffraction of iron oxides and iron sulfides have a lot of overlap. To counter this, copper, with a pronounced difference in powder diffraction pattern between oxides and sulfides was also studied. Mesityl copper was chosen as the precursor for copper due to the absence of elements other than C, H and Cu. As these single droplet combustion studies are being done for the first time to produce metal sulfides, these two are excellent metal sources to test the production and characterization of metal sulfides as it restricts the number of compounds that can potentially form. However, as both the metalorganic salts, Ferrocene and Mesityl copper, are uncommon, zinc nitrate was also studied in parallel as it is a widely used and easily available common salt. Nitrate salts for other metals can be easily obtained and are cheaper hence a better testing subject for multiple metals. Hence, after testing initial characterization to confirm formation of metal sulfides, focus was placed on studying in-depth the use of metal nitrate salt as the metal source. Nitrate metal salts used throughout were hydrated salts unless otherwise specified.

Other metal sources, including some single sources which contain metal and sulfur in the same molecule were studied for dissolution in solvents and sulfur source to study potential future paths to create metal sulfide nanoparticles. Some of these are shown in Table 3.

Table 3. Metal source, sulfur source and solvent dissolution studies. A mixture of metal sources as well as single source compounds that were tested are shown here. Acetylacetonate salts are abbreviated as (acac) and diethyldithiocarbamate as (ddtc). All nitrate salt mentioned are hydrated versions of the respective salts.

Metal Source	Sulfur Source	Solvent	Dissolution
Iron oxide	TDT	Ethanol	No
Iron oxide	-	Xylene	No
Iron oxide	-	Ethanol	Yes
Iron oxide	-	Toluene	No
Zinc oxide	TDT	Xylene	No
Zinc oxide	-	ethanol	No
Zinc oxide	TDT	Ethanol	No
Zinc oxide	-	Toluene	No
Zinc oxide	-	Xylene	No
Cerium oxide	THT	-	No
Cerium oxide	Toluene	-	No
Copper(acac)	THT	ethanol	No
Copper(acac)	TDT	toluene	No
Copper(acac)	THT	xylene	No
Copper(acac)	THT	EHA	No[#]
Copper(acac)	THT	DMSO	Yes
Copper(acac)	TDT	xylene	No
Copper(acac)	TDT	Xylene + DMSO	No
Copper(acac)	THT	EHA+ xylene	No
Copper(acac)	-	Acetone + xylene	No
Lithium(acac)	-	Xylene	No
Lithium(acac)	THT	EHA	Yes
Aluminum(acac)	THT	EHA	Yes
Indium(acac)	THT	xylene	Yes[§]
Zinc (ddtc)	-	toluene	No
Zinc (ddtc)	-	Xylene + DMSO	No
Zinc (ddtc)	-	Acetone	No
Zinc (ddtc)	-	EHA + xylene	No
Zinc (ddtc)	-	Ethanol + xylene	No

Zinc (ddtc)	-	EHA + ethanol	No
Zinc (ddtc)	-	Ethanol + H2O	No
Zinc (ddtc)	-	Xylene + toluene	Yes
Trimethyl(phenyl)tin	-	xylene	Yes
Zinc nitrate	TDT	xylene	No
Zinc nitrate	THT	Ethanol	Yes
Zinc nitrate	TDT	DMSO	Yes*
Gallium nitrate	THT	Ethanol	Yes
Lithium nitrate	THT	Ethanol	Yes
Iron nitrate	THT	Ethanol	Yes
Copper nitrate	THT	Ethanol	Yes
Ferrocene	TDT	Xylene	Yes
Ferrocene	THT	Xylene	Yes
Mesityl copper	THT	EHA	Yes

*Depends on the order in which solutions are mixed. DMSO mixed with TDT to which zinc nitrate is added forms a well dissolved solution. However, when zinc nitrate is initially mixed with DMSO and then sulfur source added to it forms separated layers.

§additional xylene needed for complete dissolution

#partial dissolution

From the table, it can be observed that although there are classes of metal compounds that seem to be ideal metal sources, consistent dissolution with a sulfur source is challenging. From the multiple classes of metals that were tested, consistent dissolution to study the formation of metal sulfides was seen in metal nitrate salts. As seen in Table 2, a large percentage of liquid phase synthesis also utilize metal nitrates as the metal source. Nitrate ions form salts with a wide range of elements across the periodic table. This is displayed in Figure 18. The ease of similar dissolution across nitrates of multiple metals also provides a base to study variations in metal while keeping solvent and sulfur constant. Nitrate salts have also previously been used in producing metal oxides through flame combustion synthesis. Although the chemistry is different owing to the need for a sulfur source, it has been shown to successfully work with combustion synthesis.

Figure 18. Elements indicated in yellow have corresponding nitrate salts commercially available through Alfa Aesar as of 2022.

3.2 Nanoparticle composition identification

As high throughput single droplet combustion is a screening method, particles produced are minute in quantity. The particles are captured directly on TEM grids for the same reason. Hence analysis of composition, crystallinity, morphology and size is done primarily using techniques available on a transmission electron microscope. The data obtained are low resolution images to identify particles, high resolution images to analyze lattice spacing and selected area electron diffraction (SAED) images to obtain all d-spacing in the observed area. Electron diffraction data was analyzed on ImageJ.

As mentioned in the previous section, the testing started using a precursor solution of ferrocene. The particles formed from combustion are shown in the low-resolution column labelled LR in

Figure 19. Analysis on the SAED images obtained from the sample was analyzed as mentioned in section 2.4. Analyzed diffraction rings give corresponding d-values of 2.942 Å, 2.475 Å, 2.064 Å and 1.488 Å. Between 2.064 Å and 1.488 Å there are spots observed but a circle drawn through these was avoided as symmetric spots were difficult to locate and trace. This would account for the missing ICSD d-spacing 1.7 Å.
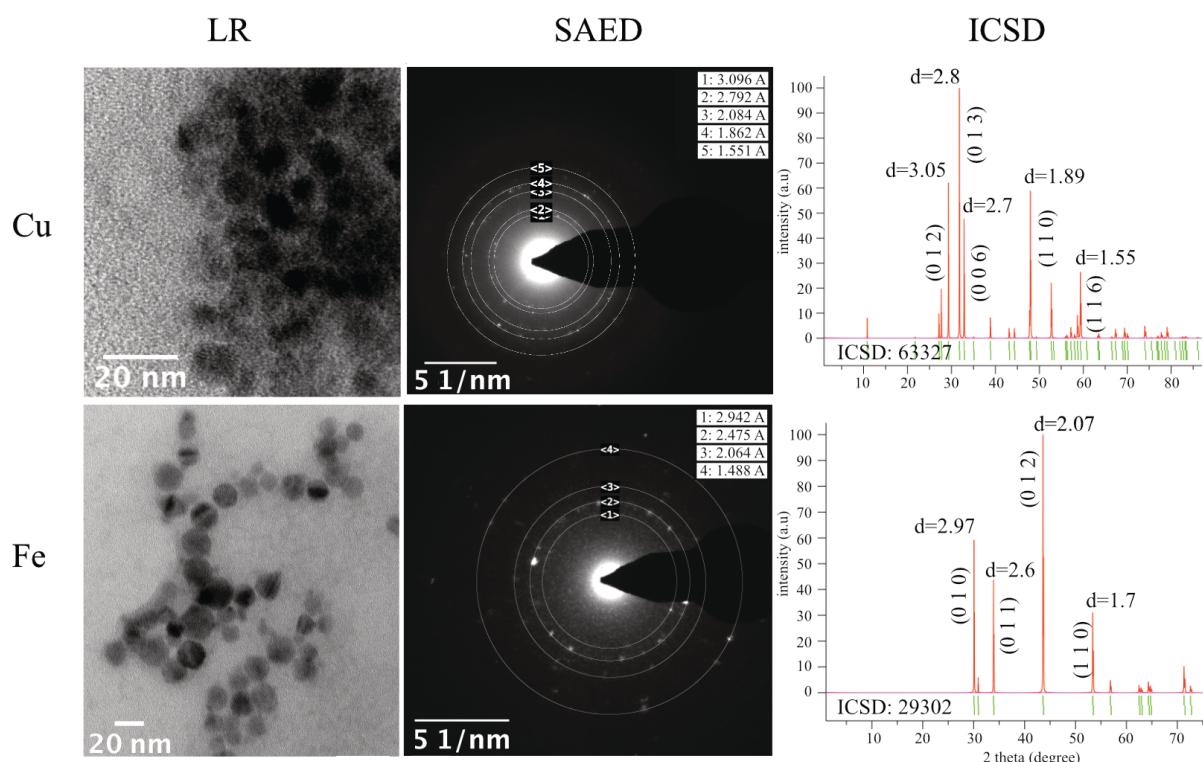
Figure 19. Transmission Electron Microscope analysis of obtained particles. LR: low resolution image of particles SAED: selected area diffraction of particles ICSD: powder diffraction patterns obtained from ICSD database. Shown here are results from particles formed on combustion of mesityl copper+THT+EHA and ferrocene+THT+xylene.

Although, Ferrocene as a compound is ideal to test the formation of iron sulfide the d-spacing of iron sulfides and iron oxides have a lot of overlap. Although it is distinguishable to a certain extent, due to it having a d-spacing value above 2.6 Å, the possible formation of iron oxides along with iron sulfides is harder to distinguish as the d-spacing values below 2.6 Å are very

close as shown in Table 4. Hence, as an initial test subject for single droplet combustion iron is inadequate to confirm beyond a doubt that only iron sulfides have formed. With the next clean source of metal, mesityl copper, is a more suitable test subject for confirmation of formation of sulfide alone as with copper, both oxides and sulfides have very distinct set of d-spacings making it easy to rule out the formation of oxides.

Table 4. Various iron oxides and their d-spacing values in angstroms (Å).

Known lattice spacing d_{hkl} (Fe_2O_3)	Known lattice spacing d_{hkl} (Fe_3O_4)	Known lattice spacing d_{hkl} (FeO)
2.519	2.531	2.484
1.842	2.099	2.152
1.487	1.484	1.521

Mesityl copper solution was combusted and the particles formed are shown in Figure 19. Here, the diffraction rings of copper analyzed correspond to d-spacing values of 3.096 Å, 2.792 Å, 2.084 Å, 1.862 Å, and 1.551 Å. The 3 most intense peaks in the powder diffraction pattern obtained from the ICSD database show good agreement to the d-spacing obtained from the SAED ring pattern. Although mesityl copper seems like an ideal source it is far too expensive to be successfully transitioned to large scale production in the future. As seen in Table 5, copper sulfide d-spacing can be sufficiently differentiated for various copper oxides. Here copper peroxide is omitted as it is known to decompose above 6°C in the presence of moisture and only known stable oxides of copper are considered.[156]

Table 5. Various copper oxides and their d-spacing values in angstroms (Å).

Known lattice spacing d_{hkl} (Cu$_2$O)	Known lattice spacing d_{hkl} (CuO)
2.531	2.484
2.099	2.152
1.484	1.521

Although, similar to metal acetylacetonates, metal nitrates are endothermic on heating they have been previously used in combustion studies to produce nanoparticles.[37, 157, 158] Here, as a wide library of metal nitrates are available, they are used for testing the formation and mechanism of formation. A precursor solution of one of the most used nitrate salts, zinc nitrate, is tested. In the particles produced from zinc nitrate solution, the two rings observed in SAED images correspond to d-spacing values of 3.08 Å and 1.86 Å (Figure 20). This d-spacing matches with the two major diffraction peaks of ZnS (1 1 1) and (0 2 2) with a slight shift. SAED images can be of varying quality. For nano scale objects or objects with a short-range order this can result in excessive brightness of the central area of the SAED image.[159] The visibility of spots on an SAED pattern also depend on the tilt of the sample. Here, the d-spacing is further confirmed through lattice fringe analysis on high-resolution TEM images showing lattice fringe spacing of 0.3 nm, supporting the formation of ZnS. Similarly, any other sulfides produced on a small scale can be characterized by repeating the above-mentioned methodology.
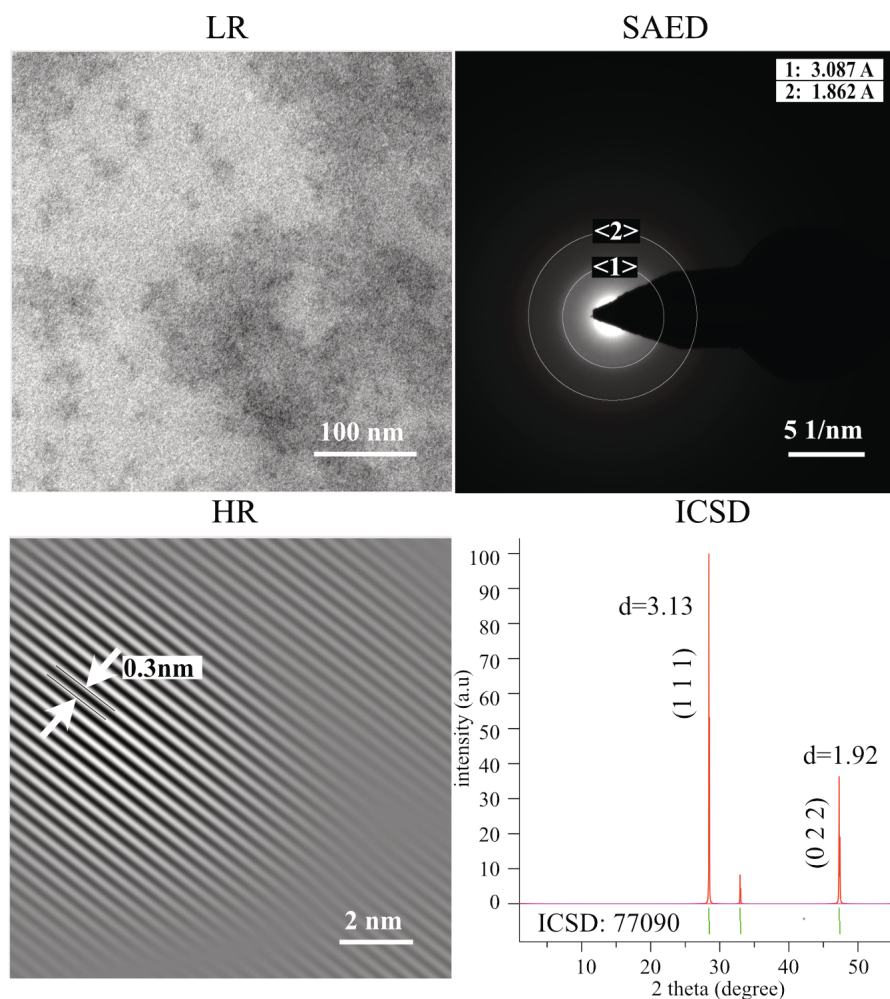
Figure 20. Transmission Electron Microscope analysis of obtained particles from combustion of zinc solution. LR: low resolution image of particles SAED: selected area diffraction of particles HR: high resolution image ICSD: powder diffraction patterns obtained from ICSD database.

3.3 UV-vis spectrophotometric analysis of solutions

UV-vis spectrophotometry is a relatively simple method to analyze solutions and their components. It was assumed that changes in solution on addition of each of the component to metal-sulfur precursor solutions could be observed using this technique. However, this proved to be challenging. An initial run of metal source in solvent was done and the spectra shown in Figure 21 was obtained. On the top row, analysis of copper solution is shown. First, a spectrum

of the solvent EHA in combination with THT and copper source (mesityl copper) was done separately. The concentration of THT and metal source were held constant in all solutions so that a comparison could be made. A similar analysis of zinc nitrate solution was also done. Here, ethanol is used as the solvent and separate two solutions of ethanol + THT and ethanol + zinc source were analyzed. Solvent used in both solutions is used as a reference sample during analysis. The addition of THT to zinc source and ethanol is also displayed. In both cases, a comparison of metal + solvent to sulfur source + solvent was done. The change seen in comparing both spectra is insufficient to conclude what changes, if any, are happening on a molecular level in solution between sulfur source and metal source. Hence, making the deduction of sulfur metal interaction in solution for different metal sources is difficult.
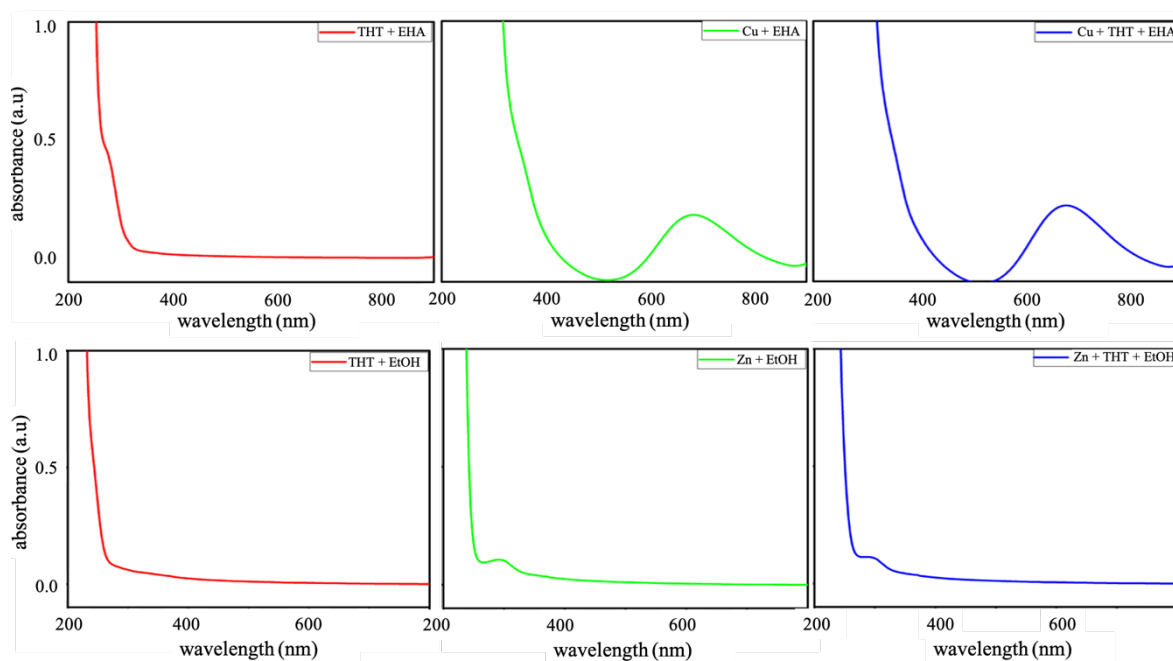
Figure 21. UV-vis spectrophotometric analysis of sulfur source + solvent, metal source + solvent and sulfur source + metal source + solvent was done on two different precursor-solution combinations. On the top row is solution analysis of copper which was made using mesityl copper, EHA and THT while the row is analysis of zinc made from zinc nitrate, ethanol and THT.

Although it is useful to determine concentration, it is difficult to separate peaks from individual components in the solution containing THT. This is clearly seen in Figure 21 that fails to show any significant changes or new peaks on addition of sulfur source into the solution. This makes difficult to determine, for example, if the concentration changes are equal or unequal for different components in the solution on evaporation. Fehnel and Carmack have shown that similar sulfur compounds such that of phenylmercapto group show little tendency to interact with other functional groups attached to the alpha-carbon and hence fail to show new absorption bands or displacement of maxima of the parent sulfide.[160] In another publication by the same authors, it was shown that an absence of characteristic absorption bands was observed for an isolated sulfone function in ethanol solutions. This is seen as the effect of conjugative interaction also in in aryl sulfones.[161] This could explain the difference seen in the spectra of THT with ethanol and that of EHA. For these reasons, here it was determined that using UV-Vis spectrophotometry was ill suited to study precursor-solvent solutions and their corresponding interactions.

3.4 FTIR analysis of solutions

With the failure of being able to deduce interactions of metal-sulfur sources in solution through UV-vis spectrophotometry, a switch was made to analyze solutions using FTIR. Shown in Figure 22 is a comparative run of solvent alone and solvent with sulfur source without any prior treatment. As seen, there is a lack of obvious peak indication or ability to deduce individual component peaks also on subtraction. The inability to observe any possible metal-sulfur interaction is instrument limited. After much pondering, two ways that complement each other so that metal-sulfur interactions can deduced were implemented.
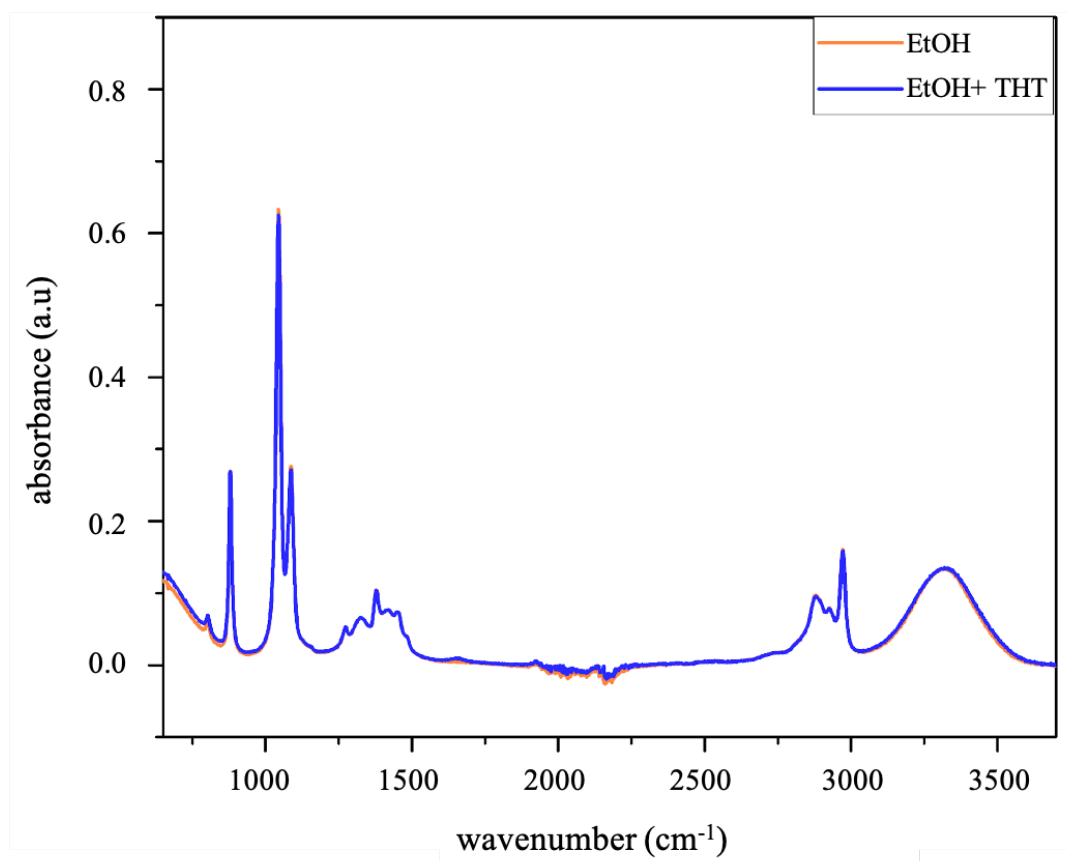
Figure 22. FTIR analysis of as prepared ethanol (EtOH) and a solution of ethanol and THT (EtOH+THT).

3.4.1 Room temperature evaporation

Metal-sulfur precursor solutions were left open under a chemical hood to observe the impact of evaporation. On evaporation the solution was observed to split into two immiscible layers. This is shown in Figure 23. As it is difficult to capture the splitting in a glass bottle, droplets of solution were suspended on a transparent fishing line and a time lapse video was made on an iPhone 13 to capture the evaporation. Once the split has taken place, syringes are used to carefully collect samples from both layers before individually undergoing an FTIR analysis.

In Figure 23 the result of FTIR analysis on the phase separated layers is shown. Also shown in the graph are spectra of pure THT and pure Ethanol to be used as a reference. As seen, the spectra of one of the immiscible layers traces the spectra of pure THT. An additional smaller peak is seen close to 1260 cm-1 which could indicate the presence of small amounts of ethanol. The second immiscible layer, however, fails to trace closely to any of the individual compounds that were used in the making of the solution. However, it does retain smaller peaks that indicate a slight presence of THT at 1260 cm^{-1}.
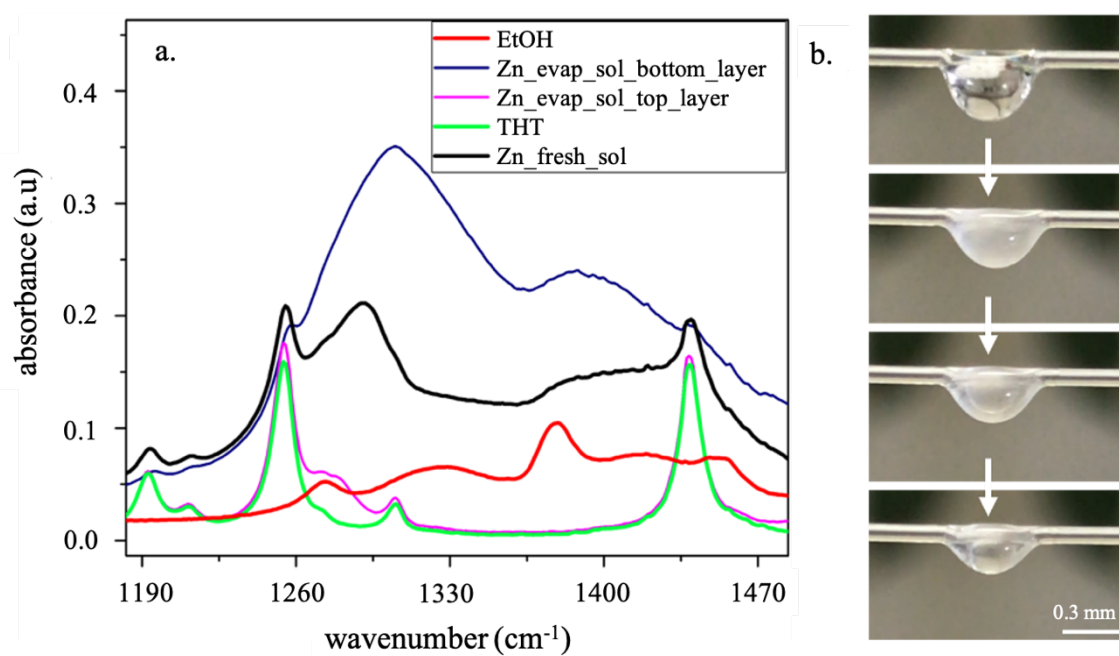
Figure 23. On the left-hand side, FTIR analysis of the splitting of metal nitrate precursor solution on evaporation is shown. On the right-hand side, a droplet of the metal-sulfur precursor solution undergoing evaporation is captured. Here, it can be seen that the starting solution is initially clear and turns milky right before a defined immiscibility is observed.

In droplets this separation has been determined to start at the periphery as evaporation flux is highest here.[162] This phase separation is triggered by non-uniform evaporation rates. In the zinc solution, this can be attributed to the lower boiling point of ethanol compared to that of THT. The process is observed to have three distinct steps – clear starting solution followed by a milky

looking phase after which two distinct layers are visible. The milky state, as seen also in Guo et al., can be attributed to formation of small regions of phase concentration which then come together to form a visibly separated phase.

In Rosebrock et al., shell formation is primarily attributed to particle formation on evaporation of precursor from droplet surface.[35] However, at room temperature evaporation, where rates are much lower than that of combustion, it has been observed that the liquid itself can turn milky and separate into different layer with differing viscosities. As shell formation was previously attributed to inhibition of evaporation, from bulk data it is seen that the increased viscosity of the liquid component could rather cause this. The solution composition and chemistry are likely to be the impactful parameters that lead to the visible shell in droplets.

The bottom layer was found to trace closely to the FTIR spectra of nitric acid as shown in Figure 24. pH paper was used to test the acidity of the layer and indicated a highly acidic solution. With this knowledge, the first infrared spectrum it was compared to was that of nitric acid as it is known that nitrate salts are the conjugate base of nitric acid. A closer inspection of the FTIR spectra of one of the two layers formed on separation of metal nitrate is shown in Figure 24(a). Peaks 1306 cm^{-1} and 1628 cm^{-1} correspond to nitrate ion coordinated with water.[163] According to Goebbert et al., peaks at these precise wavenumbers indicate that one molecule of nitrate ion is surrounded by 3 molecules of water. C-C-O peaks at 1044 cm^{-1} and 878 cm^{-1} indicate the presence of a remaining amounts of ethanol in the layer. OH bond stretching is indicated by the peak at 3318 cm^{-1}. The broad peak in this area also indicated strong hydrogen bonding.
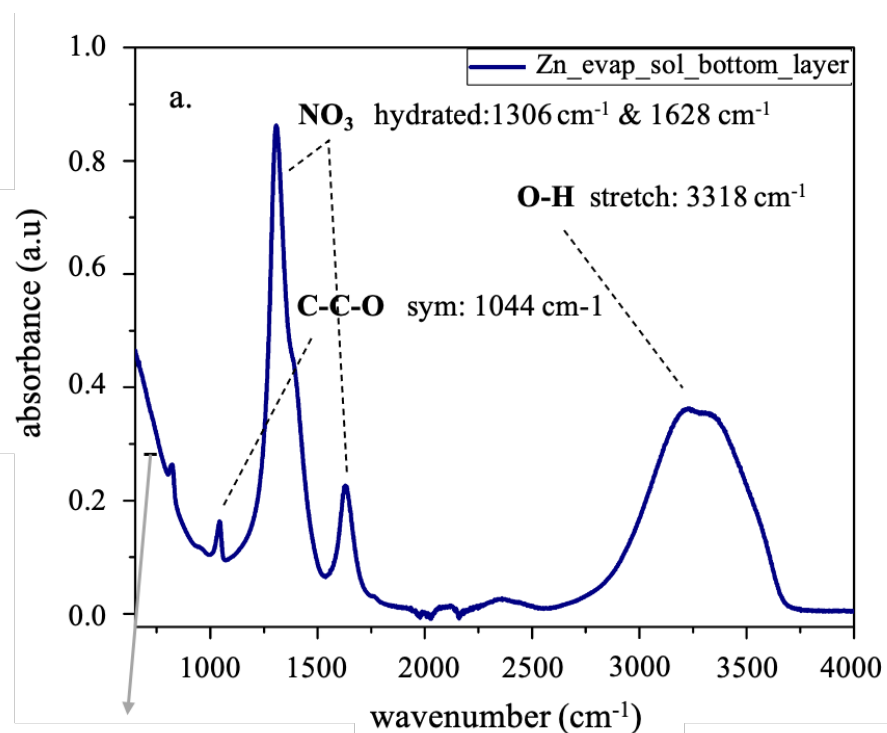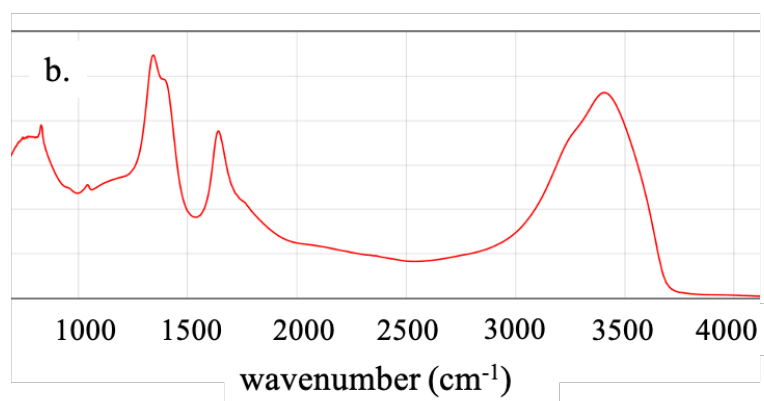
Figure 24. On the top is the infrared spectrum of the viscous layer formed on evaporation of zinc nitrate+THT+ethanol solution. Below is the infrared spectrum of 23.3% nitric acid in water obtained from the NIST Chemistry WebBook, SRD 69.

Similar peaks are present on evaporation of solutions of other metal nitrate salts with the same solvent, sulfur source and concentrations. This is demonstrated with the example of Gallium shown below in Figure 25. With infrared spectroscopy only functional groups can be elucidated. The region below 1500 cm^{-1} in the top immiscible layer for both Ga and Zn show significant differences. It can be deduced that this is a property inherent to most metal nitrate salts. With Zn, the top immiscible layer traces precisely along THT peaks except for two peaks,

one at 1513 cm-1 and the other at around 1003 cm^{-1}. This behaviour possibly indicates the lack of strong interaction between the molecules of THT and ethanol. This could also indicate possible weak hydrogen bonding between the two.
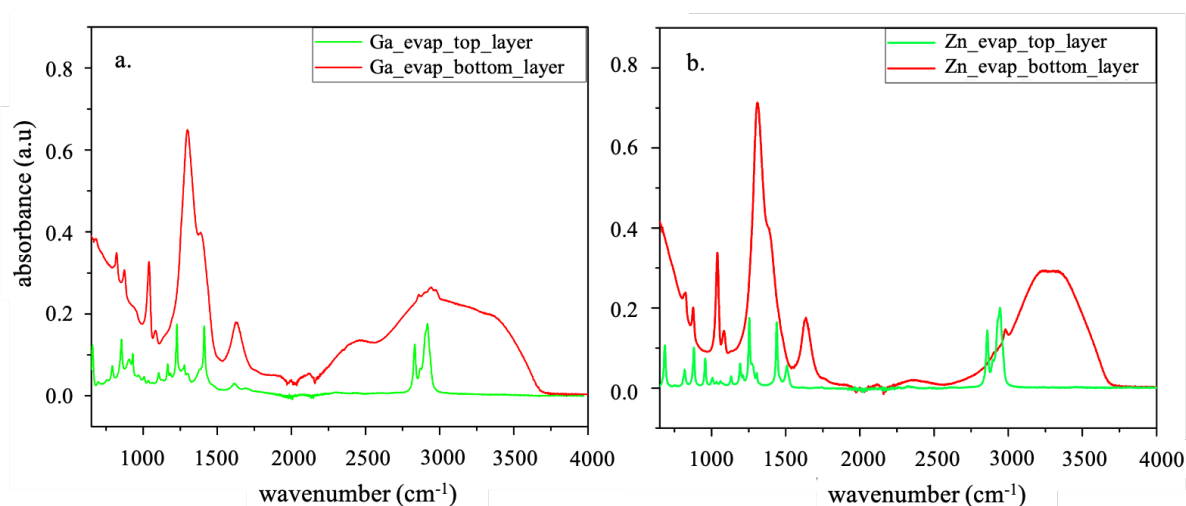
Figure 25. FTIR analysis of the layers formed of two different nitrate metal salt solution on evaporation. Both gallium (Ga) and zinc (Zn) show similarities in the immiscible layers formed.

Although unusual, the seeming lack of a strong interaction between THT and ethanol could partially be a result of THT being a saturated molecule. This suggests a less reactive molecule as a result of electron lone pairs on sulfur being unavailable for conjugation. I. Bezverkhyy and colleagues studied adsorption of THT on zeolites which showed the adsorption of THT on H-USY zeolite being completely reversible. The desorption from the acidic zeolite was almost complete at temperatures below 100 °C. Considering that the boiling point of THT is 121 °C, it is indicative of very weak interaction between the two and an absence of THT protonation. The authors state that the acidic nature of the zeolite plays an important role in the complete reversibility.[164]
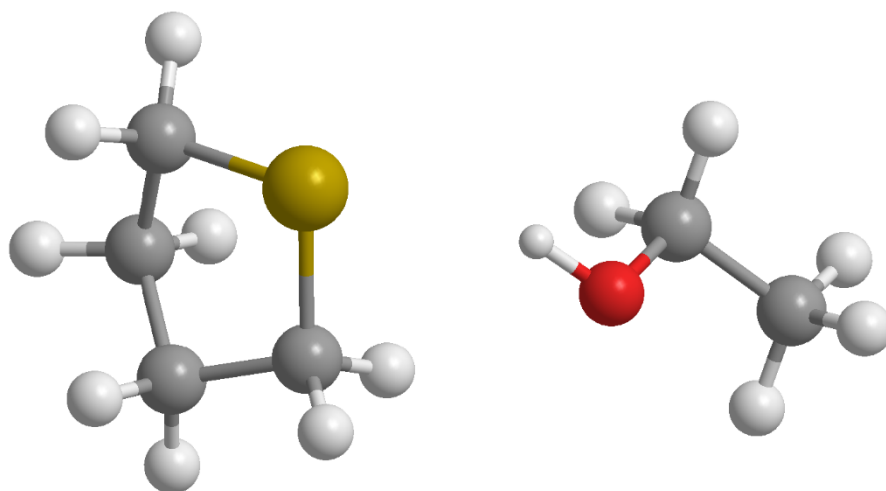
Figure 26. The image depicts and energy optimized configuration of THT and ethanol in solution. FTIR analysis shows this interaction to be weak and past studies have shown that an acidic environment can result in extremely weak interaction between OH group and THT molecules.[164]

As seen in this section, the solution combinations with THT, nitrate salt and ethanol are acidic in nature. A depiction of THT in the vicinity of an ethanol molecule is shown in Figure 26. A combination of an acidic environment with the stable nature of THT is determined to be the likely reason for the lack of strong interactions on evaporation of the solutions.

3.4.2 Distillation

From room temperature evaporation, an understanding of what components are left behind on evaporation was identified. To complement it and observe what components are leaving the solution a modified short-path distillation set-up was used. A short path distillation refers to the shorter path the distillate must take to be collected compared to traditional distillation set-ups. The intention here instead of purifying a distillate as much as possible is to condense the evaporated components at a short distance so that it keeps its concentration as close to the

initial vaporization as possible. This is to be able to analyze which components are leaving the solution on heating.

With simple distillation, vapours undergo multiple evaporation condensation steps which in turn increases the concentration of a certain component present in the vapour. This is also why distillation columns are used as they allow the vapour to undergo multiple evaporation condensation cycles before reaching the condenser for final condensation. To avoid a change in concentration from starting vapour as much as possible, a reduction of surface area and hence a shorter distance to collect the condensate is desired. As small quantities are used here, starting solution is 15 mL, modified short-path distillation is additionally appropriate.

The solution is placed in a three-neck flask with a thermometer in the middle neck. A side neck is fitted with a short glass periphery which is used as the collection arm. The third neck is fitted with a rubber stopper and used as the inlet to put the solution in (Figure 28). The flask is held into a circulating water bath using a support stand and clamps. The upper limit of temperature for the precision circulating water bath is 100 °C. However, as the water bath needs to be partially open to accommodate the three-neck flask into it the temperature of the water bath was kept at 93 °C which was the highest stable temperature possible for open heating of the system. As soon as distillate starts dropping into the collection container, a minute amount is collected and characterized using FTIR. This temperature is noted to be 78 °C.

In the distillate collected from the zinc solution as seen in Figure 27, it can be seen that the FTIR peaks trace that of pure ethanol well. There are smaller peaks present which then coincide with those of pure THT. This is seen as an indication that a combination of ethanol and THT initially evaporates together. The concentration of THT in the collected distillate is

extrapolated from correlation curves created from solutions with known concentration of THT in ethanol.
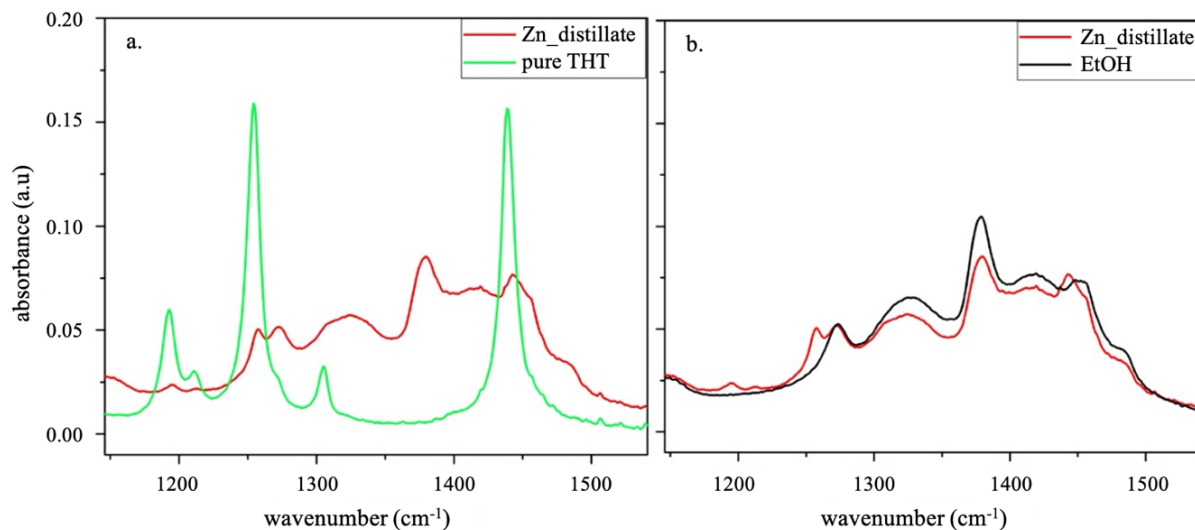
Figure 27. Distillate obtained from modified short-path distillation of zinc nitrate+THT+ethanol precursor solution is shown here. On the left hand side it a comparison to the spectrum of pure THT is done and on the right side a comparison to ethanol. As seen, it traces well with the spectrum of ethanol with minor smaller peaks of THT.

To create a correlation curve, Ethanol-THT solutions with well-defined and known concentrations were created and individually run through an FTIR analysis. Three difference concentrations were chosen as shown in Figure 28. Having obtained the FTIR spectra of each well-defined ethanol+THT solutions, a wavenumber at which pure THT has a prominent peak that also avoids overlap with peaks of ethanol was chosen. At this wavenumber, the intensity of peak of the ethanol+THT solution is noted. From the same ethanol+THT spectra, pure ethanol spectrum is subtracted and a new curve is obtained (labelled as sub. THT in Figure 29). The intensity of this curve at the same wavenumber is also noted. This is then repeated for each solution of ethanol+THT with a different concentration. Using these collected intensities of solutions with defined concentrations, molarity versus intensity is plotted at defined

wavenumber. With this, an extrapolation of molarity can be performed from intensity at given wavenumber. This is depicted in Figure 29.
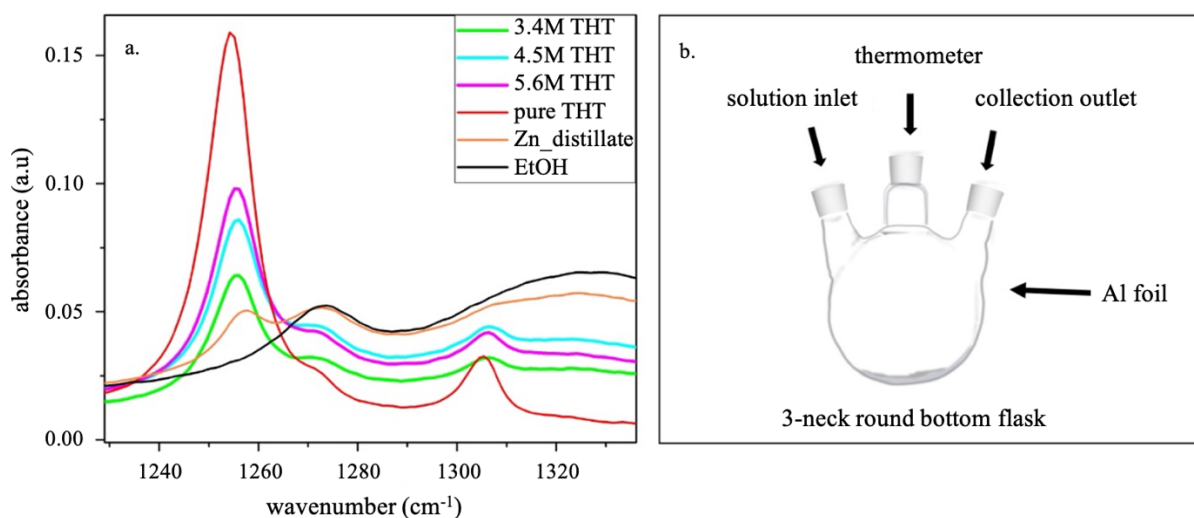
Figure 28. Shown here is an overlapping of spectra obtained from ethanol+THT solutions of varying concentrations along with that of distillate obtained and pure ethanol. On the right hand side, a simple demonstration of the modified short-path distillation that was used to collect the distillate is presented.

The resulting concentration of THT in the collected distillated for zinc solution is extrapolated to be 2.42M. In 10 ml of solution with 1:20 M:S concentration, 5.5 mL of it is ethanol. On evaporation of the ethanol, the amount of THT projected to evaporate alongside it can be extrapolated that approximately 70% of the THT is left over with the metal compound. Although this is an idealistic assumption, with the reality being that parts of ethanol could still be left behind it still indicates that increased concentrations of THT will be in contact with the metal source. From this, the inference can be made that the concentration of sulfur surrounding the metal at higher temperatures after ignition of the droplet will be higher than in the starting solution.
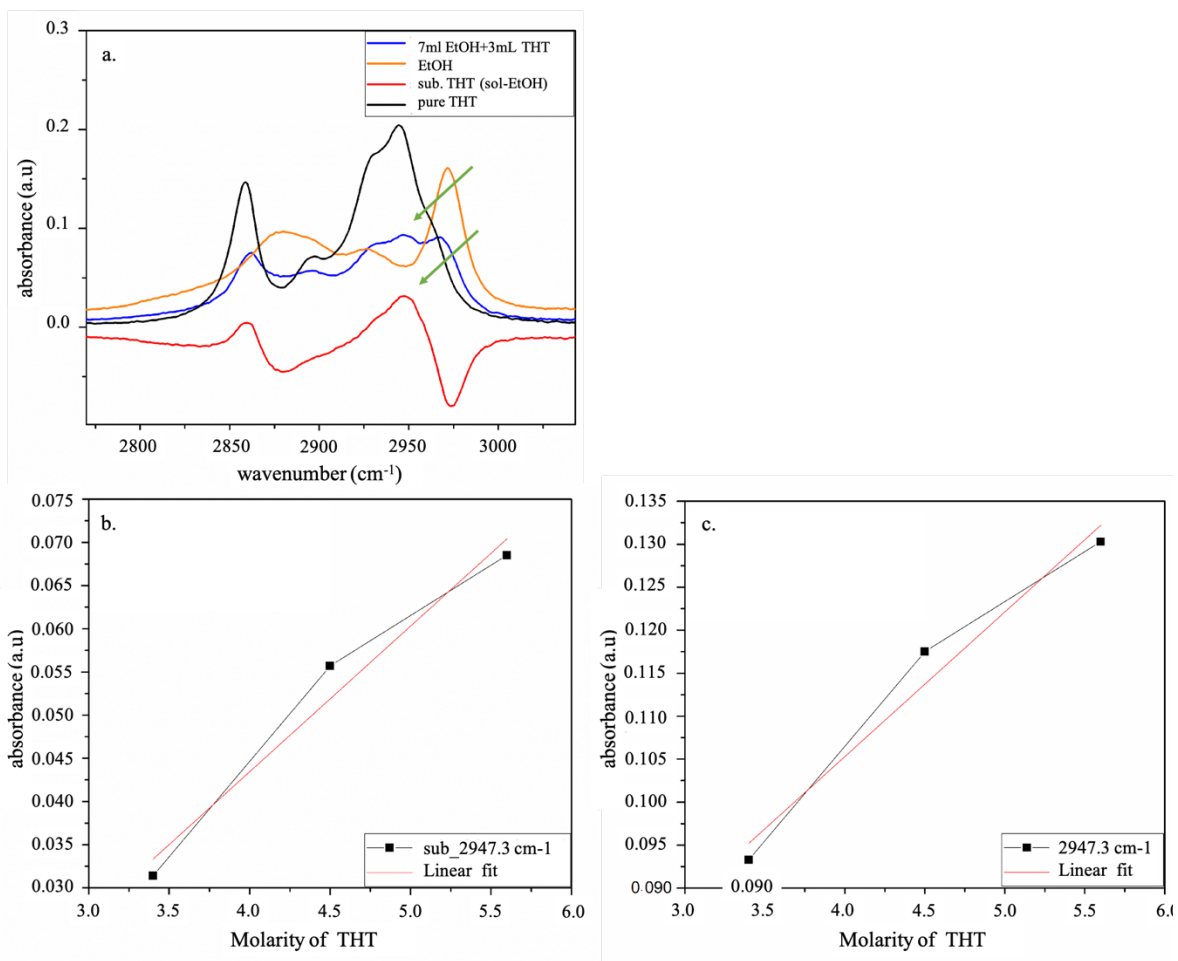
Figure 29. Above, spectra of known concentrations of ethanol+THT, ethanol+THT – pure ethanol, pure ethanol and pure THT as displayed. Green arrows indicate the position of intensities that are noted for the particular wavenumber. On the bottom, linear fit of intensities obtained from both the spectrum of known concentration solution as well as the subtracted curve are displayed.

Distillation of the exact solution with only changing the metal precursor to a different nitrate salt was done to observe if the metal has a significant effect on the initial compounds that are seen vaporizing. Displayed in Figure 30, for distillates of solutions using copper nitrate, zinc nitrate and iron nitrate. As it can be observed, the peaks are at similar wavenumbers with only small changes in intensity. As FTIR is a very sensitive analytical technique, this difference in intensity is very likely due to the minute time difference in collecting distillate. This is a clear

indication that the initial distillate is expected to be independent of the metal. The implication is likely that on burning, metal nitrate salt solutions initially exhibit similar behaviour.
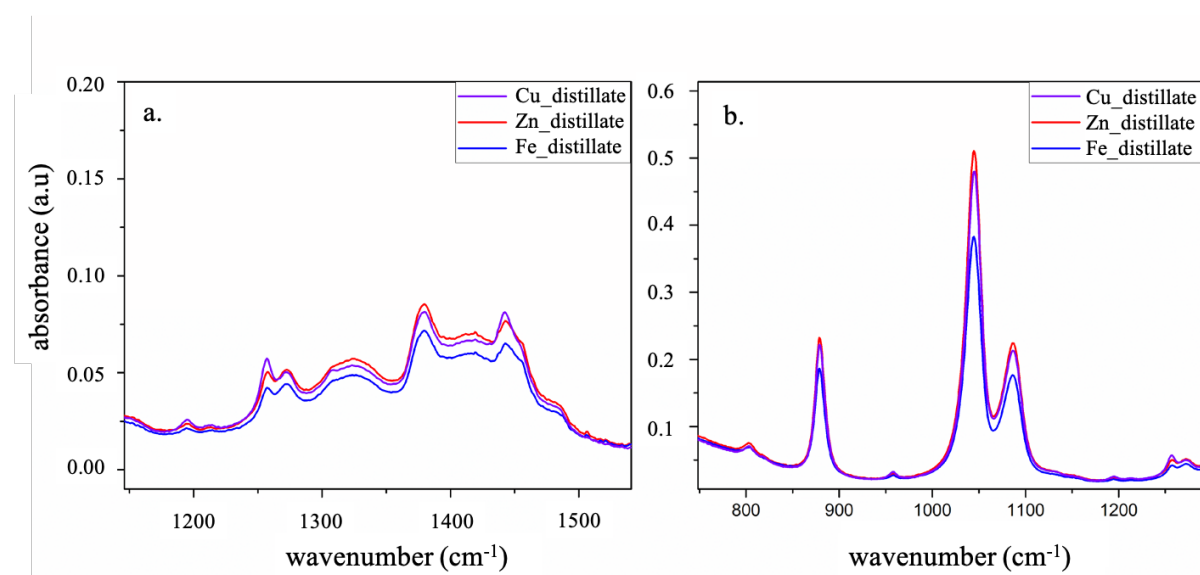
Figure 30. Two different ranges of wavenumbers showing the similarity in infrared spectrum of solutions with metal (zinc/copper/iron) nitrate+THT+ethanol.

3.5 Solution interactions

The observations in the sections above come together on inspection of the process of single droplet combustion of the metal-precursor solutions. This can be seen in Figure 31. Shown here are the combustion of zinc nitrate precursor (on top) and lithium nitrate precursor (below). Metals that burn with distinct colour are especially useful as their onset of starting to burn is visible through the distinct colour imparted to the flame. It is known that pure ethanol burns with a bluish flame with limited luminosity.[165]

The process seen in Figure 31 can be broken down into two distinct regions - 1. region with predominant burning of ethanol and 2. region with predominant burning of metal. In this section, the focus lies in the first region. Here, it can be seen that the flame colour consistently

shows two distinct regions even with different metals. Inferring from section 3.4, this is predominantly ethanol burning with smaller amounts of THT. As there is a significant loss of ethanol in this region, the concentration of THT in relation to the metal source will increase. It is also likely that there could be interactions of THT with metal compounds at these elevated temperatures. According to Clark and colleagues, at elevated temperatures metal ions can result in desulfurization of tetrahydrothiophene. In their work, desulfurization is studied over a period of 7 days.[166] As the time frame is much shorter here, it is likely that desulfurization could happen to a very small extent and can be overlooked. Hence, here it is assumed that liquid phase reaction between sulfur and metal is negligible and the product forming interaction between the two take place in region 2. From this, it is also unlikely that ethanol as a solvent is heavily intertwined in the final sulfidation reaction.

From section 3.4, it has been established that evaporation of ethanol from the solution results in an increase in acidity as well as the formation of two immiscible layers. Although, temperatures, heating rates and hence evaporation rate will be different when the solution is burning, the formation of shell structure on a burning droplet is well documented in literature.[35] Even though different combination of chemicals were used in previous studies, it is likely that the composition also effects observations. For example, the increase in acidity noted here is determined to be mainly contributed by the formation of nitric acid from the nitrate group present in the metal source. It is likely that different classes of sources will depict varying behaviours.
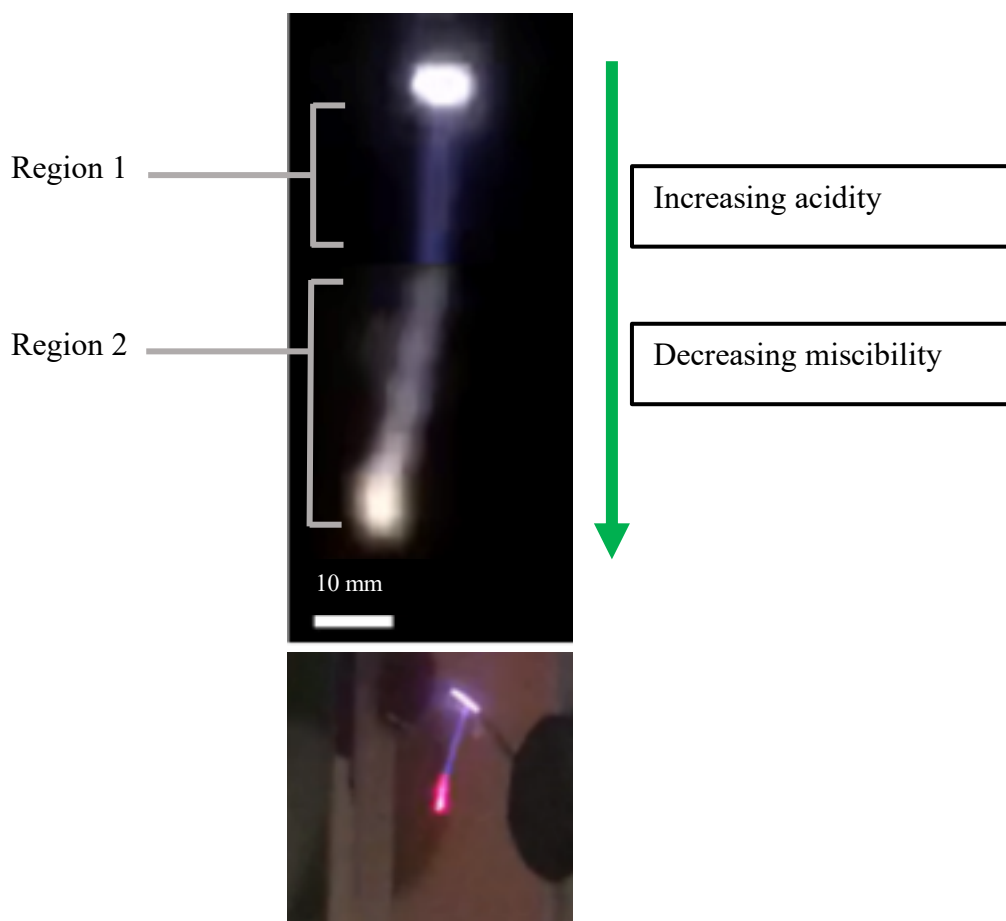
Figure 31. A droplet of zinc nitrate+THT+ethanol being combusted where two distinct regions can be observed. Below, a droplet of lithium nitrate+THT+ethanol combustion is captured. Here too, distinct regions of burning can be observed along with the characteristic flame colour of lithium. Images of combustion captured by and obtained from ERC ReSuNiCo PhD candidate Jan Derk Groeneveld.

In region 2, it is clear that the metal compound burns at this stage. The distinct flame colour from different metals confirms this. The left-over liquid in region 2 as interpreted from section 3.4 is made of a majority metal source and THT, it is inferred that in this region remaining THT burns along with the metal. This ties in with the other observations in section 3.4, where on evaporation the solution splits into two immiscible region (seen in Figure 23). It can be deduced that it is likely the inner region of the droplet in Figure 23 that contains the metal ions along with a majority of THT. With this, a clear pathway leading to the formation of metal

sulfide nanoparticles can be constructed through solution evaporation and distillation studies along with identifying compounds at different stages of the process using FTIR analysis.

As it has been determined that a liquid phase interaction between sulfur and metal is insignificant, the reaction taking place in gas phase takes precedence. To obtain a better understanding of what proceeds to happen, high temperature breakdown of THT must be considered.

3.6 High temperature breakdown of THT

High temperature breakdown of THT is crucial to understand how the gas-phase reaction with metal ions ensues. Cracking of organosulfur compounds is generally widely studied as they are a major component in crude oils. It is also known that cracking of organosulfur compounds to produce H_2S requires large amounts of water vapour and is a standard industrial process. Although, literature on cracking of THT is limited they are in agreements that for the usual thermolysis route

As the combustion of THT here is free of any water vapour introduced intentionally, it is hypothesized that the breakdown likely differs and generation of H_2S would then need further verification. The breakdown of THT, and hence the sulfur containing fragments that are most likely to result in the formation of metal sulfide is important to understand the final mechanism of formation through the combustion process. For this, thermogravimetry coupled with a mass spectrometer was utilized. THT as is from Sigma Aldrich was put in an aluminium oxide crucible and loaded into the TG couple to a mass spectrophotometer. Pure argon flow was used

here with 20 L/min protective flow coupled with a 50 L/min co-flow. The heating cycle of 10 K/min was used. The detected and obtained atomic mass numbers by mass spectroscopy is shown in Figure 32.
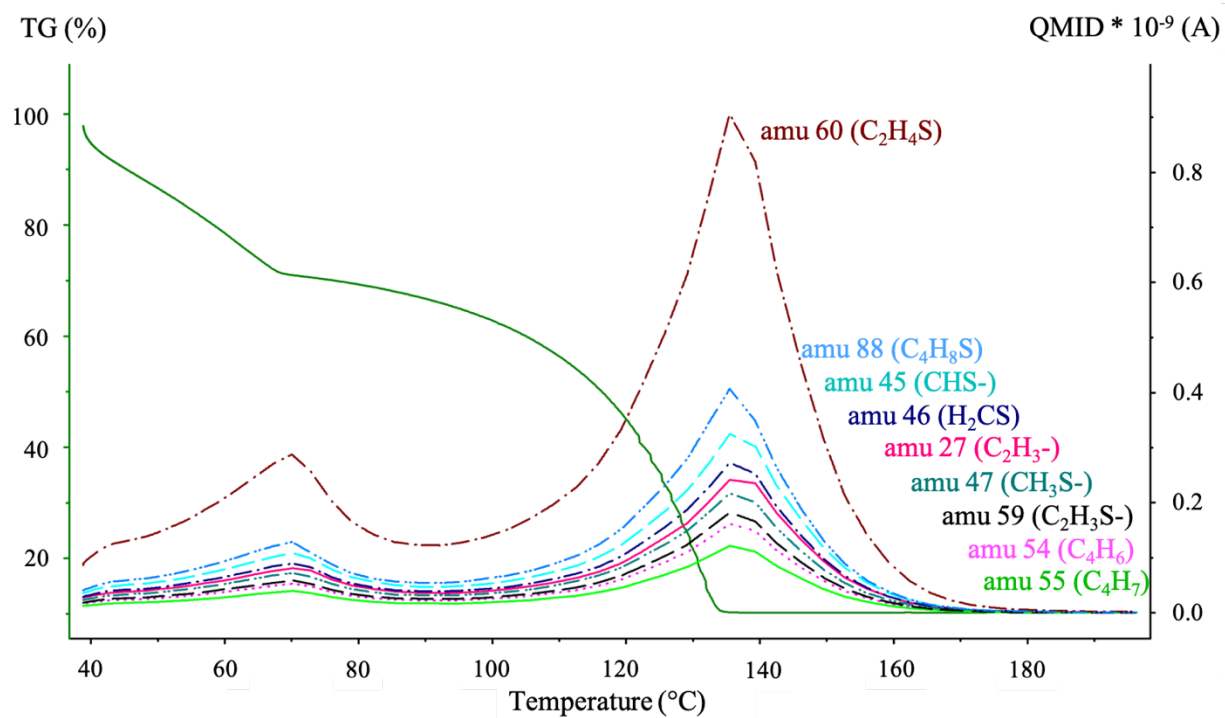
Figure 32. TG-MS analysis of pure THT. Shown here is the breakdown of THT at higher temperatures into smaller fractions.

In mass spectroscopy, the more abundant the ion the more intense the signals are for individual amu. The amu is either matched using a database provided by Netzsch or manually using a NIST database. This is because the database provided by Netzsch is limited to about 250,000 compounds. As THT and its fragment are scarcely studied, a more comprehensive database is needed to match the amu to corresponding fragment. There is still the whole molecule of THT detected with amu 88 but amu 60 is observed to be the most abundant and amu 60 is most likely to be a cyclic fragment containing sulfur and two carbon atoms.

The individual analysis of THT is additionally interesting because in previous studies there have been disagreements on whether H_2S or CS_2 are primarily the sulfur compounds that then form as a sulfur-giving source to metals. Results from the mass spectrometer shows that the most abundant ions are those with atomic mass unit (amu) 60. This is an indication that the disintegration of the compound starts with the bonds between C1-C2 and C3-C4. The structures that form from this breakage are a cyclic sulfur compound and two-carbon chain. Further breaking apart of amu 60 is indicated by the presence of amu 45, 46, 47 and 59. The fragments 54 (C_4H_6) and 55 (C_4H_7) imply that the other most probable pathway is a break away of sulfur with hydrogen.
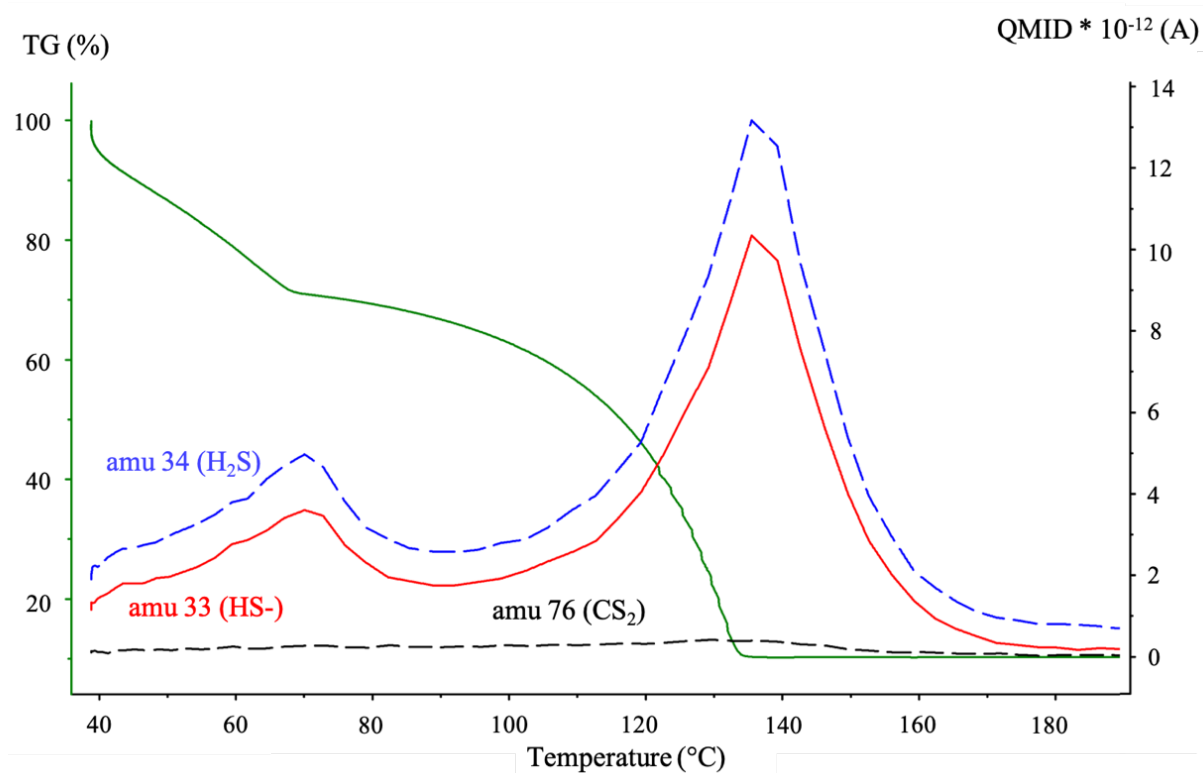
Figure 33. TG-MS analysis of pure THT. Shown here are the select atomic mass units of H_2S, HS⁻ and CS_2 on the breakdown of THT at higher temperatures.

The profound observation here is that the ionic current strength of CS_2 and H_2S in comparison to other sulfur fragments is negligible (Figure 33). This assessment is in contradiction to studies

that imply the main fragmented sulfur component is H_2S.[30, 167] In Xia et al., after thermal cracking of THT water and nitrogen are pumped into the reaction chamber which is said to aid in moving products out before detection.[168] Although they state that the introduction of water vapour has nil effect on the reaction and product distribution, Clark and colleagues. have shown that reactions and yields of reaction products is different when cracking of tetrahydrothiophene is done with and without the presence of water.[169] This is due to the fact that in both cases, water is the only source of oxygen in the system. In their work, the introduction of oxygen in the system is shown to increase carbon dioxide yields. However, in the absence of oxygen there is seen to be a higher yield of fragments with small molecular weight.

Figure 34. The possible breakdown path of THT at higher temperatures into smaller fractions is depicted here. With the abundance of amu 60 it is hypothesized that the breakdown initiates with C-C bond cleavages resulting in sulfur containing fragment of amu 60. The further breakdown of amu 60 then results in smaller sulfur fragments of amu 47, amu 46, amu 45 and amu 59.

Cracking of organosulfur compounds is generally widely studied This can also be seen in the study from Lin et al. where the concentration of H_2S formed is insignificant.[170] Here, for 1g of THT 10 g of water is used with a reaction time of 24 h. Water vapour essentially provides the oxygen needed for the reaction but in the production of sulfides excess oxygen supply is avoided to prevent formation of metal oxides. The absence of detection of other sulfide fragments in gas is likely due to the set up shown where a gas detection is placed specifically for H_2S.

3.7 Mechanism of formation in gas-phase

To elucidate the mechanism of formation of metal sulfides through the combustion of precursor solutions, combining individual component high temperature breakdown studies along with high temperature breakdown of the precursor solution is used. For representative purposes, the mechanism of formation of zinc sulfide through the combustion of zinc nitrate and THT in ethanol is shown here. Depending on changes in metal sources while using THT as the sulfur source, it is likely that there are changes in formation mechanism. Most metal nitrates as a class of compounds have shown similar behaviour on interaction with THT.

Individual analysis of zinc nitrate in TG-MS shows H_2O slightly above 100ºC, as exhibited in Figure 35. This shift to higher temperatures is most probably because of the time it takes the gas molecules to be transported through the transfer line from TG to the mass spectrometer. Above 300ºC intense peaks of NO and NO_2 are seen which indicate a breakaway of the nitrate group. This is seen to happen in steps, first occurring slightly above 200ºC to a small degree followed by the second one starting above 250 ºC and intensifying on reaching temperatures above 300 ºC. This temperature is likely to shift when heating rates change. Here a heating rate of 10 K/min was used. In combustion synthesis, heating rates tend to be much higher and hence

can significantly influence when this step occurs. Such high heating rates are unable to be reproduced in the TG-MS machine.
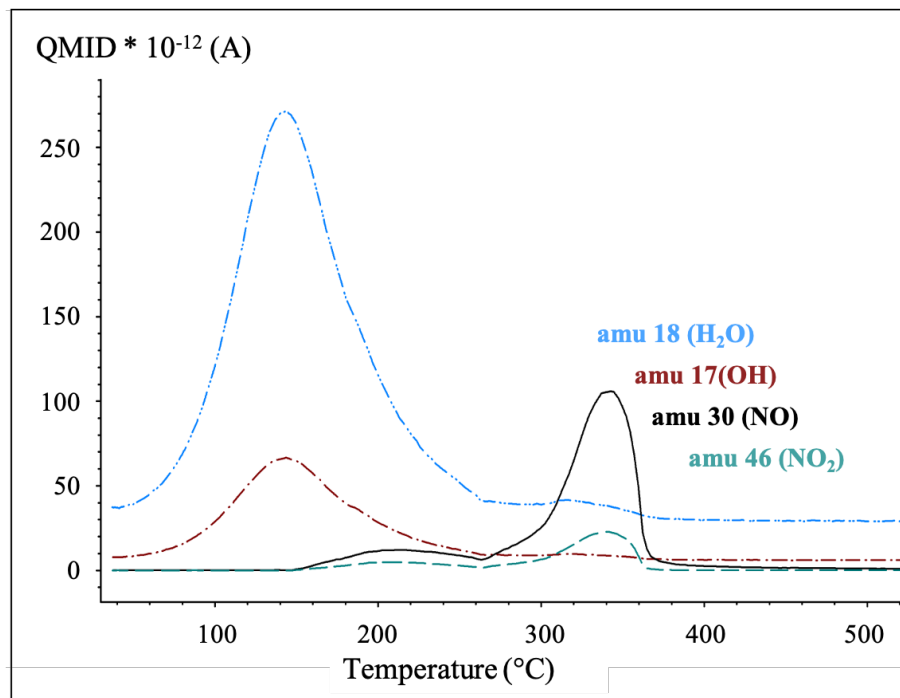
Figure 35. High temperature breakdown of zinc nitrate hexahydrate salt used in precursor-solvent solution

Analysis of the precursor-solvent solution of zinc nitrate + THT + ethanol using mass spectrometry is shown in Figure 36. Accompanying the peaks of NO and NO₂, peaks contributed by THT are observed at temperatures that were unseen in pure THT. This is likely an indication of strong interaction in solution between metal salt and THT that disintegrates at higher temperatures. Interestingly, in solution, the intensity of the fragments of THT have different relative intensities as compared to that in pure THT in the temperature range above 200°C. Here, amu 45 is dominant, followed by amu 60, amu 47 and amu 59. The structures are as shown in Figure 34. This can be due to ethanol also contributing to amu 45. Amu 29, which is contributed by ethanol is seen positioned right above amu 88 contributed by THT. This is an indication that small amounts of ethanol are still present in the solution when the solution

reaches superheating temperature of ethanol (189.5ºC).[171] The high temperature region sees negligeable intensity from H_2S or HS^-, implying an absence in their contribution to transformation of Zn ions to zinc sulfide.

As it has been determined that the formation of zinc sulfide occurs at high temperatures at which disintegration of individual components has taken place, the inference that sulfur containing fragments present on disintegration is likely to assist in the formation of metal sulfides. The prominent sulfur containing fragments seen are CHS^-, C_2H_4S, CH_3S^-, $C_2H_3S^-$ and H_2CS.

Additionally, below 120ºC the relative intensities of THT peaks in Zn+THT+EtOH solution remain the same, without regard to amu 46 as it accounts for as NO_2 as well as amu 27 and amu 45 which can also arise from species contributed by ethanol. To confirm the existence of species arising from ethanol, amu 29 is looked at as there is an absence of overlap with prominent peaks of species of THT or zinc nitrate. In pure THT amu 60 is clearly the dominant fragment in both under 90ºC and above 100ºC regions. In the zinc solution, the region under 100ºC, it is seen that amu 45 is the dominating species until 75ºC. A similar behaviour can be noticed with amu 29 too, confirming the contribution of ethanol to amu 45. This adds to the observation from previous sections of initial burn away of ethanol and THT which would then be followed by a burning of THT with metal components and small amounts of ethanol.
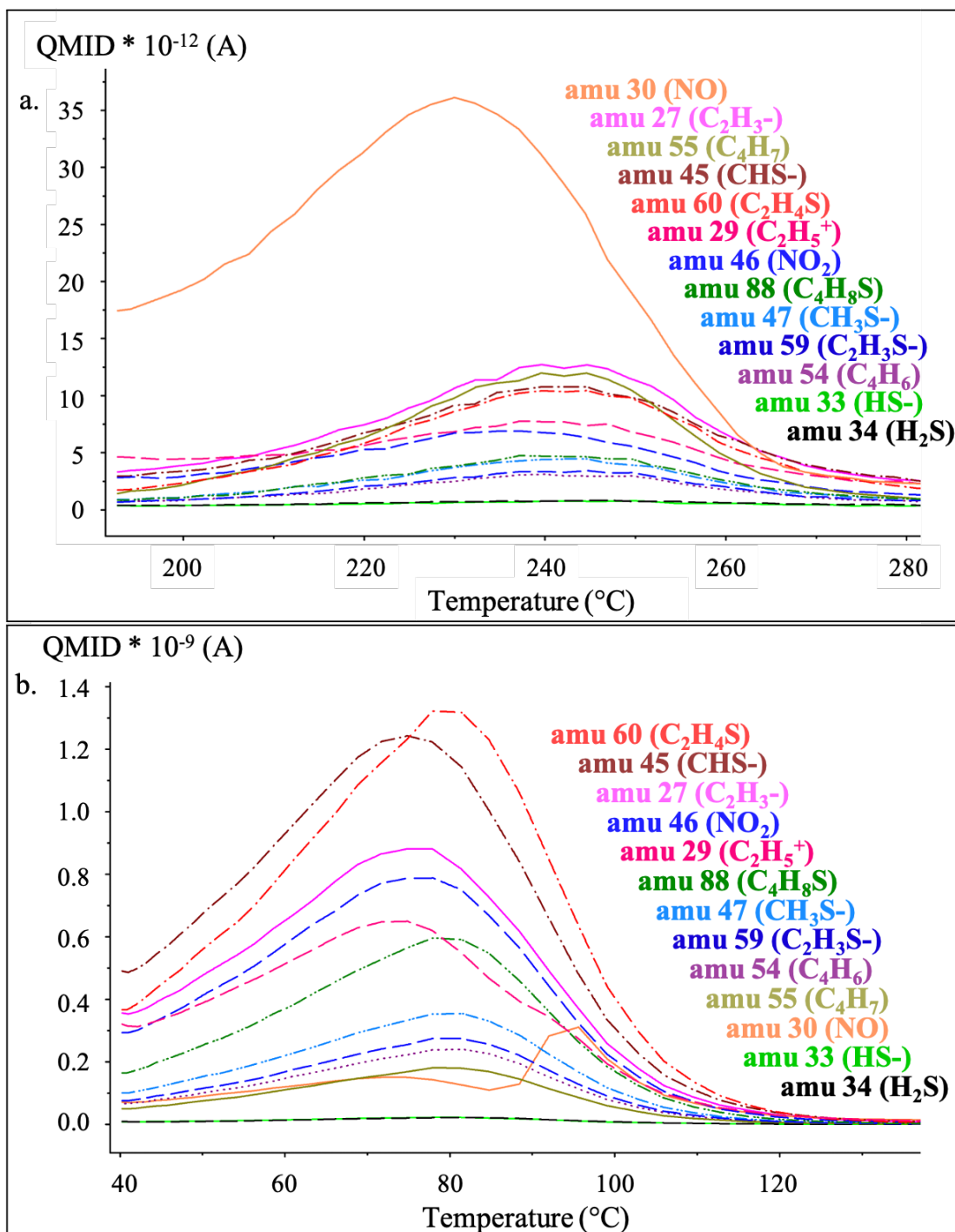
Figure 36. High temperature breakdown of zinc nitrate + THT + ethanol solution analysed using mass spectrometry. a.) Temperature region above 200°C b.) Temperature region below 120°C. The atomic mass units (amu) are shown in descending order of intensity (from top).

The difference in the relative intensities of amu 88 compared to that of 46 and 27 in pure THT below 120ºC can likewise be explained through the contribution from different compounds to the same amu. NO_2 fragment contributes highly to amu 46 and ethanol partially contributes to amu 27 here. As amu 46 is the dominant peak of NO_2, it is the corresponding fragment attached to amu 46 in Figure 36.

Above 200°C, a dominance of amu 55 (C_4H_7) is observed although this behaviour is unseen in pure THT or in zinc solution at lower temperature. Considering the fragmentation caused by electron impact before detection of molecules in a mass spectrometer, the intensity of amu 55 in pure THT and zinc solution below 120°C remains relatively stable hence suggesting the epicenter of this phenomena happens before species reach ionization. As the second stage burning of THT with metal has been established in previous sections, the reaction of THT with metal ion is the probable cause of the usual peak of amu 55. It is possible that THT has partially reacted with the zinc when temperatures were ramped up. As in single droplet combustion, the time duration of the droplet at high temperatures in a fraction of the time (a few micro seconds), it is considered to be the less dominant path of formation of sulfides.

As other sulfur fragments in addition to amu 55 are still detected above 200°C in zinc solution, it is likely an indication of the excess sulfur present when creating solutions. NO (amu 30) is observed to be the most abundant ion at 230°C but unseen beyond 300°C as in pure zinc nitrate. This suggests the last release of NO and NO_2 takes place along with fragments of reacted and unreacted THT. The quantities of HS^- and H_2S detected remain negligible in the region below 120°C and region above 300°C. As H_2S was also detected in negligible quantities in the high temperature breakdown of pure THT, it negates the involvement of H_2S as contributing to the

formation of metal sulfide. In the breakdown of zinc solution both HS^- and H_2S are observed to be almost nonexistent compared to the other species detected (Figure 36).
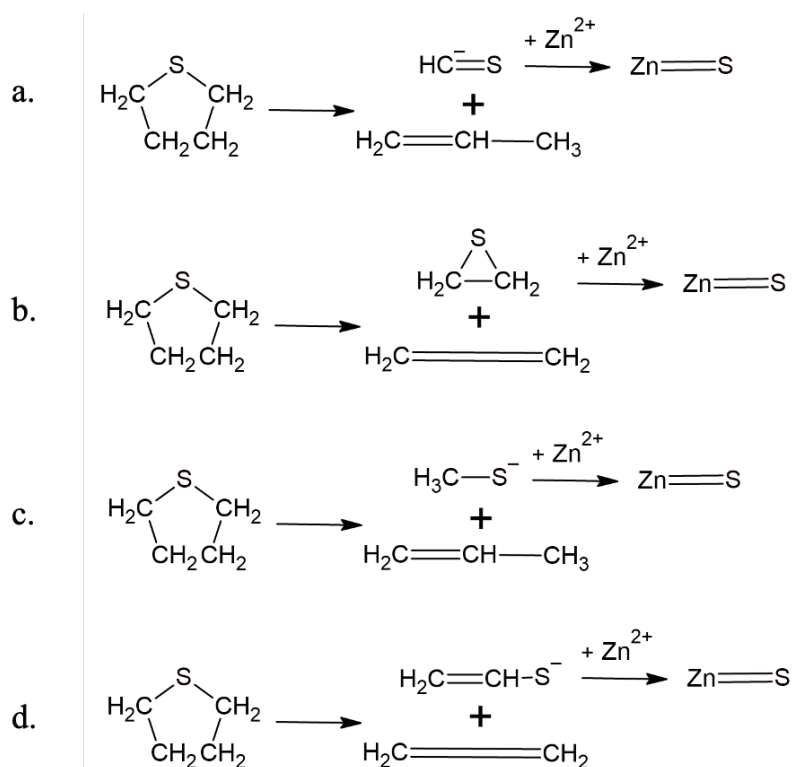
Figure 37. Possible formation pathways of THT breakdown products interacting with zinc ion to form zinc sulfide.

The overall mechanism of formation of zinc sulfide at high temperatures and short durations with THT as the sulfur source is expected to occur through interactions with sulfur fragments of THT. This is depicted in Figure 37. The fragmentation of THT whether alone or in combination with other precursors appears to remain constant. Depending on the fragments of sulfur, the complementary remaining carbon chain is also depicted in Figure 37. The inference is that a metal ion in the gas phase will react with the disintegrated parts of THT observed to form metal sulfide nanoparticles.

3.8 Summary

Beginning with identifying sources for precursor-solvent solution combinations for combustion synthesis of metal sulfides, this work has gone further and to provide new insights into processes that can be utilized to establish reaction pathways of precursor-solvent solutions and methodology to identify interactions leading to the formation of nanoparticles.

Overall, the following has been accomplished - (1) identified viable metal and sulfur sources/classes (2) shown viable precursor-solution combinations using metal and sulfur sources for single droplet combustion (3) added insight into chemical interaction in solution on evaporation (4) shown simple distillation as a viable option to understand solution behaviour on heat treatment (5) elucidated mechanisms breakdown of sulfur source THT and overall reaction.

In other studies that produce metal sulfide nanoparticles through combustion which are described in detail in section 1.2.1, it is likely that the metal is interacting with species of sulfur other than H_2S. It must however be noted that the reaction schemes found in these studies are simplified. The need of large amounts of water or oxygen to produce H_2S is known and is also discussed in section 3.6. The need to avoid an oversupply of oxygen or water to produce metal sulfides combined with the knowledge generated here of the breakdown and interaction of THT, one of many sulfur containing sources, it is highly probable that the highest contributing sulfur fraction will vary depending on the sulfur source being used.

Conclusion

In this work, viable metal and sulfur sources are established that can be used and have the potential to produce metal sulfide nanoparticles through the process of combustion of liquid precursor solutions. The most versatile sulfur source is recognized to be tetrahydrothiophene (THT). THT is highly combustible, dissolves in a wide range of solvents, dissolves a wide range of metal salts as it is liquid form and is considered a clean source of sulfur possessing only S, C and H in its molecular structure. Although it does have a foul and overbearing smell, lending its use to odouring of natural gases, handling it under chemical hoods with proper protection one can avoid (figuratively) getting punched in the nose. THT is also economical for future large-scale production.

Metal nitrate salts as a library for metal sources with similar characteristics was also established. Commercially, there are nitrate salts of at least 40 different metals available. As seen, there are similarities in their dissolution, interaction with sulfur source THT and evaporation characteristic in precursor-solvent solutions. As metal sulfide synthesis using combustion on a large scale is new and needs more insight, this library can provide excellent testing material. However, production of metal sulfide nanoparticles through combustion can be done using other classes of metal sources as well. For special materials, as seen in

combustion synthesis with multi-metal oxide nanoparticles, it is likely that precursors must be specifically picked due to dissolution challenges that can arise.

The main challenge in this work was to figure out a way to understand what interactions and processes could be taking place leading to the formation of metal sulfides. Challenging because working specifically only on the solutions there was an absence of a predefined way to go about realizing this. The initial use of UV-vis spectrophotometry to analyze solutions and changes in various interactions such as solvent-metal, solvent-sulfur and solvent-metal-sulfur proved to be unfeasible with various classes of metal precursors. As the FTIR spectrum is akin to being a fingerprint of a compound, it was the next choice of analysis. Nevertheless, running prepared solutions as such and comparing them to study the changes also proved to be difficult to find insight into metal-sulfur interactions as nothing changed in terms of functional groups coupled with the limitations of the instrument to analyze in the region 200-400 ccm^{-1} which is where peaks of sulfur and metal interaction are usually observable.

The idea to let bulk precursor-solution combinations to evaporate to simply observe the process turned out to be the path that led to some fascinating findings. Observations of splitting of solution into immiscible layers was seen. To try to capture this phenomenon on camera a fishing line was used to suspend a droplet of solution. The shell-like structure that it exhibited on evaporation is reported to form in droplets undergoing combustion. Evaporation combined with FTIR analysis showed what was left over on evaporation. As observations were made on what is left behind on evaporation, a way to look at what was evaporating initially was formulated. To be able to collect the vaporized material, condensation was needed. This pointed towards distillation. However, in the process of distillation, the vapours undergo multiple evaporation condensation cycles and thus increase the concentration of the vapours.

The goal here was to be able to remain as close as possible to the initial concentration of the vapour. Hence, the use of a modified short-path distillation set-up. This combined with FTIR analysis of the distillate it was detected that irrespective of the metal ion in the nitrate salt, the initial distillate was the same – ethanol with small amounts of THT. FTIR proved to be powerful when analyzing treated solutions.

On observation of the actual combustion of the precursor solution combinations the observations in bulk solution could be correlated. Images captured showed an initial blue steak followed by a colour change that is specific to the metal present in the solution, the indication that metal starts burning later in the process. In distillation it is seen that ethanol with small amounts of THT evaporate initially and it known that pure ethanol burns with a blue flame. This further suggests that concentration of sulfur interacting with metal at higher temperature is greater than the starting solution. Solution interactions of precursors were proposed and elucidated.

One of the most crucial steps was to determine the breakdown of THT. As an excess supply of oxygen due to its competing nature with sulfur to combine with metal ions is avoided, it was assumed there might be changes in breakdown as compared to known breakdown path of organosulfur compounds where oxygen is supplied in excess in the form of water vapour. Mass spectroscopic studies confirmed that in the absence of oxygen, negligible amounts of H_2S are produced as a result of the breakdown. Instead, there is a dominance of 5 other sulfur containing fragments. The amount of CS_2 detected is also negligible. Together with the study of high temperature breakdown of metal source, mechanism of gas phase interaction leading to the formation of metal sulfides is suggested here.

In short, possible paths of metal-sulfur solution creation along with systematic approach to the discovery of dissociation and mechanism for reaction in the future have been established.

Future work

As this is just the beginning of the exploration and understanding into creating metal sulfide nanoparticles through the process of combustion, there is much to be discovered and understood. From a precursor solution perspective, the variations that can be used are plentiful. In this work, the focus was to establish the best possible source that can cover the production of a wide range of metal sulfides. To create compounds such as multi-ion sulfides through combustion it is likely the sulfur and metal sources will have to be precisely tailored to the compound being created due to difficulties that are likely to arise when it comes to dissolution in solvent.

Further independent studies through different approaches will be required to confirm the mechanism formation of metal sulfides through the process of combustion. The presence of small amounts of water from the hydrated metal salts could be playing a role in the phase separation seen in this work as THT and water are known to be immiscible. This occurrence needs to be further studied, ideally supplemented by theoretical methods. If different sulfur sources are used in the production, their individual breakdown behaviours in limited oxygen environments need to be studied separately. The discovery of other suitable sulfur sources for combustion synthesis would likely mean their breakdown down at higher temperature proceeds differently to that of tetrahydrothiophene (THT).

As discussed in this work, solid sources of sulfur are less attractive than liquid sources. While the exploration of the use of gaseous source is limited, the prospect of using a gaseous source of sulfur in combustion synthesis is an attractive alternative. Some of the common gaseous sources of sulfur such as H_2S are highly reactive and known to produce metal sulfides on exposure to metal and works using it directly in combustion synthesis are yet to be seen in literature. There are challenges to working with highly combustible and corrosive gases, however it could be an advantage for several reasons. The biggest advantage being, dissolution of the sulfur source with metal source can be disregarded. This opens the possibility to work with many kinds of metal sources without the limitation posed by liquid sources of sulfur.

Bibliography

1.   Di, T.; Xu, Q.; Ho, W.; Tang, H.; Xiang, Q.; Yu, J., Review on Metal Sulphide-based Z-scheme Photocatalysts. *ChemCatChem* **2019,** *11* (5), 1394-1411.

2.   Torres, M. E. S.; Morales, A. R.; Peralta, A. S.; Kroneck, P. M. H., *Transition Metals and Sulfur – A Strong Relationship for Life*. De Gruyter: 2020.

3.   Xu, X.; Liu, W.; Kim, Y.; Cho, J., Nanostructured transition metal sulfides for lithium ion batteries: Progress and challenges. *Nano Today* **2014,** *9* (5), 604-630.

4.   Shi, W.; Lu, B., Nanoscale Kirkendall Effect Synthesis of Echinus-like SnO2@SnS2 Nanospheres as High Performance Anode Material for Lithium Ion Batteries. *Electrochim. Acta* **2014,** *133*, 247-253.

5.   Wu, P.; Du, N.; Zhang, H.; Liu, J.; Chang, L.; Wang, L.; Yang, D.; Jiang, J. Z., Layer-stacked tin disulfide nanorods in silica nanoreactors with improved lithium storage capabilities. *Nanoscale* **2012,** *4* (13), 4002-6.

6.   Wang, Q.; Huang, Y.; Miao, J.; Zhao, Y.; Wang, Y., Synthesis and electrochemical characterizations of Ce doped SnS2 anode materials for rechargeable lithium ion batteries. *Electrochim. Acta* **2013,** *93*, 120-130.

7.   H.Tributsch; J.C.Bennett, Electrochemistry and photochemistry of MoS2 layer crystals. I. *Journal of Electroanalytical Chemistry and Interfacial Electrochemistry* **1977,** *81*, 97-111.

8.   Hinnemann, B.; Moses, P. G.; Bonde, J.; Jørgensen, K. P.; Nielsen, J. H.; Horch, S.; Chorkendorff, I.; Nørskov, J. K., Biomimetic Hydrogen Evolution: MoS2 Nanoparticles as Catalyst for Hydrogen Evolution. *J. Am. Chem. Soc.* **2005,** *127*, 5308–5309.

9.   Li, H.; Tsai, C.; Koh, A. L.; Cai, L.; Contryman, A. W.; Fragapane, A. H.; Zhao, J.; Han, H. S.; Manoharan, H. C.; Abild-Pedersen, F.; Norskov, J. K.; Zheng, X., Activating and optimizing MoS2 basal planes for hydrogen evolution through the formation of strained sulphur vacancies. *Nat Mater* **2016,** *15* (3), 364.

10.   Faber, M. S.; Dziedzic, R.; Lukowski, M. A.; Kaiser, N. S.; Ding, Q.; Jin, S., High-performance electrocatalysis using metallic cobalt pyrite (CoS(2)) micro- and nanostructures. *J. Am. Chem. Soc.* **2014,** *136* (28), 10053-61.

11.   Lee, Y. J.; Park, S.-K., Metal–Organic Framework-Derived Hollow CoSx Nanoarray Coupled with NiFe Layered Double Hydroxides as Efficient Bifunctional Electrocatalyst for Overall Water Splitting. *Small* **2022,** *18*.

12.   Wang, Q.; Ze-YuTian; Cui, W.-J.; Hu, N.; Zhang, S.-M.; Ma, Y.-Y.; Han, Z.-G., Hierarchical flower-like CoS2-MoS2 heterostructure spheres as efficient bifunctional electrocatalyst for overall water splitting. *Int. J. Hydrogen Energy* **2022,** *47* (25).

13. Huang, W.-H.; Li, X.-M.; Yang, X.-F.; Zhang, H.-B.; Wang, F.; Zhang, J., Highly efficient electrocatalysts for overall water splitting: mesoporous CoS/MoS2 with hetero-interfaces. *Chem. Commun.* **2021,** *57*, 4847-4850

14. Khan, Z. R.; Zulfequar, M.; Khan, M. S., Chemical synthesis of CdS nanoparticles and their optical and dielectric studies. *Journal of Materials Science* **2011,** *46* (16), 5412-5416.

15. Kaur, J.; Sharma, M.; Pandey, O. P., Structural and optical studies of undoped and copper doped zinc sulphide nanoparticles for photocatalytic application. *Superlattices Microstruct.* **2015,** *77*, 35-53.

16. Balischewski, C.; Choi, H. S.; Behrens, K.; Beqiraj, A.; Korzdorfer, T.; Gessner, A.; Wedel, A.; Taubert, A., Metal Sulfide Nanoparticle Synthesis with Ionic Liquids - State of the Art and Future Perspectives. *ChemistryOpen* **2021,** *10* (2), 272-295.

17. Joo, J.; Na, H. B.; Yu, T.; Kim, Y. W.; Wu, F.; Zhang, J. Z.; Hyeon, T., Generalized and Facile Synthesis of Semiconducting Metal Sulfide Nanocrystals. *Journal of the American Chemical Society* **2003,** *125*.

18. Lee, S.-M.; Jun, Y.-w.; Cho, S.-N.; Cheon, J., Single-Crystalline Star-Shaped Nanocrystals and Their Evolution: Programming the Geometry of Nano-Building Blocks. *Journal of the American Chemical Society* **2002,** *124*, 11244-11245.

19. *IUPAC. Compendium of Chemical Terminology, 2nd ed. (the "Gold Book"). Compiled by A. D. McNaught and A. Wilkinson. Blackwell Scientific Publications, Oxford (1997). Online version (2019-) created by S. J. Chalk. ISBN 0-9678550-9-8.* .

20. Chin, P. P.; Ding, J.; Yi, J. B.; Liu, B. H., Synthesis of FeS2 and FeS nanoparticles by high-energy mechanical milling and mechanochemical processing. *J. Alloys Compd.* **2005,** *390* (1-2), 255-260.

21. Dutková, E.; Jesús Sayagués, M.; Fabián, M.; Baláž, M.; Achimovičová, M., Mechanochemically synthesized ternary chalcogenide Cu3SbS4 powders in a laboratory and an industrial mill. *Mater. Lett.* **2021,** *291*.

22. Dong, W.; Wang, X.; Li, B.; Wang, L.; Chen, B.; Li, C.; Li, X.; Zhang, T.; Shi, Z., Hydrothermal synthesis and structure evolution of hierarchical cobalt sulfide nanostructures. *Dalton Trans* **2011,** *40* (1), 243-8.

23. Kundu, J.; Khilari, S.; Pradhan, D., Shape-Dependent Photocatalytic Activity of Hydrothermally Synthesized Cadmium Sulfide Nanostructures. *ACS Appl Mater Interfaces* **2017,** *9* (11), 9669-9680.

24. Bolagam, R.; Um, S., Hydrothermal Synthesis of Cobalt Ruthenium Sulfides as Promising Pseudocapacitor Electrode Materials. *Coatings* **2020,** *10* (3).

25. Bilecka, I.; Niederberger, M., Microwave chemistry for inorganic nanomaterials synthesis. *Nanoscale* **2010,** *2*.

26. Teoh, W. Y.; Amal, R.; Mädler, L., Flame spray pyrolysis: An enabling technology for nanoparticles design and fabrication. *Nanoscale* **2010,** *2* (8), 1324-1347.

27. Strobela, R.; Baiker, A.; E.Pratsinis, S., Aerosol flame synthesis of catalysts. *Adv. Powder Technol.* **2006,** *17*, 457-480.

28. Meierhofer, F.; Fritsching, U., Synthesis of Metal Oxide Nanoparticles in Flame Sprays: Review on Process Technology, Modeling, and Diagnostics. *Energy & Fuels* **2021,** *35* (7), 5495-5537.

29.   Nunes, D.; Pimentel, A.; Santos, L.; Barquinha, P.; Pereira, L.; Fortunato, E.; Martins, R., Synthesis, design, and morphology of metal oxide nanostructures. In *Metal Oxide Nanostructures*, 2019; pp 21-57.

30.   Athanassiou, E. K.; Grass, R. N.; Stark, W. J., One-step large scale gas phase synthesis of Mn 2+ doped ZnS nanoparticles in reducing flames. *Nanotechnology* **2010,** *21* (21), 215603.

31.   Johannessen, T.; Koutsopoulos, S., One-Step Flame Synthesis of an Active Pt/TiO2 Catalyst for SO2 Oxidation—A Possible Alternative to Traditional Methods for Parallel Screening. *J. Catal.* **2002,** *205* (2), 404-408.

32.   Strobel, R.; Krumeich, F.; Stark, W. J.; Pratsinis, S. E.; Baiker, A., Flame spray synthesis of Pd/Al2O3 catalysts and their behavior in enantioselective hydrogenation. *J. Catal.* **2004,** *222* (2), 307-314.

33.   Strobel, R.; Stark, W. J.; Mädler, L.; Pratsinis, S. E.; Baiker, A., Flame-made platinum/alumina: structural properties and catalytic behaviour in enantioselective hydrogenation. *J. Catal.* **2003,** *213* (2), 296-304.

34.   Wang, Y.; Wu, Y.; Shirazi-Amin, A.; Kerns, P.; Fee, J.; He, J.; Jin, L.; Maric, R.; Suib, S. L., Direct Construction of Mesoporous Metal Sulfides via Reactive Spray Deposition Technology. *ACS Applied Energy Materials* **2019,** *2* (4), 2370-2374.

35.   Rosebrock, C. D.; Riefler, N.; Wriedt, T.; Mädler, L.; Tse, S. D., Disruptive burning of precursor/solvent droplets in flame-spray synthesis of nanoparticles. *AIChE Journal* **2013,** *59* (12), 4553-4566.

36.   Godsave, G., Combustion of Droplets in a Fuel Spray. *Nature* **1949,** *164*, 708–709.

37.   Rosebrock, C. D.; Wriedt, T.; Mädler, L.; Wegner, K., The role of microexplosions in flame spray synthesis for homogeneous nanopowders from low-cost metal precursors. *AIChE Journal* **2016,** *62* (2), 381-391.

38.   A. Ismael, M.; Heikal, M.; A. Aziz, A.; Crua, C.; El-Adawy, M.; Nissar, Z.; Baharom, M.; Zainal A, E.; Firmansyah, Investigation of Puffing and Micro-Explosion of Water-in-Diesel Emulsion Spray Using Shadow Imaging. *Energies* **2018,** *11* (9).

39.   Watanabe, H.; Okazaki, K., Visualization of secondary atomization in emulsified-fuel spray flow by shadow imaging. *Proceedings of the Combustion Institute* **2013,** *34* (1), 1651-1658.

40.   M, F.; T, I.; Y, M., Observation of microexplosion in light oil-water emulsion spray flame. . *Proceedings of the Japanese Society of Mechanical Engineers, Part B* **2003,** *69*.

41.   Y, M.; M, M., In situ observation of microexplosion of emulsion droplets in spray flames. . *Atomization Sprays* **2001,** *11*.

42.   Stodt, M. F. B.; Groeneveld, Jan D.; Mädler, L.; Kiefer, J.; Fritsching, U., Microexplosions of multicomponent drops in spray flames. *Combust. Flame* **2022,** *240*.

43.   Li, H.; Pokhrel, S.; Schowalter, M.; Rosenauer, A.; Kiefer, J.; Mädler, L., The gas-phase formation of tin dioxide nanoparticles in single droplet combustion and flame spray pyrolysis. *Combust. Flame* **2020,** *215*, 389-400.

44.   Li, S.; Li, J.; Yi, J.; Shan, Z., Cleaner beam house processes trial on cattle sofa leather. *Journal of Cleaner Production* **2010,** *18* (5), 471-477.

45.   Malghan, S. G., Role of sodium sulfide in the flotation of oxidized copper, lead, and zinc ores. *Mining, Metallurgy & Exploration* **1986,** *3*, 158–163.

46.   Meyer, B., *Sulfur, Energy, and Environment*. Elsevier: 1977.

47.   Dinegar, R. H.; Smellie, R. H.; Mer, V. K. L., Kinetics of the Acid Decomposition of Sodium Thiosulfate in Dilute Solutions. *Journal of the American Chemical Society* **1951,** *73*.

48.   Schroeder, D. C., Thioureas. *Chem. Rev.* **1955**.

49.   Mertschenk, B.; Knott, A.; Bauer, W., Thiourea and Thiourea Derivatives. *Ullmann's Encyclopedia of Industrial Chemistry* **2000**.

50.   Suresh, S., Studies on the dielectric properties of CdS nanoparticles. *Appl. Nanosci.* **2013,** *4* (3), 325-329.

51.   Fotouhi, L.; Rezaei, M., Electrochemical synthesis of copper sulfide nanoparticles. *Microchim. Acta* **2009,** *167* (3-4), 247-251.

52.   Bhattacharya, S.; Chakravorty, D., Electrical and magnetic properties of cold compacted iron-doped zinc sulfide nanoparticles synthesized by wet chemical method. *Chem. Phys. Lett.* **2007,** *444* (4-6), 319-323.

53.   Fazli, Y.; Mahdi Pourmortazavi, S.; Kohsari, I.; Sadeghpur, M., Electrochemical synthesis and structure characterization of nickel sulfide nanoparticles. *Mater. Sci. Semicond. Process.* **2014,** *27*, 362-367.

54.   Upadhyay, R. K.; Sharma, M.; Singh, D. K.; Amritphale, S. S.; Chandra, N., Photo degradation of synthetic dyes using cadmium sulfide nanoparticles synthesized in the presence of different capping agents. *Separation and Purification Technology* **2012,** *88*, 39-45.

55.   Sun, W.; Zhong, J.; Zhang, B.; Jiao, K., Application of cadmium sulfide nanoparticles as oligonucleotide labels for the electrochemical detection of NOS terminator gene sequences. *Anal Bioanal Chem* **2007,** *389* (7-8), 2179-84.

56.   Seoudi, R.; Shabaka, A. A.; Kamal, M.; Abdelrazek, E. M.; Eisa, W., Dependence of spectroscopic and electrical properties on the size of cadmium sulfide nanoparticles. *Physica E: Low-dimensional Systems and Nanostructures* **2012,** *45*, 47-55.

57.   Pathak, C. S.; Mishra, D. D.; Agarwala, V.; Mandal, M. K., Blue light emission from barium doped zinc sulfide nanoparticles. *Ceramics International* **2012,** *38* (7), 5497-5500.

58.   Mishra, S. K.; Srivastava, R. K.; Prakash, S. G.; Yadav, R. S.; Panday, A. C., Structural, optical and photoconductivity characteristics of manganese doped cadmium sulfide nanoparticles synthesized by co-precipitation method. *Journal of Alloys and Compounds* **2012,** *513*, 118-124.

59.   Kole, A. K.; Kumbhakar, P., Effect of manganese doping on the photoluminescence characteristics of chemically synthesized zinc sulfide nanoparticles. *Applied Nanoscience* **2011,** *2* (1), 15-23.

60.   Sun, W.; Zhong, J.; Qin, P.; Jiao, K., Electrochemical biosensor for the detection of cauliflower mosaic virus 35 S gene sequences using lead sulfide nanoparticles as oligonucleotide labels. *Anal. Biochem.* **2008,** *377* (2), 115-9.

61.   Mullaugh, K. M.; Luther, G. W., 3rd, Spectroscopic determination of the size of cadmium sulfide nanoparticles formed under environmentally relevant conditions. *J Environ Monit* **2010,** *12* (4), 890-7.

62.   Fakhri, A.; Pourmand, M.; Khakpour, R.; Behrouz, S., Structural, optical, photoluminescence and antibacterial properties of copper-doped silver sulfide nanoparticles. *J. Photochem. Photobiol. B.* **2015,** *149*, 78-83.

63.   Abdullah, O. G.; Saleem, S. A., Effect of Copper Sulfide Nanoparticles on the Optical and Electrical Behavior of Poly(vinyl alcohol) Films. *Journal of Electronic Materials* **2016,** *45* (11), 5910-5920.

64.   Iwasaki, K.; Torimoto, T.; Shibayama, T.; Takahashi, H.; Ohtani, B., Preparation and Characterization of Water-Soluble Jingle-Bell-Shaped Silica-Coated Cadmium Sulfide Nanoparticles. *J. Phys. Chem. B* **2004,** *108*, 11946-11952.

65.   Albani, D.; Shahrokhi, M.; Chen, Z.; Mitchell, S.; Hauert, R.; Lopez, N.; Perez-Ramirez, J., Selective ensembles in supported palladium sulfide nanoparticles for alkyne semi-hydrogenation. *Nat Commun* **2018,** *9* (1), 2634.

66.   Sadovnikov, S. I.; Kuznetsova, Y. V.; Rempel, A. A., Ag2S silver sulfide nanoparticles and colloidal solutions: Synthesis and properties. *Nano-Structures & Nano-Objects* **2016,** *7*, 81-91.

67.   Li, N.; Sun, Q.; Yu, Z.; Gao, X.; Pan, W.; Wan, X.; Tang, B., Nuclear-Targeted Photothermal Therapy Prevents Cancer Recurrence with Near-Infrared Triggered Copper Sulfide Nanoparticles. *ACS Nano* **2018,** *12* (6), 5197-5206.

68.   Stroyuk, A. L.; Raevskaya, A. E.; Korzhak, A. V.; Kuchmii, S. Y., Zinc sulfide nanoparticles: Spectral properties and photocatalytic activity in metals reduction reactions. *Journal of Nanoparticle Research* **2006,** *9* (6), 1027-1039.

69.   Lau, B. L. T.; Hsu-Kim, H., Precipitation and Growth of Zinc Sulfide Nanoparticles in the Presence of Thiol-Containing Natural Organic Ligands. *Environ. Sci. Technol.* **2008,** *42*, 7236–7241.

70.   Green, M.; Taylor, R.; Wakefield, G., The synthesis of luminescent adenosine triphosphate passivated cadmium sulfide nanoparticles. *J. Mater. Chem.* **2003,** *13* (8), 1859.

71.   Kryukov, A. I.; Kuchmii, S. Y.; Korzhak, A. V.; Zinchuk, N. N.; Raevskaya, A. E.; Stroyuk, a. A. L., Quantum-sized effects and the Nature of the Primary Photoprocesses in Copper(I) and Copper(II) sulfide nanoparticles. *Theoretical and Experimental Chemistry* **1999,** *35*.

72.   Shahi, A. K.; Pandey, B. K.; Swarnkar, R. K.; Gopal, R., Surfactant assisted surface studies of zinc sulfide nanoparticles. *Applied Surface Science* **2011,** *257* (23), 9846-9851.

73.   Lakowicz, J. R.; Gryczynski, I.; Piszczek, G.; Murphy, C. J., Emission Spectral Properties of Cadmium Sulfide Nanoparticles with Multiphoton Excitation. *J. Phys. Chem. B* **2002,** *106*, 5365-5370.

74.   Lakowicz, J. R.; Gryczynski, I.; Gryczynski, Z.; Nowaczyk, K.; Murphy, C. J., Time-resolved spectral observations of cadmium-enriched cadmium sulfide nanoparticles and the effects of DNA oligomer binding. *Anal Biochem* **2000,** *280* (1), 128-36.

75.   Shi, X.; Sun, K.; Balogh, L. P.; Baker, J. R., Synthesis, characterization, and manipulation of dendrimer-stabilized iron sulfide nanoparticles. *Nanotechnology* **2006,** *17* (18), 4554-4560.

76.   Xiong, Z.; He, F.; Zhao, D.; Barnett, M. O., Immobilization of mercury in sediment using stabilized iron sulfide nanoparticles. *Water Res* **2009,** *43* (20), 5171-9.

77.   Morris, T.; Copeland, H.; Szulczewski, G., Synthesis and Characterization of Gold Sulfide Nanoparticles. *Langmuir* **2002,** *18*, 535-539.

78.   Mercy, A.; Sakthi Murugesan, K.; Milton Boaz, B.; Jesper Anandhi, A.; Kanagadurai, R., Synthesis and structural and optical characterization of Mn2+ doped cadmium sulphide

nanoparticles stabilized in DETA matrix. *Journal of Alloys and Compounds* **2013,** *554*, 189-194.

79.   Murugadoss, G.; Ramasamy, V., Synthesis, effect of capping agents and optical properties of manganese-doped zinc sulphide nanoparticles. *Luminescence* **2013,** *28* (1), 69-75.

80.   Pathania, D.; Sarita; Rathore, B. S., Synthesis, characterization and photocatalytic application of Bovine Serum Albumin capped cadmium sulphide nanopartilces. *Chalcogenide Letters* **2011,** *8,* , 396 - 404.

81.   Pathak, C. S.; Mandal, M. K., Yellow light emission from Mn2+ doped ZnS nanoparticles. *Optoelectron. Adv. Mater. Rapid Commun.* **2011,** *5*, 211-214.

82.   Pathak, C. S.; Mishra, D. D.; Agarawala, V.; Mandal, M. K., Mechanochemical synthesis, characterization and optical properties of zinc sulphide nanoparticles. *Indian Journal of Physics* **2012,** *86* (9), 777-781.

83.   Mercy, A.; Selvaraj, R. S.; Boaz, B. M.; Anandhi, A.; Kanagadurai, a. R., Synthesis, structural and optical characterisation of cadmium sulphide nanoparticles. **2013,** *51*, 448-452.

84.   Khosravi, A. A.; Kundu, M.; Kuruvilla, B. A.; Shekhawat, G. S.; Gupta, R. P.; Sharma, A. K.; Vyas, P. D.; Kulkarni, S. K., Manganese doped zinc sulphide nanoparticles by aqueous method. *Applied Physics Letters* **1995,** *67* (17), 2506-2508.

85.   Gayou, V. L.; Salazar-Hernández, B.; Macuil, R. D.; Zavala, G.; Santiago, P.; Oliva, A. I., Structural studies of ZnS nanoparticles by high resolution transmission electron microscopy. *Journal of Nano Research* **2010,** *9*, 125-132.

86.   Zhu, N.; Zhang, A.; Wang, Q.; He, P.; Fang, Y., Lead Sulfide Nanoparticle as Oligonucleotides Labels for Electrochemical Stripping Detection of DNA Hybridization. *Electroanalysis* **2004,** *16* (7), 577-582.

87.   Wu, S. Y.-H.; Tseng, C.-L.; Lin, F.-H., A newly developed Fe-doped calcium sulfide nanoparticles with magnetic property for cancer hyperthermia. *J. Nanopart. Res.* **2009,** *12* (4), 1173-1185.

88.   Gao, W.; Sun, Y.; Cai, M.; Zhao, Y.; Cao, W.; Liu, Z.; Cui, G.; Tang, B., Copper sulfide nanoparticles as a photothermal switch for TRPV1 signaling to attenuate atherosclerosis. *Nat Commun* **2018,** *9* (1), 231.

89.   Sun, B.; Yi, G.; Chen, D.; Zhou, Y.; Cheng, J., Synthesis and characterization of strongly fluorescent europium-doped calcium sulfide nanoparticles. *J. Mater. Chem.* **2002,** *12* (4), 1194-1198.

90.   Rekha, S.; Martinez, A. I.; Safeera, T. A.; Anila, E. I., Enhanced luminescence of triethanolamine capped calcium sulfide nanoparticles synthesized using wet chemical method. *Journal of Luminescence* **2017,** *190*, 94-99.

91.   Lee, S. M.; Ko, Y. N.; Choi, S. H.; Kim, J. H.; Kang, Y. C., Capacitive properties of reduced graphene oxide microspheres with uniformly dispersed nickel sulfide nanocrystals prepared by spray pyrolysis. *Electrochim. Acta* **2015,** *167*, 287-293.

92.   Krishnamoorthy, K.; Veerasubramani, G. K.; Kim, S. J., Hydrothermal synthesis, characterization and electrochemical properties of cobalt sulfide nanoparticles. *Mater. Sci. Semicond. Process.* **2015,** *40*, 781-786.

93.   Dunne, P. W.; Starkey, C. L.; Gimeno-Fabra, M.; Lester, E. H., The rapid size- and shape-controlled continuous hydrothermal synthesis of metal sulphide nanomaterials. *Nanoscale* **2014,** *6* (4), 2406-18.

94.   Lee, D. G.; Lee, N. H.; Oh, H. J.; Jung, S. C.; Hwang, J. S.; Lee, W. J.; Kim, S. J., Formation and characterization of nanoparticles based CuInS2 absorbing layer for solar cell. *J Nanosci Nanotechnol* **2011,** *11* (2), 1434-7.

95.   Zhang, X.; Wang, H.; Wang, G., Cobalt sulfide nanoparticles anchored in three-dimensional carbon nanosheet networks for lithium and sodium ion batteries with enhanced electrochemical performance. *J Colloid Interface Sci* **2017,** *492*, 41-50.

96.   Mir, F. A.; Chattarjee, I.; Dar, A. A.; Asokan, K.; Bhat, G. M., Preparation and characterizations of cadmium sulfide nanoparticles. *Optik* **2015,** *126* (11-12), 1240-1244.

97.   Rempel, A. A.; Kozhevnikova, N. S.; Van den Berghe, S.; Van Renterghem, W.; Leenaers, A. J. G., Self-organization of cadmium sulfide nanoparticles on the macroscopic scale. *physica status solidi (b)* **2005,** *242* (7), R61-R63.

98.   Krishnamoorthy, K.; Pazhamalai, P.; Kim, S. J., Ruthenium sulfide nanoparticles as a new pseudocapacitive material for supercapacitor. *Electrochim. Acta* **2017,** *227*, 85-94.

99.   Han, S.; Kong, M.; Guo, Y.; Wang, M., Synthesis of copper indium sulfide nanoparticles by solvothermal method. *Mater. Lett.* **2009,** *63* (13-14), 1192-1194.

100.   Singh, A.; Manivannan, R.; Noyel Victoria, S., Simple one-pot sonochemical synthesis of copper sulphide nanoparticles for solar cell applications. *Arabian Journal of Chemistry* **2019,** *12* (8), 2439-2447.

101.   Patel, J. D.; Mighri, F.; Ajji, A.; Chaudhuri, T. K., Morphology and size control of lead sulphide nanoparticles produced using methanolic lead acetate trihydrate–thiourea complex via different precipitation techniques. *Materials Chemistry and Physics* **2012,** *132* (2-3), 747-755.

102.   Neelakandeswari, N.; Sangami, G.; Dharmaraj, N.; Taek, N. K.; Kim, H. Y., Spectroscopic investigations on the photodegradation of toluidine blue dye using cadmium sulphide nanoparticles prepared by a novel method. *Spectrochim Acta A Mol Biomol Spectrosc* **2011,** *78* (5), 1592-8.

103.   Navaneethan, M.; Nisha, K. D.; Ponnusamy, S.; Muthamizhchelvan, C., Optical and surface morphological properties of triethylamine passivated lead sulphide nanoparticles. *Materials Chemistry and Physics* **2009,** *117* (2-3), 443-447.

104.   Jayalakshmi, M.; Rao, M. M., Synthesis of zinc sulphide nanoparticles by thiourea hydrolysis and their characterization for electrochemical capacitor applications. *Journal of Power Sources* **2006,** *157* (1), 624-629.

105.   Pattabi, M.; Uchil, J., Synthesis of Cadmium Sulphide nanoparticles. **2000,** *63*, 309-314.

106.   Krishnamoorthy, K.; Veerasubramani, G. K.; Radhakrishnan, S.; Kim, S. J., Preparation of Copper Sulfide Nanoparticles by Sonochemical Method and Study on Their Electrochemical Properties. *J. Nanosci. Nanotechnol.* **2015,** *15*, 4409–4413.

107.   Tukhtaev, R. K.; Boldyrev, V. V.; Gavrilov, A. I.; Larionov, S. V.; Myachina, L. I.; Savel'eva, Z. A., Metal Sulfide Synthesis by Self-Propagating Combustion of Sulfur-Containing Complexes. *Inorganic Materials* **2002,** *38*, 985–991.

108.   Mao, L.; Wang, Y.; Zhong, Y.; Ning, J.; Hu, Y., Microwave-assisted deposition of metal sulfide/oxide nanocrystals onto a 3D hierarchical flower-like TiO2 nanostructure with improved photocatalytic activity. *Journal of Materials Chemistry A* **2013,** *1* (28), 8101.

109.   Guo, Y.; Zhang, J.; Yang, L.; Wang, H.; Wang, F.; Zheng, Z., Syntheses of amorphous and crystalline cupric sulfide nanoparticles and study on the specific activities on different cells. *Chem Commun (Camb)* **2010,** *46* (20), 3493-5.

110.   Khiew, P. S.; Radiman, S.; Huang, N. M.; Ahamd, M. S., Synthesis and characterization of copper sulfide nanoparticles in hexagonal phase lyotropic liquid crystal. *Journal of Crystal Growth* **2004,** *268* (1-2), 227-237.

111.   Liu, L.; Wang, L.; Yin, H.; Li, Y.; He, X., The Preparation and Application of Bismuth (III) Ion-Selective Electrode Based on Nanoparticles of Bismuth Sulfide. *Anal. Lett.* **2006,** *39* (5), 879-890.

112.   Lu, H.-Y.; Chu, S.-Y.; Tan, S.-S., The characteristics of low-temperature-synthesized ZnS and ZnO nanoparticles. *J. Cryst. Growth* **2004,** *269* (2-4), 385-391.

113.   Mokhtari, P.; Ghaedi, M.; Dashtian, K.; Rahimi, M. R.; Purkait, M. K., Removal of methyl orange by copper sulfide nanoparticles loaded activated carbon: Kinetic and isotherm investigation. *Journal of Molecular Liquids* **2016,** *219*, 299-305.

114.   Salavati-Niasari, M.; Banaiean-Monfared, G.; Emadi, H.; Enhessari, M., Synthesis and characterization of nickel sulfide nanoparticles via cyclic microwave radiation. *C. R. Chimie* **2013,** *16* (10), 929-936.

115.   Ghaedi, M.; Pakniat, M.; Mahmoudi, Z.; Hajati, S.; Sahraei, R.; Daneshfar, A., Synthesis of nickel sulfide nanoparticles loaded on activated carbon as a novel adsorbent for the competitive removal of Methylene blue and Safranin-O. *Spectrochim Acta A Mol Biomol Spectrosc* **2014,** *123*, 402-9.

116.   Dhas, N. A.; Zaban, A.; Gedanken, A., Surface Synthesis of Zinc Sulfide Nanoparticles on Silica Microspheres: Sonochemical Preparation,Characterization, and Optical Properties. *Chem. Mater.* **1999,** *11*, 806-813.

117.   Son, D.; Jung, D.-R.; Kim, J.; Moon, T.; Kim, C.; Park, B., Synthesis and photoluminescence of Mn-doped zinc sulfide nanoparticles. *Appl. Phys. Lett.* **2007,** *90* (10), 101910.

118.   Wanga, L. P.; Hong, G. Y., A new preparation of zinc sulfide nanoparticles by solid-state method at low temperature. *Materials Research Bulletin* **2000,** *35*, 695–701.

119.   Wang, H.; Zhang, J.-R.; Zhao, X.-N.; Xu, S.; Zhu, J.-J., Preparation of copper monosulfide and nickel monosulfide nanoparticles by sonochemical method. *Mater. Lett.* **2002,** *55*, 253–258.

120.   Darouie, M.; Afshar, S.; Zare, K.; Monajjemi, M., Investigation of different factors towards synthesis of CuS spherical nanoparticles. *J. Exp. Nanosci.* **2013,** *8* (4), 451-461.

121.   Nguyen, M.; Tran, P. D.; Pramana, S. S.; Lee, R. L.; Batabyal, S. K.; Mathews, N.; Wong, L. H.; Graetze, M., In situ photo-assisted deposition of MoS2 electrocatalyst onto zinc cadmium sulphide nanoparticle surfaces to construct an efficient photocatalyst for hydrogen generation. *Nanoscale* **2013,** *5*, 1479–1482.

122.   Li, Y.; Lu, W.; Huang, Q.; Huang, M.; Li, C.; Chen, W., Copper sulfide nanoparticles for photothermal ablation of tumor cells. *Nanomedicine* **2010,** *5(8)*, 1161–1171.

123.   Thongtem, T.; Phuruangrat, A.; Thongtem, S., Characterization of copper sulfide nanostructured spheres and nanotubessynthesized by microwave-assisted solvothermal method. *Materials Letters* **2010,** *64* (2), 136-139.

124.   Kravchyk, K. V.; Widmer, R.; Erni, R.; Dubey, R. J.; Krumeich, F.; Kovalenko, M. V.; Bodnarchuk, M. I., Copper sulfide nanoparticles as high-performance cathode materials for Mg-ion batteries. *Sci Rep* **2019,** *9* (1), 7988.

125.   Bhattacharya, R.; Das, T. K.; Saha, S., Synthesis and characterization of CdS nanoparticles. *Journal of Materials Science: Materials in Electronics* **2011,** *22* (12), 1761-1765.

126.   Saldanha, P. L.; Brescia, R.; Prato, M.; Li, H.; Povia, M.; Manna, L.; Lesnyak, V., Generalized One-Pot Synthesis of Copper Sulfide, Selenide-Sulfide, and Telluride-Sulfide Nanoparticles. *Chemistry of Materials* **2014,** *26* (3), 1442-1449.

127.   Mukherjee, P.; Shade, C. M.; Yingling, A. M.; Lamont, D. N.; Waldeck, D. H.; Petoud, S., Lanthanide sensitization in II-VI semiconductor materials: a case study with terbium(III) and europium(III) in zinc sulfide nanoparticles. *J Phys Chem A* **2011,** *115* (16), 4031-41.

128.   Karthikeyan, R.; Thangaraju, D.; Prakash, N.; Hayakawa, Y., Single-step synthesis and catalytic activity of structure-controlled nickel sulfide nanoparticles. *CrystEngComm* **2015,** *17* (29), 5431-5439.

129.   Ahmad, R.; Azimi, H.; Distaso, M.; Brabec, C. J.; Peukert, W., Facile synthesis and post-processing of eco-friendly, highly conductive copper zinc tin sulphide nanoparticles. *J Nanopart Res* **2013,** *15:1886.*

130.   Kremser, G.; Rath, T.; Kunert, B.; Edler, M.; Fritz-Popovski, G.; Resel, R.; Letofsky-Papst, I.; Grogger, W.; Trimmel, G., Structural characterisation of alkyl amine-capped zinc sulphide nanoparticles. *J Colloid Interface Sci* **2012,** *369* (1), 154-9.

131.   Ghezelbash, A.; Korgel, B. A., Nickel Sulfide and Copper Sulfide Nanocrystal Synthesis and Polymorphism. *Langmuir* **2005,** *21*, 9451-9456.

132.   Fei, L.; Jiang, Y.; Xu, Y.; Chen, G.; Li, Y.; Xu, X.; Deng, S.; Luo, H., A novel solvent-free thermal reaction of ferrocene and sulfur for one-step synthesis of iron sulfide and carbon nanocomposites and their electrochemical performance. *J. Power Sources* **2014,** *265*, 1-5.

133.   Tu, W.; Denizot, B., Synthesis of small-sized rhenium sulfide colloidal nanoparticles. *J Colloid Interface Sci* **2007,** *310* (1), 167-70.

134.   Yin, Y.; Xu, X.; Ge, X.; Xia, C.; Zhang, Z., Synthesis of cadmium sulfide nanoparticles in situ using g-radiation. *Chem. Commun.* **1998**.

135.   Zhang, Y. C.; Qiao, T.; Ya Hu, X., A simple hydrothermal route to nanocrystalline CuS. *J. Cryst. Growth* **2004,** *268* (1-2), 64-70.

136.   Choi, S.-H.; An, K.; Kim, E.-G.; Yu, J. H.; Kim, J. H.; Hyeon, T., Simple and Generalized Synthesis of Semiconducting Metal Sulfide Nanocrystals. *Adv. Funct. Mater.* **2009,** *19* (10), 1645-1649.

137.   Jung, J.; Kim, M. A.; Cho, J. H.; Lee, S. J.; Yang, I.; Cho, J.; Kim, S. K.; Lee, C.; Park, J. K., Europium-doped gadolinium sulfide nanoparticles as a dual-mode imaging agent for T1-weighted MR and photoluminescence imaging. *Biomaterials* **2012,** *33* (24), 5865-74.

138.   Li, Q.; Hu, X.; Bai, Y.; Alattar, M.; Ma, D.; Cao, Y.; Hao, Y.; Wang, L.; Jiang, C., The oxidative damage and inflammatory response induced by lead sulfide nanoparticles in rat lung. *Food Chem Toxicol* **2013,** *60*, 213-7.

139.   Leo´n-Vela´zquez, M. S.; Irizarry, R.; Castro-Rosario, M. E., Nucleation and Growth of Silver Sulfide Nanoparticles. *J. Phys. Chem. C* **2010,** *114*, 5839–5849.

140.   Chen, J.; Li, Y.; Wang, Y.; Yun, J.; Cao, D., Preparation and characterization of zinc sulfide nanoparticles under high-gravity environment. *Mater. Res. Bull.* **2004,** *39* (2), 185-194.

141.   Let, A. L.; Mainwaring, D. E.; Rix, C. J.; Murugaraj, P., Thio sol–gel synthesis of titanium disulfide thin films and nanoparticles using titanium(IV) alkoxide precursors. *Journal of Physics and Chemistry of Solids* **2007,** *68* (7), 1428-1435.

142.   Jung, Y. K.; Kim, J. I.; Lee, J.-K., Thermal Decomposition Mechanism of Single-Molecule Precursors Forming Metal Sulfide Nanoparticles. *J. Am. Chem. Soc.* **2010,** *132*, 178–184.

143.   Liu, S.; Zhang, H.; Swihart, M. T., Spray pyrolysis synthesis of ZnS nanoparticles from a single-source precursor. *Nanotechnology* **2009,** *20* (23), 235603.

144.   Armelao, L.; Camozzo, D.; Gross, S.; Tondello, E., Synthesis of copper sulphide nanoparticles in carboxylic acids as solvent. *J Nanosci Nanotechnol* **2006,** *6* (2), 401-8.

145.   Athanassiou, E. K.; Grass, R. N.; Stark, W. J., One-step large scale gas phase synthesis of Mn 2 + doped ZnS nanoparticles in reducing flames. *Nanotechnology* **2010,** *21* (21), 215603.

146.   Anand, K. V.; Chinnu, M. K.; Kumar, R. M.; Mohan, R.; Jayavel, R., Formation of zinc sulfide nanoparticles in HMTA matrix. *Applied Surface Science* **2009,** *255* (21), 8879-8882.

147.   Huang, Y.; Lai, Y.; Shi, S.; Hao, S.; Wei, J.; Chen, X., Copper sulfide nanoparticles with phospholipid-PEG coating for in vivo near-infrared photothermal cancer therapy. *Chem Asian J* **2015,** *10* (2), 370-6.

148.   Balakrishnan, A.; Groeneveld, J. D.; Pokhrel, S.; Madler, L., Metal Sulfide Nanoparticles: Precursor Chemistry. *Chemistry—A European Journal* **2021,** *27* (21), 6390-6406.

149.   Riefler, N.; Wriedt, T.; Fritsching, U., Impedance characterization of a coupled piezo-tube-fluid system for micro droplet generation. *Journal of Fluids and Structures* **2019,** *88*, 185-197.

150.   Mittemeijer, E. J., *Fundamentals of Materials Science*. Springer.

151.   Han Zhang; Jie Tang; Qi Zhang; Gongpu Zhao; Guang Yang; Jian Zhang; Otto Zhou; Qin, L.-C., Field Emission of Electrons from Single LaB6 Nanowires. *Adv. Mater.* **2006,** *18*.

152.   Nafari, A.; Karlen, D.; Rusu, C.; Svensson, K.; Olin, H.; Enoksson, P., MEMS Sensor for In Situ TEM Atomic Force Microscopy. *Journal of Microelectromechanical Systems* **2008,** *17* (2), 328-333.

153.   Joseph I. Goldstein; Dale E. Newbury; Joseph R. Michael; Nicholas W. M. Ritchie; Scott, J. H. J.; Joy, D. C., *Electron Beam—Specimen Interactions: Interaction Volume*. 2018.

154.   Davisson, C.; Germer, L. H., The Scattering of Electron by Single Crystal Nickel. *Nature* **1927,** *119*.

155.   Williams, D. B.; Carter, C. B., *Transmission Electron Microscopy*. Springer

156. Krüss, G., Einige Beobachtungen über die höheren Sauerstoffverbindungen des Kupfers. *Berichte der deutschen chemischen Gesellschaft* **1884,** *17* (2), 2593-2597.

157. Arslan, E. Metal Acetylacetonates and Their Properties. Rutgers, The State University of new Jersey 2019.

158. Meierhofer, F.; Li, H.; Gockeln, M.; Kun, R.; Grieb, T.; Rosenauer, A.; Fritsching, U.; Kiefer, J.; Birkenstock, J.; Madler, L.; Pokhrel, S., Screening Precursor-Solvent Combinations for Li4Ti5O12 Energy Storage Material Using Flame Spray Pyrolysis. *ACS Appl Mater Interfaces* **2017,** *9* (43), 37760-37777.

159. Nebaba, S.; Zavyalov, D.; Pak, A., Patterns Detection in SAED Images of Transmission Electron Microscopy. *CEUR Workshop Proceedings* **2020**.

160. Fehnel, E. A.; Carmack, M., The Ultraviolet Absorption Spectra of Organic Sulfur Compounds. I. Compounds Containing the Sulfide Function. *Jornal of the American Chemical Society* **1949,** *71*, 84-93.

161. Fehnel, E. A.; Carmack, M., The Ultraviolet Absorption Spectra of Organic Sulfur Compounds. II. Compounds Containing the Sulfide Function. *Journal of the American Chemical Society* **1949,** *71*, 231-237.

162. Guo, W.; Kinghorn, A. B.; Zhang, Y.; Li, Q.; Poonam, A. D.; Tanner, J. A.; Shum, H. C., Non-associative phase separation in an evaporating droplet as a model for prebiotic compartmentalization. *Nat Commun* **2021,** *12* (1), 3194.

163. Goebbert, D. J.; Garand, E.; Wende, T.; Bergmann, R.; Meijer, G., Infrared Spectroscopy of the Microhydrated Nitrate Ions NO3-(H2O)1-6 *J. Phys. Chem. A* **2009,** *113*.

164. Bezverkhyy, I.; Bouguessa, K.; Geantet, C.; Vrinat, M., Adsorption of tetrahydrothiophene on faujasite type zeolites: Breakthrough curves and FTIR spectroscopy study. *Applied Catalysis B: Environmental* **2006,** *62*, 299-305.

165. Log, T.; Moi, A. L., Ethanol and Methanol Burn Risks in the Home Environment. *Int J Environ Res Public Health* **2018,** *15* (11).

166. Clark, P. D.; Dowling, N. I.; Lesage, K. L.; Hyne, J. B., Chemistry of organosulphur compound types occurring in heavy oil sands: 5. Reaction of thiophene and tetrahydrothiophene with aqueous Group VIIIB metal species at high temperature. *Fuel* **1987,** *66*.

167. Bubenhofer, S. B.; Schumacher, C. M.; Koehler, F. M.; Luechinger, N. A.; Grass, R. N.; Stark, W. J., Large-Scale Synthesis of PbS–TiO2 Heterojunction Nanoparticles in a Single Step for Solar Cell Application. *J. Phys. Chem. C* **2012,** *116* (30), 16264-16270.

168. Xia, D.; Tian, Y.; Zhu, G.; Xiang, Y.; Luo, L.; Huang, T. T.-S., Theoretical and Experimental Studies on the Thermal Cracking of Tetrahydrothiophene. *Energy Fuels* **2007,** *21*.

169. Clark, P. D.; Hyne, J. B.; Tyrer, J. D., Chemistry of organosulphur compound types occurring in heavy oil sands:: 1. High temperature hydrolysis and thermolysis of tetrahydrothiophene in relation to steam stimulation processes. *Fuel* **1983,** *62*.

170. Lin, R.; Chen, K.; Miao, M.; Zhang, L.; Wang, X.; Jiang, Y.; Zhang, J.; Wang, Y.; Pan, H., Reaction Mechanism of H2S Generation during Tetrahydrothiophene Aquathermolysis Reaction. *Energy & Fuels* **2020,** *34* (3), 2781-2789.

171. Blander, M.; Katz, J., Bubble nucleation in liquids. *AIChE Journal* **1975,** *21*, 833-848.

List of Figures

List of Tables

List of Publications

A Balakrishnan, J D Groeneveld, S Pokhrel, L Madler, Metal Sulfide Nanoparticles: Precursor Chemistry, Chemistry – A European Journal, 27, p. 6390 – 6406, 2021

A Balakrishnan, J D Groeneveld, S Pokhrel, L Madler, Single Droplet Combustion: Proof-of-Principle for ZnS Formation, Project Repository Journal, 6, p. 90-93, 2020

Conference presentation

A Balakrishnan, J D Groeneveld, S Pokhrel, L Madler, Gas-phase synthesis of metal sulphide nanoparticles, 4th International Symposium Gas-Phase Synthesis of Functional Nanomaterials: Fundamental Understanding, Modeling and Simulation, Diagnostics, Scale-up and Application.

In this dissertation the select combustion results from Jan Derk Groeneveld, PhD student (2019) also working in the ERC project ReSuNiCo were added and unpublished images acquired by JDG are acknowledged where used. Specifically, precursor solutions were passed on to JDG who combusted them using the in-house built single droplet generator and collected the particles on TEM grids.

Prof. Johannes Kiefer generated Figure 26 and provided input on FTIR data analysis.

Declaration

I, hereby, declare that I have completed the work presented in this solely and all references and collaborators have been dutifully cited.

_____

Adithya Käse